ANTARCTIC SUBGLACIAL HYDROLOGY
—
INTERACTIONS OF SUBGLACIAL LAKES, BASAL WATER FLOW AND ICE DYNAMICS

SEBASTIAN GÖLLER

Universität Bremen

Dissertation zur Erlangung des akademischen Grades
Doktor der Naturwissenschaften (Dr. rer. nat.)

18. Februar 2014

ERKLÄRUNG

Hiermit versichere ich, dass ich

1. die Arbeit ohne fremde Hilfe angefertigt habe,

2. keine anderen als die von mir angegebenen Quellen und Hilfsmittel benutzt habe und

3. die den benutzten Werken wörtlich oder inhaltlich entnommenen Stellen als solche kenntlich gemacht habe.

Bremen, 18. Februar 2014

Sebastian Göller

ABSTRACT

The Antarctic Ice Sheet influences the global temperature and sea level by complex interactions with the atmosphere and the ocean and is thus an important factor in the Earth's climate system. Recent climate assessments reveal a steady increase of global temperatures and an on-going shrinking of glaciers and ice sheets. Because the total Antarctic ice volume has the potential to raise the global sea level by about 58 meters, it is of particular interest to understand the ice dynamics regarding the mass export and thus the contribution to sea level rise. Observations of the last decades reveal a widespread hydrological system of subglacial lakes and drainage networks beneath the Antarctic Ice Sheet which is recognized to have a large impact on the ice dynamics. The aim of this thesis is to investigate this subglacial hydrological environment and its interactions with the ice flow dynamics of the overlying ice sheet.

For reaching this aim, the ice flow model Rimbay is enhanced by a subglacial hydrology module which provides the simulation of basal water flow and the identification of positions and extents of subglacial lakes. This model is then applied to the Antarctic Ice Sheet. A subsequent validation by the analysis of ice-penetrating radar profiles in Dronning Maud Land leads to the identification of 31 new potential subglacial lake locations. Based on these findings, the total number of Antarctic subglacial lakes is estimated to be 1 300±300, a factor of three more than what has been discovered so far. Their overall extent is assessed to cover about 0.6% of the Antarctic ice-bed interface. Furthermore, strong correlations are found between modeled pathways of basal water flow and observed locations of ice streams.

In a detailed investigation of the Ross Ice Streams at the Antarctic Siple Coast the local basal driver of fast ice flow is identified as water saturated and unconsolidated sediment. The assessment of the basal flow regime enables the simulation of basal drainage patterns which are clearly associated with current patterns of fast ice flow. The application of satellite-observed ice surface elevation changes to the present-day ice sheet geometry additionally allows prognostic water flow simulations. They reveal a high dynamic of basal water pathways. In particular, a major hydraulic tributary of the Kamb and Whillans Ice Stream is redirected towards the Bindschadler Ice Stream within the next 200 years, possibly resulting in future increase of ice velocities within the Bindschadler Ice Stream.

In order to gain further insights into the complex feedback mechanisms between an ice sheet and its subglacial environment, ice dynamics and subglacial hydrology are modeled in a coupled approach for a synthetic domain. A new hydrological concept is developed and implemented in Rimbay, providing the dynamic generation of subglacial lakes and covering the spatial and tempo-

ral variability of basal drainage systems. The impact of basal hydrology on the ice dynamic is estimated in various experiments, considering distinct feedback mechanisms. It is demonstrated, that a coupling at full complexity leads to a considerably negative mass balance of the investigated synthetic ice sheet. The results reveal the capabilities of the new hydrological concept and emphasize the necessity to incorporate subglacial hydrology in ice sheet models.

ZUSAMMENFASSUNG

Der Antarktische Eisschild beeinflusst durch seine komplexen Wechselwirkungen mit Atmosphäre und Ozean sowohl die globalen Temperaturen als auch den Meeresspiegel und ist damit ein wichtiger Faktor im Klimasystem der Erde. Aktuelle Klimaberichte weisen einen kontinuierlichen Anstieg der globalen Temperaturen und ein fortschreitendes Abschmelzen von Gletschern und Eisschilden nach. Das gesamte Eisvolumen der Antarktis hat das Potential, den globalen Meeresspiegel um ungefähr 58 Meter anzuheben. Es ist deshalb von besonderem Interesse, die Eisdynamik der Antarktis in Bezug auf ihren Massenabfluss und somit ihren Einfluss auf den Meeresspiegel zu verstehen. Beobachtungen der letzten Dekaden offenbaren die Existenz eines ausgedehnten hydrologischen Netzwerkes aus subglazialen Seen und Flüssen unter dem Antarktischen Eisschild, welches große Auswirkungen auf die Eisdynamik hat. Das Ziel dieser Arbeit ist die Untersuchung dieser subglazialen hydrologischen Komponenten und ihrer Wechselwirkungen mit der Dynamik des darüberliegenden Eisschildes.

Dafür wurde das Eismodell RIMBAY um ein subglaziales Hydrologie-Modul erweitert. Dieses ermöglicht die Simulation basaler Wasserflüsse sowie die Identifikation der Positionen und Ausmaße subglazialer Seen. Das erweiterte Modell wurde auf den Antarktischen Eisschild angewandt und die Ergebnisse durch Auswertung von Radarprofilen aus Dronning Maud Land validiert. Somit konnten 31 neue potentielle subglaziale Seen identifiziert werden. Die gesamte Anzahl subglazialer Antarktischer Seen wurde auf 1 300±300 und ihre gesamte Oberfläche auf ungefähr 0.6% des Antarktischen Eisschildes abgeschätzt. Davon sind gegenwärtig 379 subglaziale Antarktische Seen bekannt. Weiterhin wurden starke räumliche Korrelationen zwischen modellierten basalen Wasserflüssen und beobachteten Eisströmen festgestellt.

Die Region der Antarktischen Siple Coast wurde näher untersucht. Die hohen Eisgeschwindigkeiten der dortigen Ross Eisströme wurden in einer ausführlichen Recherche auf das Vorkommen einer leicht deformierbaren wassergesättigten basalen Schicht aus unkonsolidierten Sedimenten zurückgeführt. Das somit definierte Regime des basalen Wasserflusses ermöglicht die Simulation von basalen Dränagestrukturen, welche eine sehr gute Übereinstimmung mit beobachteten Mustern erhöhter Eisgeschwindigkeiten zeigen. Darüberhinaus wurden prognostische Simulationen des basalen Wasserflusses vorgenommen, indem durch Satelliten gemessene Änderungsraten der Eisoberfläche mit der heutigen Eisgeometrie verrechnet wurden. Diese Methode zeigt eine hohe lokale Variabilität der basalen Dränagestrukturen. Insbesondere ein größerer basaler Wasserzufluss, welcher derzeit unter den Kamb und Whillans Eisströmen mündet, wird innerhalb der nächsten 200 Jahre unter den Bindschadler

Eisstrom umgeleitet, was zu einem zukünftigen Anstieg der Eisgeschwindigkeiten innerhalb des Bindschadler Eisstromes führen kann.

Um einen tieferen Einblick in die komplexen Wechselwirkungsmechanismen zwischen einem Eisschild und seiner sublazialen hydrologischen Umgebung zu erlangen, wurde die Modellierung von Eisdynamik und subglazialer Hydrologie gekoppelt und auf ein idealisiertes Modellgebiet angewandt. Dafür wurde ein neues hydrologisches Konzept entwickelt und in RIMBAY implementiert. Es umfasst zusätzlich die dynamische Entstehung von subglazialen Seen und ist damit in der Lage, die räumliche und zeitliche Variabilität des basalen Dränagesystems realistisch abzubilden. In mehreren Experimenten mit verschiedenen Kopplungsgraden wird der entscheidende Einfluss der subglazialen Hydrologie auf die Eisdynamik demonstriert. Bei voller Komplexität der Kopplung wird eine deutlich negative Massenbilanz des idealisierten Eisschildes nachgewiesen. Diese Ergebnisse zeigen das Potential des neuen hydrologischen Konzepts und unterstreichen die Notwendigkeit, subglaziale Hydrologie in Eismodellen zu berücksichtigen.

ACKNOWLEDGMENTS

CONTENTS

ACRONYMS

AGAP Antarctica's Gamburtsev Province Project

AIS   Antarctic Ice Sheet

AWI   Alfred Wegener Institute

BAS   British Antarctic Surway

DML   Dronning Maud Land

EAIS East Antarctic Ice Sheet

ESA   European Space Agency

FD   Finite Differences

FE   Finite Elements

FS   Full Stokes

GLAS Geoscience Laser Altimeter System

HOM   Higher Order Model

InSAR Interferometric Synthetic Aperture Radar

IPCC Intergovernmental Panel on Climate Change

NASA National Aeronautics and Space Administration

NSIDC National Snow and Ice Data Center

RAMP RADARSAT-1 Antarctic Mapping Project

RES   radio-echo sounding

RIMBAY *Revised Ice Model Based on Frank Pattyn*

SAR   Synthetic Aperture Radar

SCAR Scientific Committee on Antarctic Research

SIA   Shallow Ice Approximation

SIRAL Synthetic Aperture Radar Interferometric Radar Altimeter

SSA   Shallow Shelf / Shelfy Stream Approximation

WAIS West Antarctic Ice Sheet

GENERAL INTRODUCTION

In 1955, the glaciologist and later director of the British Scott Polar Research Institute, Gordon de Quetteville Robin, investigated temperature distributions in ice sheets and stated carefully:

"It is suggested that a rise from temperatures below melting point at the base of ice sheets may provide an explanation of the occasional catastrophic advances of certain glaciers." (*Robin*, *1955*)

Today, a growing number of remote sensing and ground-based observations across Antarctica and Greenland are highlighting the existence of subglacial water in a variety of forms, ranging from large subglacial lakes to water flow in millimeter-thick layers at the ice-substrate interface. Subglacial hydrological processes are recognized to have a great impact on ice dynamics and to contribute through complex feedback mechanisms to changes in ocean circulation, sea level and global climate evolution.

1.1 MOTIVATION

The cryosphere is an important part of the global climate system and comprises those portions of the Earth's surface where water is in its solid form, frozen into ice or snow. Elements of the cryosphere are found at all latitudes and encompass glaciers, ice caps and ice sheets as well as lake and river ice, sea ice, snow cover and frozen ground (Fig. 1).

■ Sea Ice	■ Ice Shelves	▬ Sea Ice 30 Yr Ave Extent
■ Glaciers	■ Continuous Permafrost	▬ 50% Snow Extent Line
■ Ice Sheet	■ Discontinuous Permafrost	▬ Max Snow Extent Line
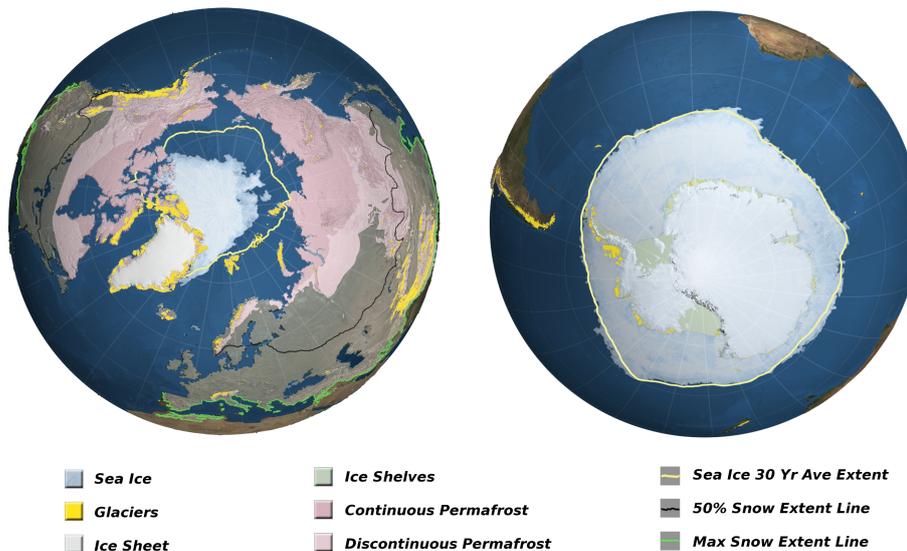
Figure 1: Components of the Earth's cryosphere in the Northern and Southern Hemisphere (Fig. after Goddard Space Flight Center, 2011).

Figure 2: The Antarctic Ice Sheet (white) with its ice shelves (gray) and other geographical features (Fig. after British Antarctic Survey, 2007).

The cryosphere is linked to its environment by many processes. It influences moisture fluxes, precipitation, hydrology, atmospheric and oceanic circulation. In particular, the high albedo of snow-covered areas has a large impact on the radiation balance. A change in extent of these areas directly affects the surface temperature of the Earth. Moreover, the components of the cryosphere store large amounts of water whereas nowadays about 99% of the global ice volume is concentrated in the ice sheets of the polar regions, in Greenland and in Antarctica. They have the potential to alter the global sea level by several meters under the influence of climate changes within the next centuries (Rignot et al., 2011b).

In its Fifth Assessment Report in 2013, the Intergovernmental Panel on Climate Change (IPCC) reveals a steady increase of global temperatures and an ongoing shrinking of glaciers and ice sheets over the last decades (IPCC, 2013). Consequently, the investigation and understanding of the ice dynamics of the large ice sheets is of particular interest since a raising sea level is threatening human habitats and economy.

The focus of this thesis is on the investigation of the Antarctic Ice Sheet (AIS) which is situated on a continental land mass at the South Pole (Fig. 2). It is subdivided into the Antarctic Peninsula and the West and East Antarctic Ice Sheets which are separated by the Transantarctic Mountains. Nearly half of the Antarctic coast line is covered by ice shelves, floating ice extensions of the
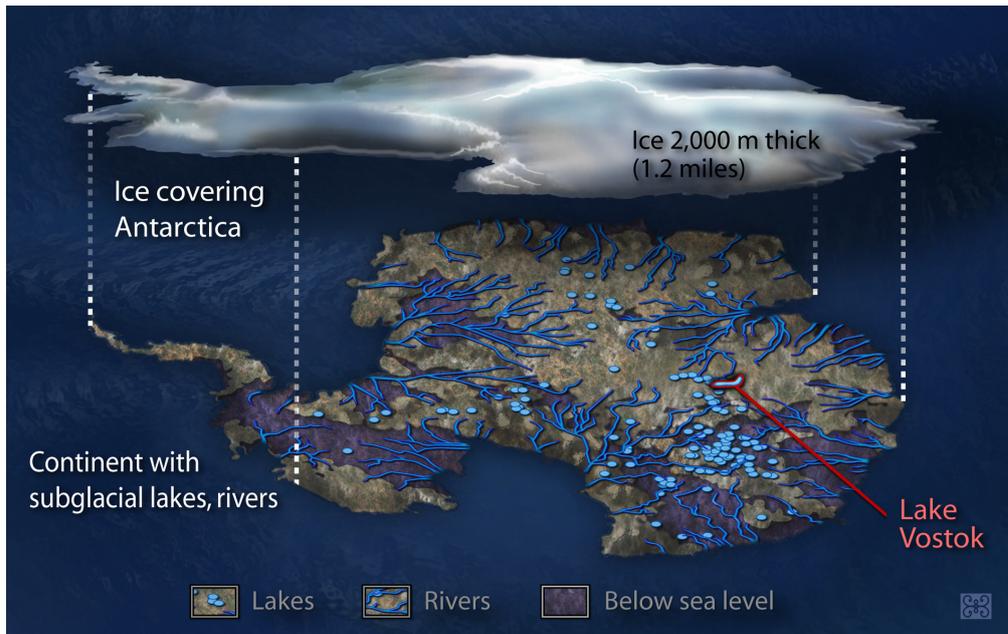
Figure 3: Beneath the AIS 379 subglacial lakes have been discovered so far. They are connected by subglacial rivers and form a widespread hydrological network which influences the dynamics of the overlaying ice. The largest subglacial lake is Lake Vostok. (Fig. by National Science Foundation, 2007b)

AIS. According to Fretwell et al. (2013), the total ice volume of the AIS has an sea level equivalent of about 58 m.

The evolution of the Antarctic ice volume is determined by its mass balance. Any imbalance of the dynamic equilibrium between mass gain and mass loss results in either a growth or a decrease of the ice body. The AIS gains mass by surface snow accumulation. The mass loss is dominated by two processes in approximately equal shares (Depoorter et al., 2013): First, mass is lost by calving of glaciers and ice shelfves where ice breaks off and forms icebergs. Second, the floating ice shelves loose mass at their base by melting due to the ocean heat flux. In comparison, only a vanishing low portion is contributed by ice melting at the base of grounded ice and by surface melting (only at the Antarctic Peninsula).

The mass balance of the AIS can be estimated by measuring ice surface elevation changes with laser or radar satellite altimetry, by detecting mass changes using gravimetry or by balancing the observed accumulation and ice flow over the grounding line (e.g., Shepherd et al., 2012). Current assessments of the Antarctic mass balance reveal a negative tendency, corresponding to a contribution of 0.27±0.11 mm per year to global sea level rise (IPCC, 2013).

The ice flow from the interior of the AIS towards its margins is caused by gravity and is the combined result of creep flow and basal sliding (e.g., Greve and Blatter, 2009). The flow follows the ice sheet surface gradient and reaches surface velocities in the order of meters per year in the inner regions of the ice sheet. At the ice sheet margins, the ice flow is dominated by several fast flowing ice streams. They transport large amounts of ice at velocities of up to
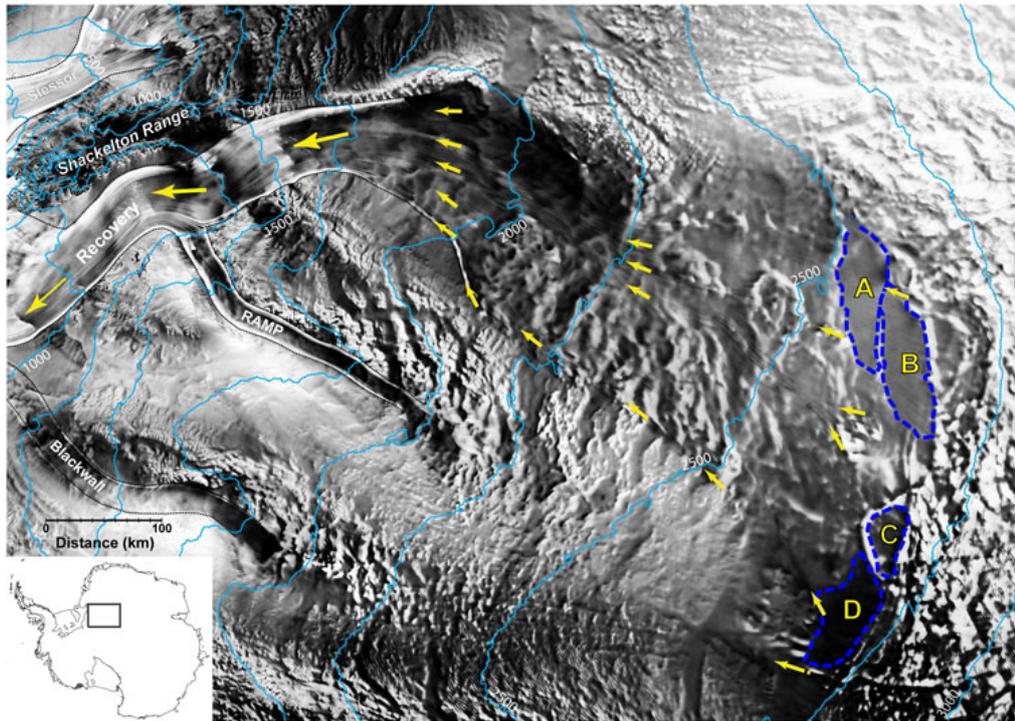
Figure 4: Effects of subglacial hydrology by the example of the Recovery Region, Antarctica: The hydrologically connected Recovery Lakes (A–D) collect basal melt water from upstream areas and release it towards the bedrock trench underneath the Recovery Glacier. There the concentrated flow of water is supposed to lower the basal friction of ice and thus increase ice flow velocities (yellow arrows) (Fig. by Bell et al., 2007).

several hundred meters per year towards the coast or are feeding into adjacent ice shelves (Rignot et al., 2011a). Large ice surface velocities are commonly associated with processes at the ice-bed interface, e.g., sediment deformation or the occurrence of basal water, enhancing the basal sliding.

The existence of water at the ice base is proven by the observation of 379 subglacial lakes within the last five decades (Wright and Siegert, 2012, Fig. 3). They have been identified using airborne radio-echo sounding (RES), satellite altimetry and ground-based seismic investigations. Subglacial lakes can occur despite the very low surface temperatures of the AIS because geothermal heat flux, frictional heating generated by ice sliding over the bedrock and internal deformation of the ice sheet act as heat sources. In combination with the insulating effect and the pressure of the up to 4 700 meters thick ice cover, the ice base can locally reach its pressure melting point, first theoretically predicted by Robin (1955). Model studies reveal that about 55% of the base of the AIS might be at its pressure melting point (Pattyn, 2010).

Observations also indicate interactions between different subglacial lakes over distances of several hundred kilometers (e.g., Wingham et al., 2006b; Fricker and Scambos, 2009; Fricker et al., 2010) and thus reveal that these lakes are not isolated, but belong to distinct subglacial hydrological networks (Fig. 3). Basal water lubricates the base of the ice sheet locally and hence leads to a re-

duced basal drag of the overlaying ice. As a result, fast flowing ice streams can evolve above areas of enhanced subglacial water flow and the ice velocity increases over subglacial lakes (e.g., Bell et al., 2007, Fig. 4). Increased ice velocities affect the mass balance of the AIS and thus have a considerable impact on global sea level rise. Consequently, it is necessary to incorporate basal hydrology into ice sheet models as it is considered to be one of the key processes required to achieve more realistic results with respect to climate projections (IPCC, 2013).

1.2 OBJECTIVES AND STRUCTURE OF THE THESIS

The aim of this thesis is to gain a better understanding of the Antarctic subglacial hydrological environment which belongs to the least accessible regions on Earth. Its main components comprise water storage by subglacial lakes and basal water transport between lakes and towards the grounding line. For the transport of water different flow regimes exist, having distinct impacts on the ice sheet's basal sliding conditions. The type of the locally dominating flow regime depends on the prevalent basal water pressure and the geological properties of the ice's substrate. Therefore, determining the distribution and nature of water flow at the bed of the AIS is considered a milestone regarding predictions of the ice dynamics under the influence of a warming climate. In this work a variety of approaches is combined to gain further insights into the character and distribution of subglacial water flows and its interactions with ice dynamics. The applied methods range from the analysis of airborne RES data and satellite altimetry observations to hydrology and ice modeling and thus unite remote-sensing and modeling strategies.

The outline of this thesis is described as follows: Chapter 2 and 3 provide the necessary background knowledge and specific preliminaries for the three main research Chapters 4 to 6. Chapter 7 contains the final conlusion and an outlook. Below, the objectives of each chapter are described in more detail:

Chapter 2 gives a brief introduction to the elements of an ice sheet-shelf system and the principles of ice flow. It contains an overview about different existing ice models and presents the fundamental equations of ice modeling. The essential equations for the calculation of ice velocities, ice temperature and ice sheet-shelf evolution are derived, corresponding to their implementation in the *Revised Ice Model Based on Frank Pattyn* (RIMBAY) (Thoma et al., 2014) which is used in this work.

Chapter 3 describes the components and the current state of research of the Antarctic hydrological environment. The focus is on the history, detection and occurrence of subglacial lakes as well as the distinction of different basal water flow regimes and their impact on ice flow. Principle approaches of modeling

subglacial hydrology and their implementation in RIMBAY are presented.

In Chapter 4 the distribution of the two main elements of subglacial hydrology (subglacial lakes and basal drainage pathways) is investigated for the AIS, raising two main research questions: **To which extent are subglacial lakes covering the base of the Antarctic Ice Sheet?** To answer this question, locations and extents of subglacial lakes are modeled by using the observed ice sheet topography. The results are validated by a comparison with the latest inventory of Antarctic subglacial lakes and the selective interpretation of radar profiles from RES flight campaigns of the Alfred Wegener Institute (AWI). **What are the drainage patterns of melt water flow beneath the Antarctic Ice Sheet on a continental scale?** This question is addressed by modeling Antarctic basal water pathways with RIMBAY. Drainage patterns and particular lake drainage pathways are analyzed as well as correlations between simulated water flow and satellite-observed ice surface velocities.

Chapter 5 focuses on interactions of subglacial hydrology and ice dynamics in the West Antarctic Ice Sheet (WAIS) and addresses the following questions: **What controls the spatial and temporal variability of the Ross Ice Streams at the Siple Coast?** The impact of basal hydrology is estimated by considering local seismic, radar and borehole observations of geological and hydrological properties as well as sliding velocities at the ice base. Additionally, detected ice surface elevation changes by the satellites altimetry campaigns IceSat and CryoSat-2 are consulted. **Can modeled basal drainage patterns explain the current configuration of the Ross Ice Streams? Which potential impact have satellite-observed surface changes on the evolution of drainage pathways and what might be the implications for future ice stream dynamics?** This question is approached by assessing the local flow regime of basal water and modeling basal water pathways and catchment areas for the current and the estimated prognostic ice sheet geometry with RIMBAY.

In Chapter 6 examines the question: **How much do interactions of ice dynamics and subglacial hydrology affect the mass balance of an ice sheet?** For answering this question, a new hydrological concept is developed and coupled to the ice model RIMBAY. In increasing levels of complexity regarding the coupling of hydrology and ice model, the distinct effects of the particular interactions are investigated and compared for a synthetic ice sheet.

Chapter 7 concludes the key findings and provides an outlook for possible future studies.

2

UNDERSTANDING ICE DYNAMICS AND ICE MODELING

This chapter provides a brief introduction to the components of ice-sheet shelf systems and the basics of ice flow for the example of Antarctica. Subsequently, an overview of existing ice flow models is given and the fundamental equations of ice modeling as well as their implementation in the *Revised Ice Model Based on Frank Pattyn* (RIMBAY) is described.

2.1 BASICS OF THE ANTARCTIC ICE SHEET-SHELF SYSTEM

In the following, a short introduction to the elementary processes of ice flow and a definition of the basic components of the Antarctic Ice Sheet-Shelf system (Fig. 5) is given. More comprehensive explanations can be found, e.g., in Cuffey and Paterson (2010).

The Antarctic Ice Sheet (AIS) measures $13.9 \cdot 10^6 \, \text{km}^2$ in area and $26.9 \cdot 10^6 \, \text{km}^3$ by volume (values inclusive ice shelves, Fretwell et al., 2013) and is situated on a continental land mass at the South Pole (Fig. 2). It reaches an ice thickness of more than $4\,700\,\text{m}$ and an elevation of over $4\,000\,\text{m}$ in the continental interior. The ice sheet surface is interrupted by mountain ranges and locally protruding single mountains, called *nunataks*. At the surface of the ice sheet *katabatic winds* carry high density air from the higher and colder elevations down the ice surface slope towards the coast following gravity. The AIS gains mass by surface accumulation, in detail via precipitation of *snow* or *diamond dust*, a type of ground-level cloud composed of tiny ice crystals. The ice crystals at the surface partly evaporate again by sublimation. Snow which is left over
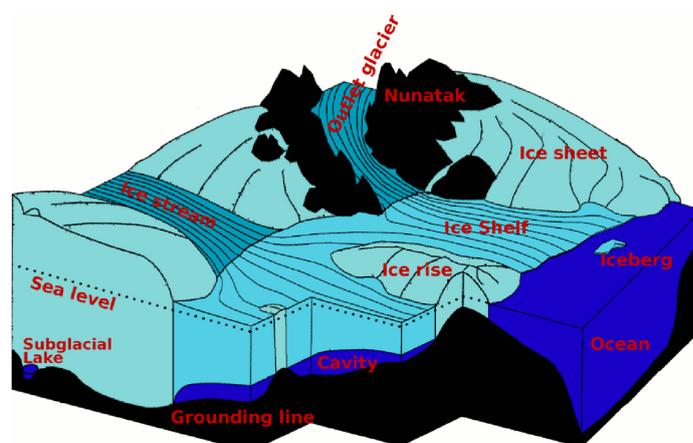
Figure 5: Schematic illustration of several features which belong to an ice sheet/shelf system, e.g., the Antarctica Ice Sheet with its shelves, and have to be considered in modeling approaches (Fig. after Sandhäger, 2000).

from previous seasons is recrystallized into *firn*, which is denser then snow. Over the years, the thickness and weight of the firn layer increases, leading to a further densification until *ice* forms. The ice then flows under the force of gravity and through the combined effect of creep flow and basal sliding from the ice sheet interior to its margins. Depending on the basal thermal regime, the ice can also be frozen to the bedrock. In this case, the flow of ice is solely determined by internal deformation. Smooth ice ridges at the ice sheet surface are separating opposing flow directions, called *ice divides*.

The mass transport of ice in coastal areas of the AIS is dominated by *outlet glaciers* and *ice streams*: channels of fast flowing ice tens of kilometers wide and hundreds of kilometers long that reach velocities of up to $1\,km\,a^{-1}$. Their enhanced sliding velocities are initiated by processes at the ice base, e.g., sediment deformation and lubrication by basal water. Water between the ice base and the underlying substrate originates from *basal melting*, which is caused by the complex influences of geothermal heat flux, internal deformation of the ice, pressure by the overlying ice column and basal friction due to the sliding of ice over the bed. Basal water can accumulate and form *subglacial lakes*, large bodies of water beneath the ice sheet. These subglacial hydrological processes are described in detail in Chap. 3.

Outlet glaciers are constrained in the sides with exposed bedrock while ice streams are bounded by areas of slowly moving ice. At the edges of ice streams shear forces cause ice deformation and recrystallization which make the ice softer and thus concentrate the deformation to narrow bands at the shear margins. As a result of intense local shear stress, deep surface cracks form, called *crevasses*. Outlet glaciers and ice streams feed into the ocean or into *ice shelves*, smooth areas of floating freshwater-ice adjacent to an ice sheet. The *grounding line* divides areas of grounded and floating ice. Floating ice shelves might be locally lifted up by shallow islands or bumps on the seafloor, forming *ice rises*. At the base of ice shelves the ocean heat flux causes basal melting, leading to a thinning of the floating ice. Mass is also lost by *calving* from ice shelves, outlet glaciers and ice streams: ice breaks off at the frontal ice-ocean margins and drifts into warmer waters where it melts eventually. Large pieces of calved and floating ice are also called *icebergs*. In the region of the Antarctic Peninsula also mass loss by surface melting and ablation occurs locally.

2.2 ICE MODELING

Ice models have to face numerous challenges: They must attempt to incorporate the physics of the complex and highly anisotropic material ice in order to describe its internal flow. Additionally, they have to deal with the interactions between ice sheets and ice shelves and their environment at different response time scales. These are processes at the ice surface (temperature, accumulation, ablation), the ice bottom (heat flux, sliding, interaction with basal water) and the ice exterior (calving fronts, geographical constrains, e.g., bedrock to-

pography and nunataks). Some of these external forcings are subject to large uncertainties (e.g., geothermal heat flux) or locally only sparse observational data are available (bedrock elevation). Moreover, the application of ice models ranges from small mountain glaciers (e.g., Alpine glaciers of some kilometers length) to continental ice sheets (Greenland or Antarctic Ice Sheet with extents of several thousand kilometers). And finally, all these tasks should be solved at reasonable computational coast and time scales.

Consequently, several models have been developed during the last decades which are either specialized in a certain subject or aim for a broad scope of applications. Some of these models are open source and thus are steadily improved by a large community of users. Other models base on a commercial package where ice modeling is only one of several possible applications. In general, all ice models can be categorized regarding their discretization which can be Finite Elements (FE) or Finite Differences (FD). FE models are, e.g., Elmer/Ice (e.g., Gagliardini and Zwinger, 2008; Gudmundsson et al., 2012; Gillet-Chaulet et al., 2012), the Ice Sheet System Model (ISSM, e.g., Larour et al., 2012) and Comsol (e.g., Aschwanden and Blatter, 2009; Humbert et al., 2009). Examples for FD models are the Parallel Ice Sheet Model (PISM, Winkelmann et al., 2011; Martin et al., 2011), the Community Ice Sheet Model (CISM, e.g., Bougamont et al., 2011; Lemieux et al., 2011) and the Simulation Code for Polythermal Ice Sheets (SICOPOLIS, Greve, 1997a,b; Sato and Greve, 2012). An overview about recent ice models is given by Bindschadler et al. (2013).

Although all ice models base on the same fundamental equations (see below), they use different implementation strategies to encounter the above challenges which can lead to different modeling results. Since analytical solutions are available for idealized setups (e.g., Huybrechts et al., 1996; Bueler et al., 2007) but not for realistic domains, it is difficult to determine the errors of each particular model. Therefore, the model validities have to be estimated by comparing the model outcomes for a series of benchmark experiments (e.g., Huybrechts et al., 1996; Pattyn et al., 2012, 2013; Bindschadler et al., 2013).

In this work, the ice model RIMBAY (Thoma et al., 2014) is used. It is based on the FD higher-order numerical ice-flow model of Pattyn (2003), which has been tested and applied to many scenarios (e.g., Pattyn, 2002; Pattyn et al., 2004; Pattyn et al., 2008; Pattyn, 2010). RIMBAY itself has been developed since 2009 at the Alfred Wegener Institute (AWI) in Bremerhavenm, where the original model was improved and extended in numerous aspects. The validity of RIMBAY is proven by several applications (e.g., Thoma et al., 2010, 2012, 2014; Determann et al., 2012; Goeller et al., 2013) and latest benchmark tests (Pattyn et al., 2013). In the following, the fundamental equations of ice modeling and the main calculations of ice velocity and temperature related to the applications in this work are presented. A list of the used physical constants is given in Tab. 1 and a schematic sequence plan of a model run is drafted in Fig. 7. For a comprehensive description of the ice model implementations it is referred to Thoma et al. (2014).

2.2.1 *Fundamental equations*

In general the field equations for ice modeling follow a continuum thermo-dynamic mechanics approach based on the conservation of mass, momentum and energy (e.g., Pattyn, 2003)

$$\frac{\partial \rho_i}{\partial t} = -\vec{\nabla} \cdot (\rho_i \vec{v}) \tag{1}$$

$$\rho_i \frac{d\vec{v}}{dt} = \vec{\nabla} \cdot \tau + \rho_i \vec{g} \tag{2}$$

$$\rho_i c_p \frac{d\theta}{dt} = \vec{\nabla} \left(\kappa \vec{\nabla} \theta \right) + Q \tag{3}$$

with

ρ_i ice density

$\vec{v}$ ice velocity with $\vec{v} = (v_x, v_y, v_z) = (u, v, w)$

$\vec{g}$ gravitational acceleration with $\vec{g} = (0, 0, g)$

τ stress tensor

θ potential ice temperature

c_p heat capacity of ice

κ thermal conductivity of ice

Q internal frictional heating due to deformation.

Treating the ice as an incompressible fluid with a constant density the conservation of mass equation (Eq. 1) simplifies to

$$\vec{\nabla} \cdot \vec{v} = \frac{\partial u}{\partial x} + \frac{\partial v}{\partial y} + \frac{\partial w}{\partial z} = 0. \tag{4}$$

The hydrostatic pressure p is defined by the trace of the stress tensor τ with

$$p = -\frac{1}{3} \operatorname{tr} (\tau) \tag{5}$$

$$= -\frac{1}{3} \left(\tau_{xx} + \tau_{yy} + \tau_{zz} \right). \tag{6}$$

Since the hydrostatic pressure is isotropic, only the deviations from p on the trace of the stress tensor τ affect the ice deformation. Consequently, it is proceeded with the deviatoric stress tensor τ' defined as

$$\tau'_{ij} = \tau_{ij} + p\, \delta_{ij} \tag{7}$$

$$= \tau_{ij} - \frac{1}{3} \left(\tau_{xx} + \tau_{yy} + \tau_{zz} \right) \delta_{ij} \tag{8}$$

where δ_{ij} is the Kronecker-delta. Neglecting the acceleration term in Eq. 2, the linear momentum can be written as

$$\begin{aligned} \frac{\partial \tau'_{xx}}{\partial x} + \frac{\partial \tau'_{xy}}{\partial y} + \frac{\partial \tau'_{xz}}{\partial z} - \frac{\partial p}{\partial x} &= 0 \\ \frac{\partial \tau'_{yx}}{\partial x} + \frac{\partial \tau'_{yy}}{\partial y} + \frac{\partial \tau'_{yz}}{\partial z} - \frac{\partial p}{\partial y} &= 0 \\ \frac{\partial \tau'_{zx}}{\partial x} + \frac{\partial \tau'_{zy}}{\partial y} + \frac{\partial \tau'_{zz}}{\partial z} - \frac{\partial p}{\partial z} &= \rho_i g. \end{aligned} \tag{9}$$

Symbol	Name	Value	Unit
α	pressure melting factor	$8.7 \cdot 10^{-4}$	$\mathrm{K\,m^{-1}}$
γ_T	thermal exchange velocity	10^{-4}	$\mathrm{m\,s^{-1}}$
ρ_i	density of ice	910	$\mathrm{kg\,m^{-3}}$
ρ_o	density of ocean water	1 028	$\mathrm{kg\,m^{-3}}$
ρ_w	density of melt water	1 000	$\mathrm{kg\,m^{-3}}$
κ	thermal conductivity of ice	2.1	$\mathrm{W\,m^{-1}\,K^{-1}}$
C	sliding rate	10^7	$\mathrm{Pa\,m^{-1/3}\,s^{1/3}}$
c_p	heat capacity of ice	2 009	$\mathrm{J\,kg^{-1}\,K^{-1}}$
c_{po}	heat capacity of ocean water	3 974	$\mathrm{J\,kg^{-1}\,K^{-1}}$
g	gravitational constant	9.81	$\mathrm{m\,s^{-2}}$
L_i	specific latent heat of fusion for ice	335	$\mathrm{kJ\,kg^{-1}}$
m	sliding coefficient	$1/3$	
n	flow exponent	3	
s_o	salinity of ocean water	35	$\mathrm{g\,kg^{-1}}$
T_o	ocean temperature	271.45	K

Table 1: Constants used in ice model RIMBAY.

The stresses τ'_{ij} can be linked to the strain rates $\dot{\epsilon}_{ij}$ using Glens flow law for polycrystalline ice (Cuffey and Paterson, 2010)

$$\dot{\epsilon}_{ij} = A\left(\theta^*\right) {\tau'_{ij}}^n \tag{10}$$

where θ^* is the ice temperature corrected for pressure-melting (Greve and Blatter, 2009), $A\left(\theta^*\right)$ is a temperature-dependent rate factor parametrized according to the Arrhenius relationship after Hooke (1981) and n the flow exponent. Equation 10 can be also reformulated to

$$\tau'_{ij} = 2\eta\dot{\epsilon}_{ij} \tag{11}$$

with the effective ice viscosity η defined as

$$\eta = \frac{1}{2}A(\theta^*)^{-\frac{1}{n}}\,\dot{\epsilon}^{\frac{1-n}{n}}. \tag{12}$$

The effective strain rate $\dot{\epsilon}$ is the second invariant of the strain rate tensor can be written as

$$\dot{\epsilon} = \sum_{ij}\frac{1}{2}\dot{\epsilon}_{ij}\dot{\epsilon}_{ij}. \tag{13}$$

Using the principle of mass conservation (Eq. 4), it can be formulated as

$$\dot{\epsilon} = \sqrt{\dot{\epsilon}_{xx}^2 + \dot{\epsilon}_{yy}^2 + \dot{\epsilon}_{xx}\dot{\epsilon}_{yy} + \dot{\epsilon}_{xy}^2 + \dot{\epsilon}_{xz}^2 + \dot{\epsilon}_{yz}^2}. \tag{14}$$

Following the relation between strain rates $\dot{\epsilon}_{ij}$ and velocity gradients with

$$\dot{\epsilon}_{ij} = \frac{1}{2}\left(\frac{\partial v_i}{\partial j} + \frac{\partial v_j}{\partial i}\right), \tag{15}$$

Eq. 11 can be rewritten as

$$\tau'_{ij} = 2\eta \begin{pmatrix} \frac{\partial u}{\partial x} & \frac{1}{2}\left(\frac{\partial u}{\partial y} + \frac{\partial v}{\partial x}\right) & \frac{1}{2}\left(\frac{\partial u}{\partial z} + \frac{\partial w}{\partial x}\right) \\ \frac{1}{2}\left(\frac{\partial u}{\partial y} + \frac{\partial v}{\partial x}\right) & \frac{\partial v}{\partial y} & \frac{1}{2}\left(\frac{\partial v}{\partial z} + \frac{\partial w}{\partial y}\right) \\ \frac{1}{2}\left(\frac{\partial u}{\partial z} + \frac{\partial w}{\partial x}\right) & \frac{1}{2}\left(\frac{\partial v}{\partial z} + \frac{\partial w}{\partial y}\right) & \frac{\partial w}{\partial z}. \end{pmatrix} \tag{16}$$

Finally, the so-called Full Stokes (FS) equations for ice modeling are obtained after combining Eq. 9 and 16:

$$\frac{\partial}{\partial x}\left(2\eta\frac{\partial u}{\partial x}\right) + \frac{\partial}{\partial y}\left(\eta\frac{\partial u}{\partial y} + \eta\frac{\partial v}{\partial x}\right) + \frac{\partial}{\partial z}\left(\eta\frac{\partial u}{\partial z} + \eta\frac{\partial w}{\partial x}\right) - \frac{\partial p}{\partial x} = 0$$

$$\frac{\partial}{\partial x}\left(\eta\frac{\partial u}{\partial y} + \eta\frac{\partial v}{\partial x}\right) + \frac{\partial}{\partial y}\left(2\eta\frac{\partial v}{\partial y}\right) + \frac{\partial}{\partial z}\left(\eta\frac{\partial v}{\partial z} + \eta\frac{\partial w}{\partial y}\right) - \frac{\partial p}{\partial y} = 0 \tag{17}$$

$$\frac{\partial}{\partial x}\left(\eta\frac{\partial u}{\partial z} + \eta\frac{\partial w}{\partial x}\right) + \frac{\partial}{\partial y}\left(\eta\frac{\partial v}{\partial z} + \eta\frac{\partial w}{\partial y}\right) + \frac{\partial}{\partial z}\left(2\eta\frac{\partial w}{\partial z}\right) - \frac{\partial p}{\partial z} = \rho_i g.$$

In order to find an expression for the pressure p in Eq. 17, Eq. 7 is rearranged. With the use of Eq. 11 the pressure is then yielded as a function of the horizontal velocities and the vertical normal stress.

$$p = -\tau'_{xx} - \tau'_{yy} - \tau_{zz}$$

$$= -2\eta\left(\frac{\partial u}{\partial x} + \frac{\partial v}{\partial y}\right) - \tau_{zz} \tag{18}$$

The stress τ_{zz} is obtained by a vertical integration of the last term in Eq. 9 from the surface S to the height z (e.g., Van der Veen and Whillans, 1989; Pattyn et al., 2008):

$$\tau_{zz} = -\rho_i g\,(S - z) + \frac{\partial}{\partial x}\int_z^S \tau'_{xz}\,dz' + \frac{\partial}{\partial y}\int_z^S \tau'_{yz}\,dz'. \tag{19}$$

The first term on the right-hand side in Eq. 19 describes the hydrostatic stress contribution while the second and the third term describe the vertical resistive longitudinal stress. In the hydrostatic approximation only the first hydrostatic term is considered and pressure p can be written as

$$p = -2\eta\left(\frac{\partial u}{\partial x} + \frac{\partial v}{\partial y}\right) + \rho_i g\,(S - z). \tag{20}$$

All equations are converted into terrain-following σ-coordinates (Fig. 6) by

$$\sigma = \frac{S - z}{H} \tag{21}$$

where H is the ice thickness. In this manner the vertical coordinate always ranges from $\sigma = 0$ at the surface to $\sigma = 1$ at the ice base and is thus independent of the local ice thickness and the bedrock elevation. The related coordinate transformation is omitted here, referring back to Pattyn (2003) or Greve and Blatter (2009).
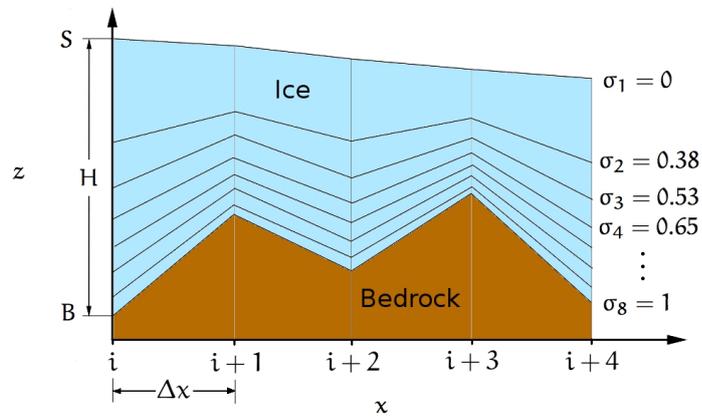
Figure 6: Schematic cross-section of an ice sheet as an example: terrain-following σ-coordinates which become closer from the ice surface elevation S towards the bedrock elevation B. The ice thickness is given by $H = S - B$.
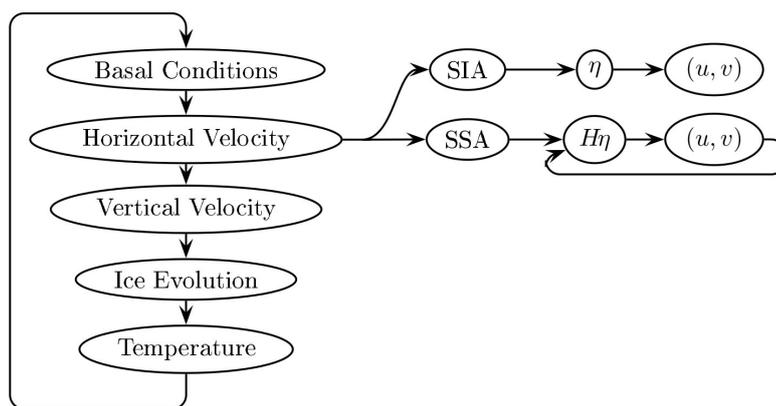
Figure 7: Sequence of iteratively solved variables for SIA and SSA (here the product $H\eta$ is calculated, instead of η) within RIMBAY (Fig. after Thoma et al., 2014).

2.2.2   *Velocity calculation*

2.2.2.1   *Horizontal velocity*

Solving the FS equations for a larger model domain needs a considerable computational effort. Therefore, common approximations of these equations have been established. They allow the modeling of entire ice sheets including their ice shelves in reasonable time spans with an acceptable accuracy (e.g., Hindmarsh, 2004). Only thereby, comprehensive parameter studies like investigations about the impact of various forcing scenarios on current day ice sheets become possible. In the following, two approximations are briefly introduced: the Shallow Shelf / Shelfy Stream Approximation (SSA) (Morland, 1987; MacAyeal, 1989) and the SIA (Hutter, 1983; Morland, 1984). For the sake of completeness, also the Higher Order Model (HOM) approximations by Pattyn (2003) and Blatter (1995) are mentioned, which are not discussed in detail.

SHALLOW SHELF APPROXIMATION   Floating ice shelves move on a stress-free base (the ocean) and thus show barely internal deformation. Hence, the assumption can be made that the horizontal velocity is depth-independent.

$$\frac{\partial u}{\partial z} = \frac{\partial v}{\partial z} = 0 \tag{22}$$

Consequently, several terms can be neglected in Eq. 17, which then simplifies to

$$\frac{\partial}{\partial x}\left(2\eta\frac{\partial u}{\partial x}\right) + \frac{\partial}{\partial y}\left(\eta\frac{\partial u}{\partial y} + \eta\frac{\partial v}{\partial x}\right) - \frac{\partial p}{\partial x} = 0$$
$$\frac{\partial}{\partial x}\left(\eta\frac{\partial u}{\partial y} + \eta\frac{\partial v}{\partial x}\right) + \frac{\partial}{\partial y}\left(2\eta\frac{\partial v}{\partial y}\right) - \frac{\partial p}{\partial y} = 0 \tag{23}$$
$$\frac{\partial}{\partial z}\left(2\eta\frac{\partial w}{\partial z}\right) - \frac{\partial p}{\partial z} = \rho_i g.$$

Applying the hydrostatic approximation (Eq. 20) the vertical momentum balance equation vanishes and an integration of Eq. 23 from the ice base B to the surface S leads to (e.g., MacAyeal, 1989; Greve and Blatter, 2009; Pattyn, 2010)

$$\frac{\partial}{\partial x}\left[2H\eta\left(2\frac{\partial U}{\partial x} + \frac{\partial V}{\partial y}\right)\right] + \frac{\partial}{\partial y}\left[H\eta\left(\frac{\partial U}{\partial y} + \frac{\partial V}{\partial x}\right)\right] - \tau_{bx} = \rho_i g H\frac{\partial S}{\partial x}$$
$$\frac{\partial}{\partial y}\left[2H\eta\left(2\frac{\partial V}{\partial y} + \frac{\partial U}{\partial x}\right)\right] + \frac{\partial}{\partial x}\left[H\eta\left(\frac{\partial U}{\partial y} + \frac{\partial V}{\partial x}\right)\right] - \tau_{by} = \rho_i g H\frac{\partial S}{\partial y} \tag{24}$$

where $H = S - B$ is the ice thickness, $\vec{V} = (U, V)$ is the vertically averaged horizontal ice velocity and $\vec{\tau}_b = (\tau_{bx}, \tau_{by})$ is the basal shear stress. The latter can be formulated in terms of the basal friction parameter β^2 and the horizontal ice velocity:

$$\vec{\tau}_b = \beta^2\vec{V}. \tag{25}$$

For floating ice (e.g., ice shelves or ice above subglacial lakes) the basal friction parameter β^2 is zero and, consequently, the basal shear $\vec{\tau}_b$ in Eq. 24 vanishes. The lacking vertical shear stresses reduce the effective strain rate $\dot{\epsilon}$ (Eq. 14) to

$$\dot{\epsilon} = \sqrt{\dot{\epsilon}_{xx}^2 + \dot{\epsilon}_{yy}^2 + \dot{\epsilon}_{xx}\dot{\epsilon}_{yy} + \dot{\epsilon}_{xy}^2}. \tag{26}$$

SHELFY STREAM APPROXIMATION   Fast flowing ice streams show a similar behavior to floating ice since they slide with small internal deformation over slippery or deformable bed structures. Thus, the above approximations made for the Shallow Shelf Approximation are valid for them too and Eq. 24 and 25 can be used with a basal friction parameter $\beta^2 > 0$, calculated below.

SHALLOW ICE APPROXIMATION   For large ice sheets (e.g., Antarctica) the horizontal extension ($\approx 4\,000$ km) is orders of magnitudes larger than the vertical extension (ice thicknesses up to $\approx 4\,000$ m). Under the assumption that the horizontal variations of the vertical ice velocities are much smaller than the vertical variations of the horizontal ice velocities, the normal stress deviators τ'_{xx}, τ'_{yy} and τ'_{zz} as well as the shear stress in the vertical planes τ_{xy} are negligible. Subsequently, all normal stresses are equal to the negative pressure accordingly Eq. 7 and the momentum balance (Eq. 17) reads

$$\frac{\partial}{\partial z}\left(\eta\frac{\partial u}{\partial z}\right) - \frac{\partial p}{\partial x} = 0$$
$$\frac{\partial}{\partial z}\left(\eta\frac{\partial v}{\partial z}\right) - \frac{\partial p}{\partial y} = 0 \tag{27}$$
$$-\frac{\partial p}{\partial z} = \rho_i g.$$

The integration of the vertical momentum balance leads to a further simplification of the hydrostatic approximation (Eq. 20) and defines the pressure p as

$$p = \rho_i g\,(S - z)\,. \tag{28}$$

Thus, the horizontal velocities become decoupled and a local solution of the horizontal velocity field $\vec{u} = (u, v)$ can be obtained by

$$\vec{u}(z) = -2\,(\rho_i g)^n\,|\vec{\nabla}S|^{n-1}\vec{\nabla}S\int_B^z A\,(\theta^*)\,(S - z)^n\,dz' + \vec{u}_b \tag{29}$$

where $\vec{u}_b = \vec{u}(B)$ is the basal sliding velocity at the ice-bedrock interface at elevation B calculated below.

2.2.2.2 Basal sliding

The calculation of the ice velocity requires a boundary condition at the ice base. For the Shallow Ice Approximation (SIA) this is the basal ice velocity $\vec{u}_b$ (Eq. 29). Assumed that the ice is frozen to solid bedrock, it can be simply set to zero, leading to a no-slip condition. In case the ice temperature reaches

the pressure melting point at its base it might start sliding even over solid bedrock. In order to obtain the sliding velocity, a Weertman-type sliding law (e.g., Pattyn et al., 2013) is applied which links the basal velocity to the basal shear stress:

$$\vec{u}_b = \frac{1}{\beta^2}\vec{\tau}_b = C^{-\frac{1}{m}} \left|\vec{\tau}_b\right|^{\frac{1}{m}-1} \vec{\tau}_b \qquad (30)$$

with C is the sliding rate and m is the sliding coefficient. Following Van der Veen and Whillans (1989) the basal shear stress $\vec{\tau}_b = (\tau_{bx}, \tau_{by})$ is given by

$$
\begin{aligned}
\tau_{bx} &= \tau'_{xz} - \left(2\tau'_{xx} + \tau'_{yy}\right)\frac{\partial B}{\partial x} - \tau'_{xy}\frac{\partial B}{\partial y} \\
\tau_{by} &= \tau'_{yz} - \left(2\tau'_{yy} + \tau'_{xx}\right)\frac{\partial B}{\partial y} - \tau'_{xy}\frac{\partial B}{\partial x}.
\end{aligned}
\qquad (31)
$$

For the SIA these equations simplify to

$$\vec{\tau}_b = -\rho_i g H \vec{\nabla} S \qquad (32)$$

and in combination with Eq. 30 the basal velocity is obtained, required for the upward integration of all horizontal ice velocities (Eq. 29).

For calculating the velocity field in the SSA (Eq. 24) the basal shear stress $\vec{\tau}_b = \beta^2 \vec{V}$ is needed as a boundary condition. In case of the Shallow Shelf Approximation no basal friction is present and the basal friction parameter can be set to $\beta^2 = 0$. In the Shelfy Stream Approximation the non-vanishing basal friction can be obtained from Eq. 30:

$$\beta^2 = C^{\frac{1}{m}} \left|\vec{\tau}_b\right|^{1-\frac{1}{m}}. \qquad (33)$$

In order to reduce the nonlinearity of the SSA momentum balance, the basal shear stress $\vec{\tau}_b$ in Eq. 33 can be expressed by the approximation given in Eq. 32 (e.g., Cuffey and Paterson, 2010). Typical values for β^2 are the range of $\beta^2 = 0$ for a stress-free ice base (e.g., above subglacial lakes and for ice shelves) and $\beta^2 \approx 25\,000\,\text{Pa}\,\text{m}^{-1}\,\text{a}$ (typical ice velocity of $v = 4\,\text{m}\,\text{a}^{-1}$ at a basal shear stress of $\tau_b = 100\,\text{kPa}$, Cuffey and Paterson, 2010).

2.2.2.3 *Vertical velocity*

The vertical velocity w at elevation z is obtained by integrating the incompressibility condition (Eq. 4) from the ice base upwards:

$$w(z) = w_b - \int_B^z \left(\frac{\partial u}{\partial x} + \frac{\partial v}{\partial y}\right) \mathrm{d}z'. \qquad (34)$$

At the ice base the vertical velocity w_b is given by

$$w_b = \frac{\partial B}{\partial t} + u_b \frac{\partial B}{\partial x} + v_b \frac{\partial B}{\partial y} - M_b \qquad (35)$$

where M_b is the basal melt rate, calculated below.

2.2.3   *Temperature calculation*

2.2.3.1   *Ice temperature*

The energy conservation equation (Eq. 3) can be split into an advective, a diffusive and a source term:

$$\rho_i c_p \left(\frac{\partial \theta}{\partial t} + \underbrace{\vec{v}\vec{\nabla}\theta}_{\text{Advection}} \right) = \underbrace{\kappa \vec{\nabla}^2 \theta}_{\text{Diffusion}} + \underbrace{Q}_{\text{Internal Sources}} \tag{36}$$

where the heat capacity c_p and the thermal conductivity κ are assumed to be constant. For the calculation of the temperature evolution it is presumed that internal deformation Q is the only internal heat source (Cuffey and Paterson, 2010) with

$$Q = 2\dot{\epsilon}\tau' = 4\eta\dot{\epsilon}^2 \tag{37}$$

where τ' is the effective deviatoric stress. The neglection of horizontal diffusion leads to

$$\frac{\partial \theta}{\partial t} = \frac{\kappa}{\rho_i c_p} \frac{\partial^2 \theta}{\partial z^2} - u\frac{\partial \theta}{\partial x} - v\frac{\partial \theta}{\partial y} - w\frac{\partial \theta}{\partial z} + 4\eta\dot{\epsilon}^2. \tag{38}$$

At the ice surface Eq. 38 is forced by the mean surface air temperature θ_s. At the ice base, it has to distinguished between floating and grounded ice. For floating ice a Dirichlet boundary condition according to the temperature of the pressure melting point is applied (e.g., Cuffey and Paterson, 2010):

$$\theta_b = -\alpha H \tag{39}$$

with the pressure melting factor α. For grounded ice the Neumann boundary condition is used:

$$\frac{\partial \theta_b}{\partial z} = -\frac{G + \vec{\tau}_b \vec{u}_b}{\kappa} \tag{40}$$

where the basal heat-flow into the ice is given by the geothermal heat flux G and frictional heating contribution $\vec{\tau}_b \vec{u}_b$ resulting from the ice sliding over the bedrock.

2.2.3.2   *Basal melting*

The basal melt rate M_b for grounded ice is computed by balancing the heat fluxes at the ice base. These are the flux of heat into the ice base dependent on the ice temperature gradient, the geothermal heat flux at the bedrock surface and the frictional heating at the ice-bedrock interface (e.g., Pattyn, 2003):

$$M_b = \frac{1}{L_i}\rho_i \left(\kappa \frac{\partial \theta_b^*}{\partial z} + G + \vec{\tau}_b \vec{v}_b \right) \tag{41}$$

where L_i is the specific latent heat of fusion for ice and θ_b^* is the basal ice temperature corrected for pressure melting. The last term in Eq. 41) is the contribution of basal frictional heating which can dominate the melting at the ice

base in areas of faster ice flow (e.g., Joughin et al., 2004; Cuffey and Paterson, 2010) but can be ignored in areas where the ice is frozen to the bedrock.

For floating ice the basal melt rate M_b can be either obtained by an external forcing, e.g., an ocean model (e.g., Grosfeld et al., 1997; Determann et al., 2012) or it can be calculated using the parametrization of Beckmann and Goosse (2003):

$$M_b = \frac{1}{L\rho_i}\rho_o c_{po}\gamma_T \left(T_o - T_f\right) A_{\text{eff}} \tag{42}$$

where ρ_o is the density of ocean water, c_{po} is the the specific heat of ocean water, γ_T is the thermal exchange velocity and T_o is the ocean temperature. The area A_{eff} is the effective area for melting and can be regarded as a tuning factor depending on the particular geometry of an ice shelf and especially its cavities. The freezing point temperature T_f at the elevation of the ice shelf base H_b is parametrized by

$$T_f = 273.15\,\text{K} + 0.0939\,\text{K} - s_o \cdot 0.057\,\text{K} + H_b \cdot 7.64 \cdot 10^{-4}\,\text{K}\,\text{m}^{-1} \tag{43}$$

with the ocean water salinity s_o.

2.2.4 *Ice sheet evolution*

The conservation of mass is given by Eq. 1 which is integrated from the ice base B to the ice surface S under the assumption of a constant ice density ρ_i. Thus, an equation for the spatial evolution of the ice thickness $H = S - B$ is gained

$$\frac{\partial H}{\partial t} = -\left(\frac{\partial\,UH}{\partial x} + \frac{\partial\,VH}{\partial y}\right) + M \tag{44}$$

where U and V are the vertically averaged horizontal velocities. The mass balance M in Eq. 44 is defined as

$$M = M_s - M_b \tag{45}$$

where M_s comprises local surface accumulation and surface melt-water ablation and M_b basal melting and refreezing.

3

INTRODUCTION TO ANTARCTIC SUBGLACIAL HYDROLOGY

Investigations over the last five decades reveal the existence of a wide-spread hydraulic system beneath the Antarctic Ice Sheet. It comprises hundreds of lakes at the ice-bed interface which are integrated in distinct subglacial hydrological networks. In this chapter, the main objects of research regarding Antarctic subglacial hydrology are considered: subglacial lakes and subglacial water flow. The origin and interactions of subglacial lakes with the overlying ice sheet are described as well as the methods and history of their exploration. Different regimes of subglacial water flow and their impact on the basal sliding of the ice sheet are discussed and illustrated. Furthermore, fundamental methods of modeling subglacial hydrology are introduced: the calculation of the basal hydraulic potential and the computation of basal water fluxes and pathways using the balance flux approach.

3.1 SUBGLACIAL LAKES

3.1.1 *Origin and motivation*

Antarctic subglacial lakes are discrete bodies of water that form at the base of the East and West Antarctic Ice Sheets between ice and bedrock (Fig. 8). Despite the very low surface temperatures of the Antarctic Ice Sheet they can exist because large areas of the ice sheet base are at the pressure melting point,
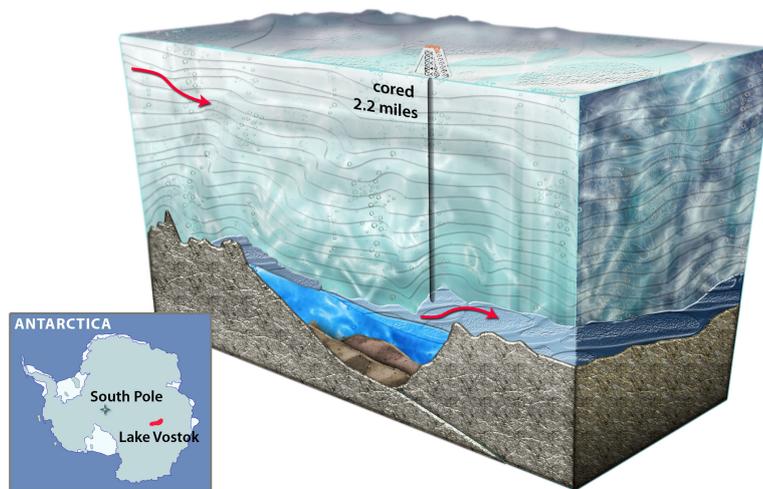
Figure 8: Schematic cross section of Lake Vostok beneath the East Antarctic Ice Sheet, the largest known subglacial lake (Fig. by National Science Foundation, 2007a).

actively melting through the combined influence of the insulating ice cover, strain heating and the geothermal heat flux into the base of the ice sheet. Melt water then flows under the forces of gravity and overburden ice pressure and accumulates within subglacial topographic hollows forming subglacial lakes (e.g., Kapitsa et al., 1996; Wright and Siegert, 2012). Following Duxbury et al. (2001) todays subglacial lakes might have already existed before the complete glaciation of Antarctica and survived the subsequent build-up of the Antarctic Ice Sheet. Pattyn (2004) confirmed this theory with ice model simulations while Siegert (2004) challenged this view and stated that during the ice sheet growth the ice would have grounded throughout the entire lake bed.

Subglacial lakes in Antarctica are studied for three scientific reasons: First, subglacial lakes comprise unique and one of the most extreme habitats on Earth. They are isolated from the circulation of the atmosphere and subject to permanent darkness, low temperatures of -2 to -4°C and enormous pressure of 22-40 bar (e.g., Carter et al., 2007). It has not been possible to take and analyse direct water samples yet. However, microbes were found in samples of accreted ice (water of the lake refrozen to its ice roof) proofing the existence of life despite the extreme conditions (Abyzov et al., 2001). Within the perspective of planetary science this indicates that life might exist under the surface of the Martian ice cap or the icy moons of Saturn and Jupiter (Wynn-Williams and Edwards, 2000; Duxbury et al., 2001; Siegert et al., 2001). Techniques developed for the exploration of Antarctic subglacial lakes (Siegert et al., 2007) have therefore applications to the search of extra-terrestrial life as well.

Second, sediments existing at the base of subglacial lakes may contain high-resolution records of ice sheet history (e.g., Siegert, 2000). Following Zotikov (1987) the steady flow of *dirty ice* across a subglacial lake combined with low melting rates at the ice-lake interface of about $1 \, \mathrm{mm \, a^{-1}}$ could result in a very low sedimentation rate. Since subglacial lakes may be millions of years old, sediment layers in the order of tens or hundreds of meters could have accumulated at the lake bottom. These sedimentary records would date back to the time at which the lake was formed and could provide climate informations and biodata older than 5-30 million years. Current ice cores only refer back in ice sheet history for 740 000 years (Augustin et al., 2004) whereby a possible maximum age of about 1.5 million years has been estimated for Antarctic ice cores (Fischer et al., 2013). However, no sediment cores within Antarctic subglacial lakes have been drilled so far.

The third reason is the most relevant one for this study: subglacial lakes are an important component of the widespread hydraulic system beneath the Antarctic Ice Sheet. They are known to interact with the overlying ice and considerably affect the ice dynamics. The basal friction of the moving ice sheet vanishes over subglacial lake surfaces. This leads to a distinct local increase of the ice velocities (e.g., Kwok et al., 2000; Pattyn et al., 2004) and also has an impact on the adjacent and faraway ice flow (Thoma et al., 2012). The modeling of water circulation inside a subglacial lake reveals local melting and

refreezing rates at the ice-water-interface in the order of 1-10 mm a^{-1} (Thoma et al., 2008, 2009, 2010, 2012). These thermodynamical processes at the lake-ice boundary alter the ice temperature up to 10 % and thereby modify the highly non-linear ice viscosity (Thoma et al., 2012) which rules the ice creep behavior. In summary, it can be stated that subglacial lakes crucially affect the velocity and direction of the ice flow as well as the thermal regime of the ice sheet.

3.1.2 *Detection methods*

The detection of subglacial lakes beneath the Antarctic Ice Sheet which is featuring ice thicknesses of over 4 000 m is a challenging task. Here, a short description of the most common techniques used and developed within the last five decades is presented: the identification of subglacial lakes by radio-echo sounding (RES), satellite-based ice surface altimetry and seismic explorations (Fig. 9).

RADIO-ECHO SOUNDING   The technique of RES takes advantage of the ability of electromagnetic waves to travel comparatively freely through both air and ice. These waves are partially reflected at boundaries between materials with different dielectric properties and therefore different speeds of wave propagation. A pair of active transmit/receive radar antennas attached to an airborne (e.g., Oswald and Robin, 1973; Blankenship et al., 2001) or ground-based vehicle (e.g., Welch and Jacobel, 2003) can thus be used to detect reflections from the base or within an ice sheet. Airborne RES with a frequency of 60 MHz is able to penetrate over 4 000 m of cold ice (e.g., Robin et al., 1977) because the Antarctic ice with its low temperatures is relatively transparent to electromagnetic radiation at this frequency (Johari and Charette, 1975). The basal reflection strength depends predominantly upon the difference in dielectricity of the ice (ϵ=3.2, Bohleber et al., 2012) and the underlying material. Because the dielectric constant of water (ϵ=81) is much higher than the one of bedrock (ϵ=4 to 9) the ice-water interface causes the much stronger reflection (Fig. 9a). Additionally, the bedrock surface which is rough compared to the smooth water surface of a subglacial lake scatters the wave energy, decreasing its reflection strength further (Siegert, 2000). Consequently, subglacial lakes can be identified on RES records by specular or mirror-like reflections with an echo strength being 10-20 dB brighter than reflections from ice-bedrock interfaces. The depth of subglacial lakes can not be determined by RES because the majority of the electromagnetic radiation is reflected at the lake surface. The transmitted part is quickly absorbed and therefore does not yield enough energy to be recorded at the ice sheet surface.

ICE SURFACE ALTIMETRY   Above subglacial lakes the shear stress at the ice-water interface tends to zero and the overlying ice sheet is floating in hydrostatic equilibrium. Thus, the ice sheet surface within the confines of

(a)

(b)

(c)
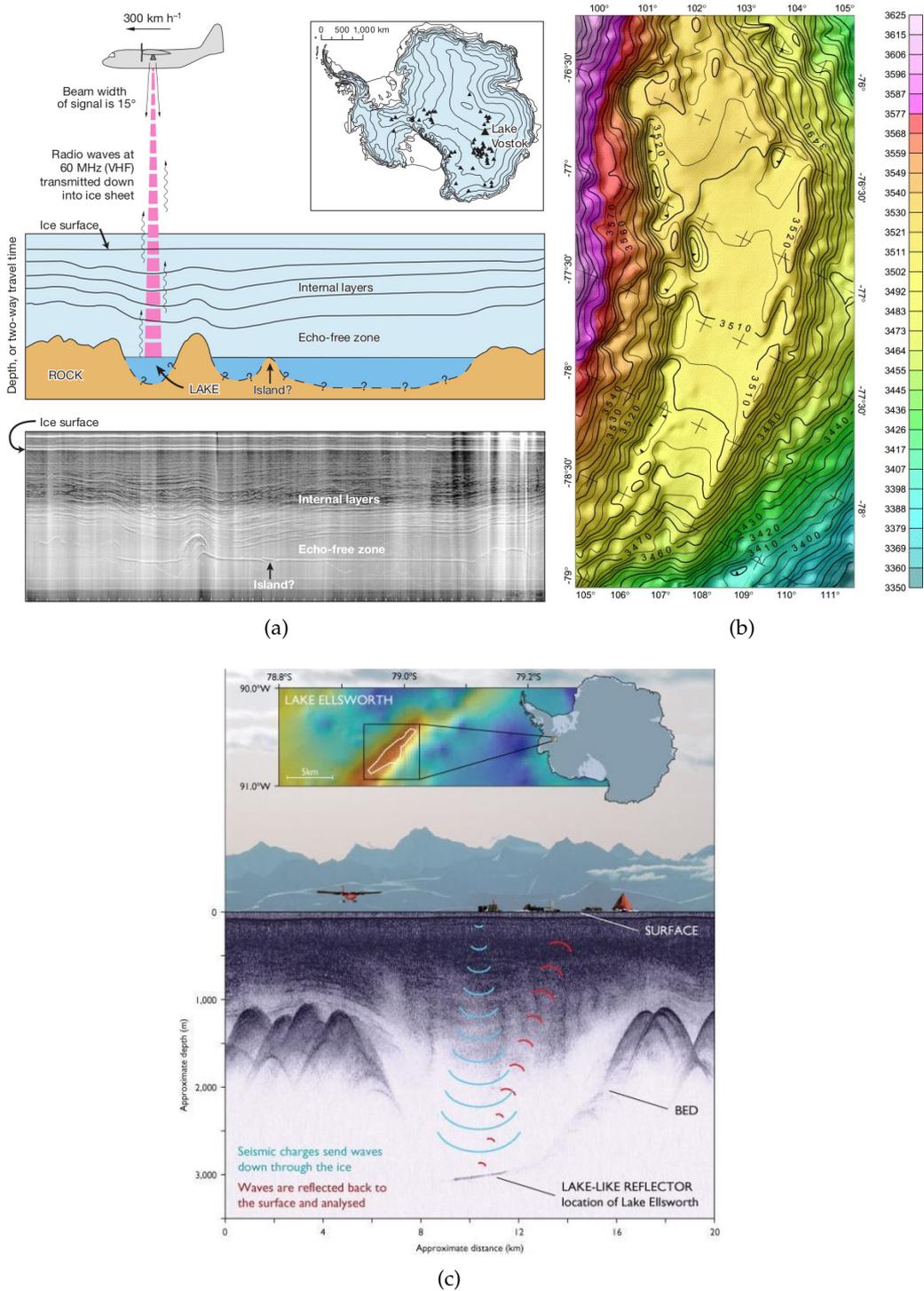
Figure 9: Detection of subglacial lakes. (a) Airborne radio-echo sounding (RES) features bright and flat reflections from water surfaces at the ice base (Fig. by Siegert et al., 2001). (b) Ice surface topography from laser altimeter and ice-penetrating radar measurements. The flat featureless region in the center of the image shows the floating ice over Lake Vostok (Fig. by Studinger et al., 2003). (c) Seismic exploration of subglacial Lake Ellsworth, seismic charges (blue) send waves down through the ice which are reflected back to the surface (red) and analyzed (Fig. by British Antarctic Survey, 2008).

the subglacial lake appears flat and featureless, similar to a floating ice shelf (Fig. 9b). Lakes smaller than 4 km across are not found to have this corresponding flat ice surface because the ice above is neither in hydrostatic equilibrium nor damps the small basal flow perturbations (e.g., Wright and Siegert, 2011). Satellite-based altimetry is a method which provides ice surface elevation data within an accuracy of a few tens of centimeters and thus has the potential to identify the locations and outlines of subglacial lakes by observing the corresponding flat surface areas (e.g., Bell et al., 2007; Smith et al., 2009). It can be distinguished between satellite radar and laser altimetry which both have their advantages. Satellite radar altimetry by, e.g., the satellites ERS-1/2 (European Remote Sensing satellites), ENVISAT (ENVIronment SATellite) (e.g., Roemer et al., 2007) and CryoSat-2 (e.g., Wingham et al., 2006a) measures the elevation averaged over a footprint of about 15 km unaffected by cloudage but needs corrections for measuring inclined surfaces. Satellite laser altimetry by, e.g., ICESat (e.g., Studinger et al., 2003; Pritchard et al., 2012) has a relatively small footprint of about 70 m but requires a clear sky and has to deal with uncertainties related to laser mispointing. Observed short-term topographical ice surface changes can be also used to detect so far unknown lakes (e.g., Wingham et al., 2006b). However, they are also used to estimate the volume of basal water drainage events and are therefore discussed in the next section.

SEISMIC EXPLORATION   Explosives are buried up to tens of meters below the ice surface to act as sources for seismic explorations (e.g., Peters et al., 2008; Woodward et al., 2010). Their detonation generates elastic waves, which propagate within the ice until they are scattered by any obstacles like bedrock or water surfaces. The reflections are detected by geophones lined up at the surface and analyzed (Fig. 9c). A new seismic exploration approach uses a truck-mounted vibrator as seismic source. In contrast to the impulsive characteristics with durations of milliseconds related to an explosive source a controlled vibrator emits energy as a finite amplitude pressure pulse over many seconds. Energy losses by inelastic behavior are thus much less because of reduced instantaneous forces (Eisen et al., 2010). Seismic explorations are time and labor intensive to carry out and therefore not suitable for large-scale investigations of the Antarctic Ice Sheet. They are more appropriate to locally confirm deductions about the subglacial environment from RES and satellite altimetry surveys. In addition, seismic explorations are capable of measuring the depth and thus the volume of subglacial lakes .

3.1.3 *History, inventory and occurrence*

In 1960 Russian pilots observed persistently flat regions on the surface of the East Antarctic Ice Sheet and used them as navigational aids, unwitting that they are related to lakes beneath the ice sheet (Robinson, 1960). In 1967 the first subglacial lake was discovered using RES near the Russian Sovetskaya Station
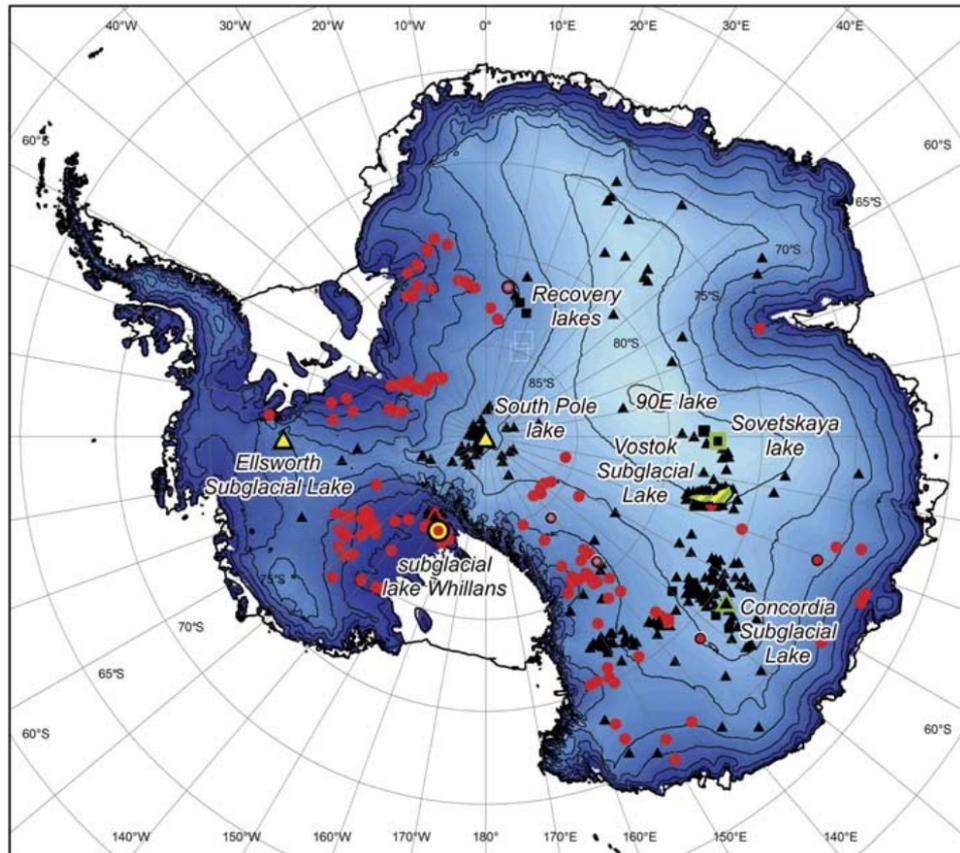
Figure 10: Map of Antarctica showing contours of ice sheet elevation and all currently
known lakes which were investigated by RES (black triangle), seismic sound-
ing (yellow triangle), gravitational field mapping (green triangle), surface
height change measurement (red circle), shape identified from ice surface
feature (square). Vostok Subglacial Lake is shown in outline. (Fig. by
Wright and Siegert, 2012)

by Robin et al. (1970), quickly followed by the detection of 17 more lake-type basal reflections in that region (Oswald and Robin, 1973). Ridley et al. (1993) identified the outlines of a large lake from ERS-1 satellite data below the Russian Vostok Station. In combination with RES observations and reanalysed seismic data from 1963/64 Kapitsa et al. (1996) identified the contemporary largest and deepest Antarctic subglacial lake, Lake Vostok. Henceforth, the number of discovered subglacial lakes increased steadily. Siegert et al. (1996) listed 77 lake locations in their inventory in 1996 and until 2005 already 145 subglacial lakes were surveyed (Siegert et al., 2005). ICESat laser altimetry investigations by Smith et al. (2009) added another 130 subglacial lakes to the inventory and extensive RES campaigns eventually lead to the number of 379 presently known subglacial lakes in Antarctica (Wright and Siegert, 2012). The largest subglacial lake, Lake Vostok, measures 280×44 km with a surface area of $14\,000$ km^2 and a maximum lake depth of $1\,100$ m (Studinger et al., 2004; Filina et al., 2008). Other prominent large lakes are the four Recovery Lakes ($1\,500$-$4\,500$ km^2), 90 Degree East Lake ($2\,000$ km^2), Sovetskaya Lake ($1\,600$ km^2), Adventure Trench Lake (780 km^2), Concordia Lake (617 km^2), South Pole Lake (42 km^2), Subglacial Lake Ellsworth (28.9 km^2), Vincennes Lake (26.6 km length) and Aurora Lake (18.3 km length) (Surface areas/lake lengths by Wright and Siegert, 2012) (Fig. 10).

The discovered Antarctic subglacial lakes are not equally distributed over the entire ice sheet because their occurrence requires two local conditions: First, the ice sheet base must be at its pressure melting point to generate melt water. Second, appropriate topographic hollows must exist to allow this water to accumulate. The ice sheet above subglacial lakes is floating in hydrostatic equilibrium, meaning that the water pressure is equal to the overburden ice pressure. Consequently, an existing gradient of the ice thickness causes an inclination of the lake-ice surface which is about 10 times (the exact value depends on the ice density) reverse to the ice surface slope. Hence, subglacial lakes can only arise in bedrock hollows with gradients being greater than 10 times the reverse ice sheet surface slope (e.g., Shreve, 1972; Siegert, 2002). Subglacial lakes therefore preferably occur in regions with low surface slopes. The distribution of the identified subglacial lakes in Fig. 10 shows that their majority and especially the large lakes are grouped within 200 km of an ice divide (Dowdeswell and Siegert, 2003). There, the ice surface slopes are low and the ice sheet reaches its maximum thickness and thus sufficiently isolates the ice base from the low surface temperatures allowing the geothermal heat flow to cause basal melting. A clustering of lakes within coastal regions associated with fast ice-flow is striking, too (e.g., within the Recovery Ice Stream downstream of the Recovery Lakes, Smith et al., 2009) (Fig. 10). Fast flowing ice streams have low surface gradients (e.g., Bennett, 2003) and could produce basal melt water by frictional heating or sediment deformation due to their high basal sliding rates (e.g., Beem et al., 2010) or receive upstream generated
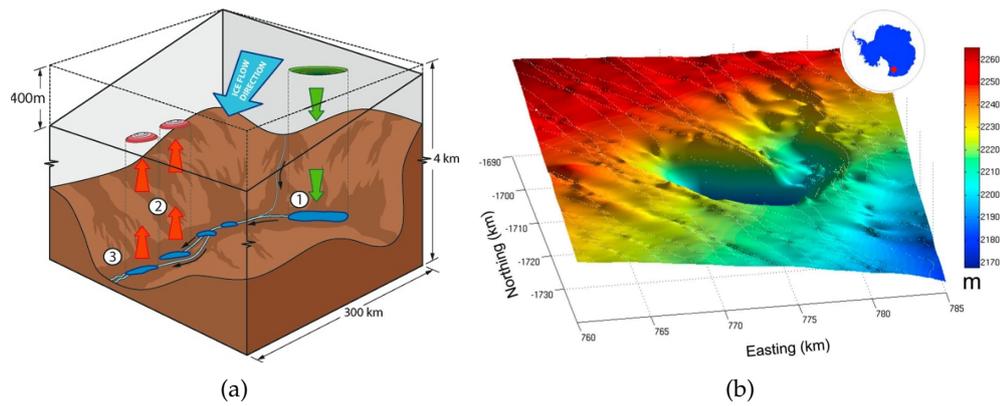
Figure 11: Active subglacial lakes: (a) Schematic illustration of correlated ice surface lowering (green) and uplift patterns (red) above adjacent subglacial lakes indicating that these lakes are linked (Fig. by SCAR). (b) Ice sheet surface deformation caused by the drainage of subglacial Lake Cook, mapped by CryoSat-2 interferometric mode data (Fig. after McMillan et al., 2013).

melt water from their tributaries (e.g., Joughin et al., 2004).

3.2 SUBGLACIAL WATER FLOW

3.2.1 *Observations and estimates*

Water flow beneath the Antarctic Ice Sheet eludes a direct monitoring. However, observations of interactions between subglacial lakes over several hundred kilometers indicate that these lakes are not isolated and distinct subglacial hydrological networks exist (Wingham et al., 2006b; Fricker et al., 2007; Carter et al., 2009b; Fricker et al., 2010; Fricker and Scambos, 2009). Satellite-based observations of short-term ice surface elevation changes are interpreted as an implication of filling or discharge of so-called *active* subglacial lakes (e.g., Smith et al., 2009; Carter et al., 2009b). The extent of detected surface deformations with timescales of months or years can be used to indirectly estimate the volume of such basal water movements (Fig. 11). Deduced volume fluxes vary from about 1 to 20 m^3 s^{-1} (Gray et al., 2005; Fricker and Scambos, 2009). In some cases up to 40 m^3 s^{-1} (Wingham et al., 2006b; Fricker et al., 2007) and even peak values of about 300 m^3 s^{-1} (e.g., Carter and Fricker, 2012) are estimated.

3.2.2 *Water flow regimes*

For the transport of water at the base of an ice sheet there are two fundamental water flow regimes: channelized and distributed flow systems (e.g., Fountain and Walder, 1998; Hewitt et al., 2012; Schoof et al., 2012). Both can exist in parallel and have different characteristics. Depending on the prevailing water pressure and the local geological properties at the ice base one regime can

(a)   (b)
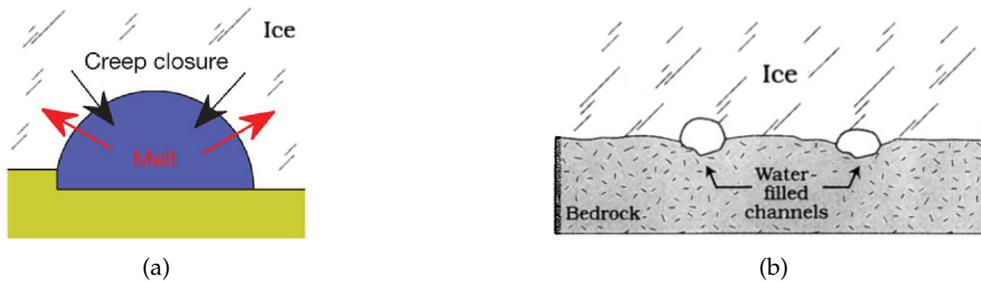
Figure 12: Channelized water flow: (a) Schematic semicircular Roethlisberger channel (cut into the ice base) which size is determined by the relation between melting and creep closure (Fig. after Schoof, 2010). (b) Nye channels (cut into the subglacial bedrock) may be accompanied by Roethlisberger channels incised into the ice above (Fig. by Fountain and Walder, 1998).

dominate the water drainage (e.g., Flowers et al., 2004; Schoof, 2010; Hewitt, 2011; Sundal et al., 2011). Both regimes are described as follows:

CHANNELIZED FLOW   Channels at the ice-bedrock interface transport basal melt water at high effective pressure (ice overburden pressure minus water pressure) (Shreve, 1972). The energy dissipated by the friction of fast flowing water melts the ice at the roof of the channel and counteracts the tendency for ice creep (caused by the overburden ice pressure) to close the channel (Fig. 12a). As a result, channel sizes rapidly adapt to the amplitude of prevailing water fluxes (e.g., Spring and Hutter, 1982). The effective pressure increases (water pressure decreases) with increasing water flux. Hence, bigger channels attract water from smaller ones and grow at their costs. This leads to the formation of an effective arborescent channel drainage structure (e.g., Schoof, 2010). Consequently, channelized systems are spatially concentrated and transport large volumes of water. Examples of channelized systems include Roethlisberger channels incised into the ice base (Roethlisberger, 1972) (Fig. 12a) and Nye channels cut into bedrock (Nye, 1973) (Fig. 12b). Channelized systems act to reduce slip by drawing water from off-axis flow and increasing coupling there. Their net effect is to reduce ice slip and thus ice discharge.

DISTRIBUTED FLOW   Distributed systems are laterally extensive and transport a small volume of water at low effective pressure. One example for distributed water flow is given by systems of linked and water-filled cavities (Lliboutry, 1968; Fowler, 1986; Gagliardini et al., 2007). They emerge by the ice flowing over bedrock bumps and forming cavities at their lee sides. The size of each cavity is mainly governed by the size and form of the obstacle at the ice base, by the ice sliding velocity and by the ice overburden pressure which tends to close the cavity by ice creep (Fig. 13a). Such cavities are connected by small orifices which are the major restriction for water flow in cavity networks and thereby keep the effective pressure in the entire system down. An idealized subglacial cavity network is shown in Figs. 13b and 13c where a plan view
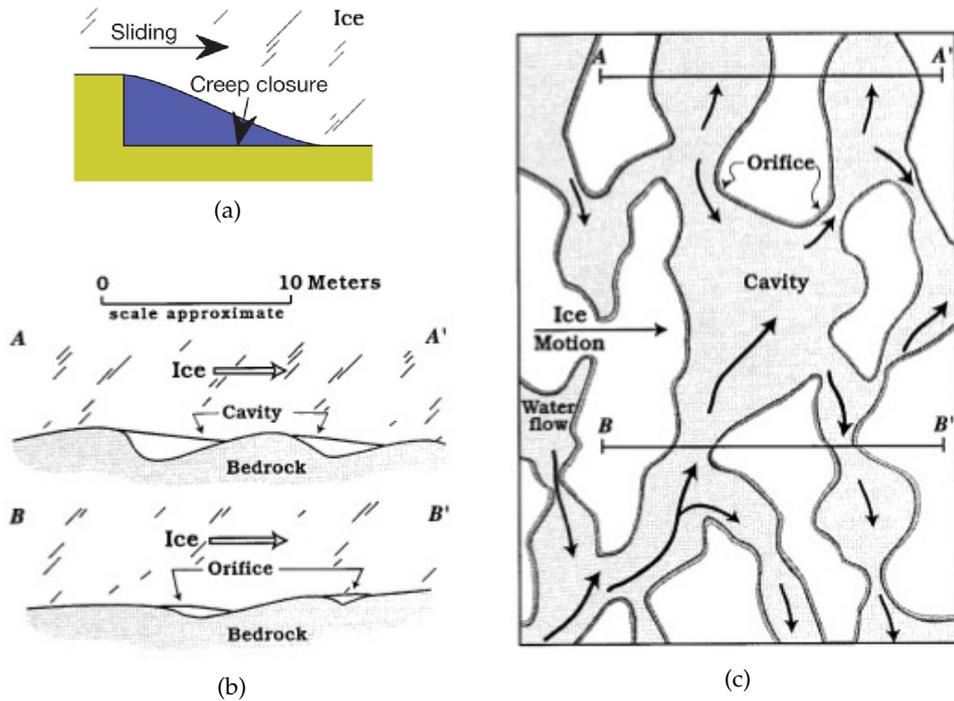
Figure 13: Distributed water flow through linked cavities: (a) Schematic basal ice cavity behind a bedrock protrusion. Its size is defined by the interplay between ice sliding and creep closure (Fig. after Schoof, 2010). (b) and (c) Idealized network of linked cavities at the ice base. The white areas in the plan view show grounded ice, the gray areas are water-filled basal cavities connected by orifices and the arrows indicate the water flow directions. The cross sections reveal the limiting impact of the orifices on the water flow of the system (Figures by Fountain and Walder, 1998).
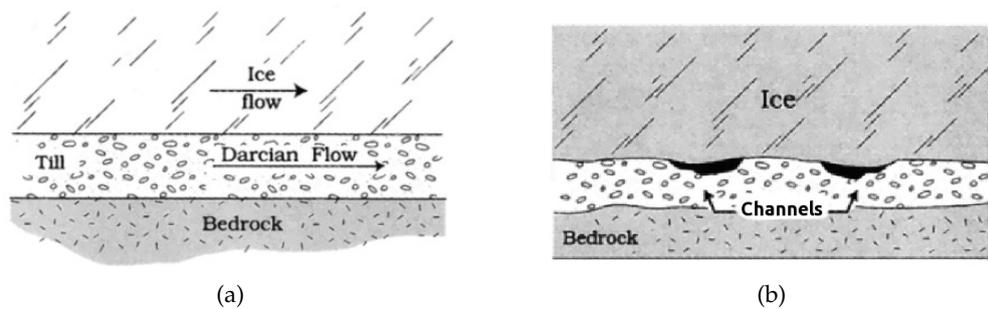
Figure 14: Distributed water flow: (a) Darcian flow within till or sediment at the ice base. (b) Flow in wide, shallow and ice-roofed channels cut into the till. (Figures after Fountain and Walder, 1998)

and two cross sections illustrate the key role of the orifices. Other examples for distributed flow systems are flow through a water film between ice and bedrock (Weertman, 1972) and flow within groundwater and till (Alley et al., 1986) (Fig. 14a). The water flow in channels eroded into sediment at the ice base (Fig. 14b) shows the properties of distributed flow systems, too. Walder and Fowler (1994) found that these wide, shallow and ice-roofed channels form a distributed, non-arborescent system due to the specific sediment properties and the mechanics of sediment transport. In summary, it can be stated that all these distributed water flow systems tend to enhance slip along the ice-bed interface, because effective pressure decreases with increasing water flux.

3.3 SUBGLACIAL HYDROLOGY MODELING

During the last decades promising efforts have been made to achieve mathematical descriptions of the particular flow regimes introduced above (e.g., Lliboutry, 1968; Roethlisberger, 1972; Weertman, 1972; Spring and Hutter, 1982; Fowler, 1986; Walder and Fowler, 1994; Gagliardini et al., 2007). Meanwhile, mathematical descriptions for collocated distributed and channelized water flow systems are available, too (Flowers et al., 2004; Schoof, 2010; Schoof et al., 2012; Hewitt, 2011; Hewitt et al., 2012). They are well implementable for the modeling of small mountain glaciers where high resolution data-sets of the order of hundreds of meters for ice thickness and bedrock elevation exist. However, for large ice sheets or even continental scale modeling their application is limited, since the available data base is too coarse. Locally, numerous airborne campaigns in Antarctica (e.g., IceBridge, IceCap, IceGrav) make high-resolution bedrock digital elevation models available. But for the whole Antarctic Ice Sheet typical elevation models provide the required geophysical data on a 1 to 5 km grid scale (Le Brocq et al., 2010; Fretwell et al., 2013) and still large areas of the bedrock are interpolated. Describing channelized water flux between adjacent grid cells at these scales would require the assumption of an appropriate channel density (Hewitt, 2011) or to model the hydrology at higher resolution than the bedrock topography data available and face major computational costs.

Additionally, the governing flow regime itself depends very much on the local geological properties at the ice base (Sec. 3.2.2). They might range from solid bedrock, rough debris and till, to soft sediments. For the Antarctic Ice Sheet these very important basal conditions are only known from a very sparse number of boreholes (e.g., Kamb, 2001). Thus, they are basically unknown for the majority of the Antarctic continent as the ice sheet base has been quite inaccessible for direct observations thus far. This inaccessibility means as well, that none of the existing mathematical theories for possible flow regimes can be easily proofed by in-situ explorations of the hydraulic system at the base of the Antarctic Ice Sheet.

In this study, the interactions between ice dynamics and subglacial hydrology are investigated on large and even continental scales. In order to confine the computational costs and avoid the uncertainties related to insufficient informations about the geological properties at the ice base, the focus is directed towards modeling approaches reduced to the essentials of subglacial hydrology: First, the calculation of the hydraulic potential and its gradients to determine the flow direction of basal water and to identify spots where water could accumulate and form subglacial lakes. Second, the computation of the balance flux to spatially trace subglacial water flow and obtain local balance flux rates. In the following, the primary objective is the description of distributed flow systems because they are (in contrast to channelized systems) assumed to lower the friction at the ice-bed interface and thus considerably influence the ice dynamics.

3.3.1 *Basal hydraulic potential*

Independently of the prevalent flow regime, melt water at the base of the ice sheet follows the gradient of the hydraulic potential p (Shreve, 1972)

$$p = \rho_w g z + p_w \tag{46}$$

with ρ_w the water density, g the acceleration of the gravity and p_w the water pressure at the considered point of elevation z. The effective pressure $p_{eff.}$ at the ice base is defined as the ice overburden pressure p_i minus water pressure p_w:

$$p_{eff.} = p_i - p_w. \tag{47}$$

For distributed water flow systems the assumption can be made, that the effective pressure $p_{eff.}$ is close to zero (e.g., Budd and Jenssen, 1987; Alley, 1996) and thus $p_w \approx p_i$. Sparse borehole measurements show $p_w > 0.95\,p_i$ (e.g., Kamb, 2001) and confirm this approximation. Consequently, the hydraulic potential p can be approximated by

$$p = \rho_w g z + p_i \tag{48}$$

with the ice pressure $p_i = \rho_i g H$, where H is the ice thickness and ρ_i the ice density. For reasons of vividness Eq. 48 with $[p] = Pa$ is converted into the water equivalent hydraulic potential $P = p/(\rho_w g)$ with $[P] = m$ a.s.l., obtaining

$$P = B + H\,\frac{\rho_i}{\rho_w} \tag{49}$$

where B is the bedrock elevation. The calculation of the hydraulic potential for distributed water flow (Eq. 49) was implemented in the *Revised Ice Model Based on Frank Pattyn* (RIMBAY).

(a) Simple hollow
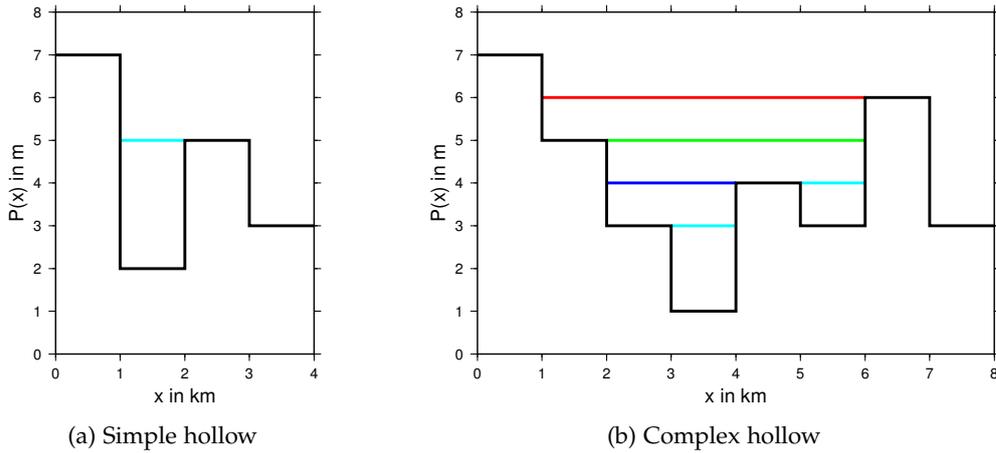
(b) Complex hollow

Figure 15: Hollow filling algorithm, applied to a one-dimensional hydraulic potential P(x): (a) Simple hollows are set to their lowest neighbor (cyan). (b) More complex hollows are iteratively filled up (in the following order: cyan, blue, green, red). The concept can be extended for the application to two-dimensional hydraulic potentials.

3.3.2 *Filling of hydraulic potential hollows*

A natural hydraulic potential surface (Eq. 49) defined by a realistic bedrock and ice sheet topography most likely contains several local minima or hollows. The upstream hydraulic potential area of a hollow is called its catchment area. The flow of basal water generated in this area follows the hydraulic gradient towards the hollow. Under the precondition that the ice base adjacent to a hollow in the hydraulic potential is at its pressure melting point, melt water can accumulate in the hollow and form a subglacial lake. This finding can be used to predict locations and extents of potential subglacial lakes by identifying and filling the hollows of a given hydraulic potential.

A filling algorithm was developed and implemented in RIMBAY which includes the filling of adjacent hollows and is therefore nontrivial. In an iterative way all minima in the potential are identified and set to the value of their lowest neighbor until no more minima exist. A tree search algorithm ensures, that minima are identified, too, which consist of adjacent grid cells with exactly the same value surrounded by higher values (Fig. 15).

3.3.3 *Balance flux*

A well established method to trace the paths of subglacial melt water is the balance flux concept (Quinn et al., 1991; Budd and Warner, 1996; Tarboton, 1997; Le Brocq et al., 2006, 2009). This concept is easy to implement, fast and well applicable to continental scale modeling (e.g., Pattyn, 2010). The approach makes the assumption that the water pressure is equal to the overburden ice pressure and thus only includes distributed flow. It presumes a basal hydraulic system in steady state and delivers the associated water flux for every grid cell, but

does not describe water pressures. Below, the concept and its implementation are introduced and some basic examples are presented.

CONCEPT   In a two-dimensional horizontal (x, y) domain, where $M_b(x, y)$ is the basal melt rate as water volume equivalent, $\bar{v}^{(w)}(x, y)$ is the vertical averaged water velocity and $W(x, y)$ is the thickness of the water layer, the steady-state balance condition reads

$$\operatorname{div}\left(W \bar{v}^{(w)}\right) = M_b \tag{50}$$

with the divergence operator div. Using Gauss's divergence theorem Eq. 50 can be expressed in its integral form:

$$\iint_S M_b \, dx \, dy = \int_C W \bar{v}^{(w)} \cdot \vec{n} \, dl. \tag{51}$$

Here, the gain of melt water within any closed area S in the (x, y) domain balances the net outward water flow through its boundary C with length l and the outward pointing unit vector $\vec{n}$. The right-hand term in Eq. 51 represents the scalar volume flux Φ with $[\Phi] = \mathrm{m}^3 \, \mathrm{a}^{-1}$ which can be calculated for any section C' of the boundary with

$$\Phi = \int_{C'} W \bar{v}^{(w)} \cdot \vec{n} \, dl. \tag{52}$$

A horizontal vector flux density ϕ with $[\phi] = \mathrm{m}^2 \, \mathrm{a}^{-1}$ is given by

$$\phi = W \bar{v}^{(w)}. \tag{53}$$

Its spatial distribution $\phi(x, y)$ is commonly referred to as the balance flux distribution.

IMPLEMENTATION   Under the assumption that water flow follows the steepest gradient of the hydraulic potential (Eq. 48), the balance flux concept can be implemented following three different algorithms (Quinn et al., 1991; Budd and Warner, 1996; Tarboton, 1997). All of them yield the balance flux $\phi_{i,j}$ (Eq. 53) at every grid point (i, j) for a finite differences discretization with a rectangular (x, y) grid of grid spacing Δx and Δy. However, the three algorithms differ in the number of adjacent grid cells which are locally involved in the calculation of the balance flux, illustrated in Fig. 16. A comprehensive comparison of these different schemes is given by Le Brocq et al. (2006).

In RIMBAY, the algorithm of Budd and Warner (1996) was implemented (Fig. 16a). It uses the four nearest neighbor grid cells to solve Eq. 50. In the following, a detailed description of the implementation is given: The gradients $P^x_{i,j}$ and $P^y_{i,j}$ of the hydraulic potential $P_{i,j}$ are expressed by central differences as

$$P^x_{i,j} = \frac{P_{i+1,j} - P_{i-1,j}}{2\Delta x} \qquad P^y_{i,j} = \frac{P_{i,j+1} - P_{i,j-1}}{2\Delta y} \tag{54}$$

| (a) Budd and Warner | (b) Quinn | (c) Tarboton |
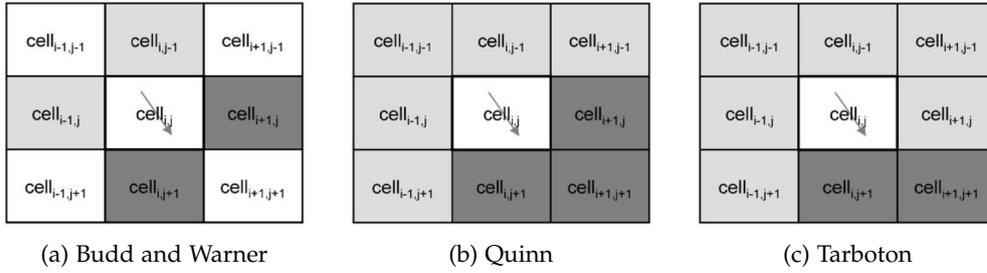
Figure 16: Schematic diagrams to illustrate the differences of the algorithms by (a) Budd and Warner (1996), (b) Quinn et al. (1991) and (c) Tarboton (1997). For the central grid cell (i, j) the flow direction $\theta_{i,j}$ is indicated by an arrow, the potentially water-contributing grid cells are marked in light gray and the water receiving grid cells in dark gray (Figures by Le Brocq et al., 2006).

with a magnitude of

$$\bar{P}_{i,j} = \sqrt{\left(P_{i,j}^x\right)^2 + \left(P_{i,j}^y\right)^2}. \tag{55}$$

The direction of the water flow at an angle θ to the x axis is given by

$$\cos\theta_{i,j} = \frac{P_{i,j}^x}{\bar{P}_{i,j}} \qquad \sin\theta_{i,j} = \frac{P_{i,j}^y}{\bar{P}_{i,j}}. \tag{56}$$

Rewriting Eq. 51 leads to an expression for the total scalar volume flux $\Phi_{i,j}^{(out)}$ *out* of the (i, j) grid cell with

$$\Phi_{i,j}^{(out)} = M_{b\,i,j}\Delta x\Delta y + \Phi_{i,j}^{(in)} \tag{57}$$

where the total scalar influx of water $\Phi_{i,j}^{(in)}$ is the sum of outflow contributions of next-neighbor upstream grid cells. The apportionment of the water outflow towards the downstream grid cells is estimated by the direction of the water flow with angle $\theta_{i,j}$ (Eq. 56) leading to

$$
\begin{aligned}
\Phi_{i,j}^{x(out)} &= \frac{\left|\cos\theta_{i,j}\right|}{\left|\sin\theta_{i,j}\right| + \left|\cos\theta_{i,j}\right|}\,\Phi_{i,j}^{(out)} \\
\Phi_{i,j}^{y(out)} &= \frac{\left|\sin\theta_{i,j}\right|}{\left|\sin\theta_{i,j}\right| + \left|\cos\theta_{i,j}\right|}\,\Phi_{i,j}^{(out)}.
\end{aligned}
\tag{58}
$$

Consequently, the scalar outflux for all grid cells can be calculated by sorting and treating all grid cells in order of descending hydraulic potential $P_{i,j}$, because the outflux $\Phi_{i,j}^{(out)}$ in Eq. 57 is always given by the local melt rate and the influx from the previously treated upstream grid cells. The vector flux $\phi_{i,j}$ into the direction of the flow angle $\theta_{i,j}$ at the center of a grid cell is obtained by

$$\phi_{i,j} = \frac{\Phi_{i,j}^{(out)}}{L\left(|\cos\theta_{i,j}| + |\sin\theta_{i,j}|\right)} \tag{59}$$

where $L = \Delta x = \Delta y$ is the side length of the grid cell.
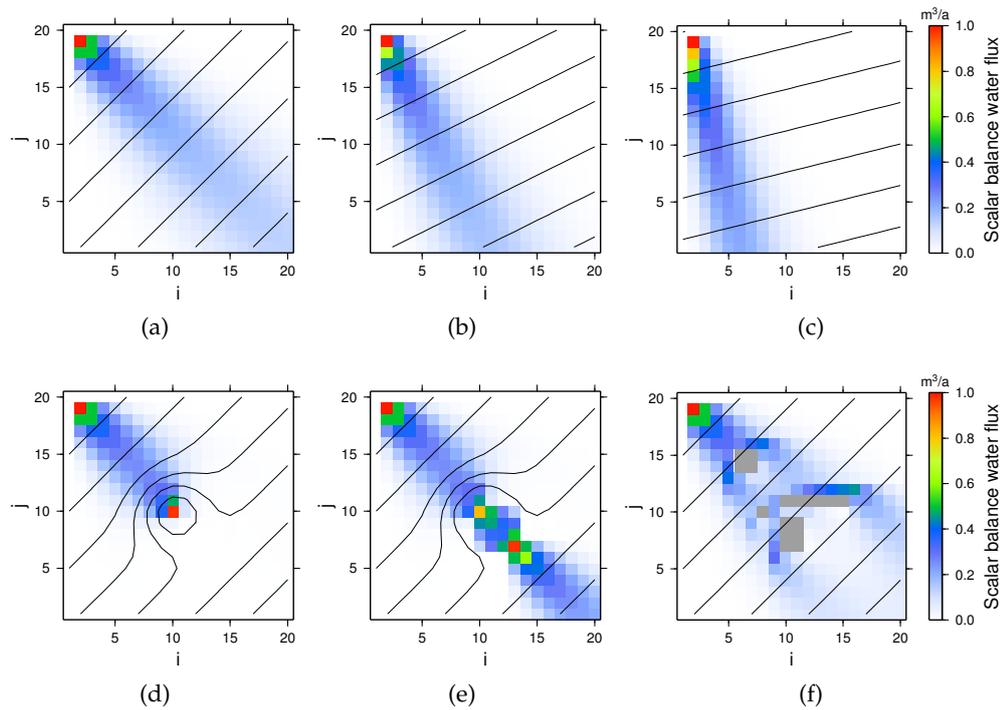
Figure 17: Scalar balance water flux on an inclined plane following the Budd and Warner (1996) scheme (Fig. 16a) by RIMBAY. Only at grid cell $(i, j) = (2, 19)$ a basal melt rate M_b of $1\,\mathrm{m\,a^{-1}}$ is defined. The hydraulic potential is illustrated by its equipotential lines. (a-c) Flux for different grid orientations. (d) Flux is ending in a hollow of the hydraulic potential. (e) Flux crosses the hollow after modification of the hydraulic potential. (f) Flux is directed around obstacles, e.g., Nunataks (gray).

APPLICATION   Scalar balance water fluxes computed by RIMBAY for several idealized setups are illustrated in Fig. 17. The model domain comprises an area of 20×20 grid cells with a grid spacing of 1 m. The basal melt rate is set to $1\,\mathrm{m\,a^{-1}}$ at one grid cell in the upper left corner of the model area and is zero everywhere else. Figures 17a, 17b and 17c show the water flux across an inclined plane with different orientations of the steepest gradient towards the grid orientation. The water flux follows the hydraulic gradient showing a clearly diffusive behavior. The level of diffusivity is influenced by the grid orientation (Le Brocq et al., 2006).

An obvious weakness of the balance flux concept is demonstrated in Fig. 17d where additionally a hollow is defined in the hydraulic potential. The upstream generated melt water follows the hydraulic gradient and is directed into the hollow where the flux ends and thus not contributes to downstream water flux. However, the concept of the balance flux calculation assumes a hydraulic system in steady state. Under that condition the hollow should be filled with water and provide a continuous overflow at the lowest point of its rim. In order to simulate this the hydraulic potential is modified in RIMBAY before the calculation of the balance flux following two steps: First, all hollows in the hydraulic potential (Sec. 3.3.2) are identified and filled. As a result, flats emerge at the potential surface where the hydraulic gradient (Eq. 54) is zero and no flux direction (Eq. 56) can be computed. To overcome this, every flat is slightly tapered into the direction of its previously identified discharge point (Goeller et al., 2013). This approach ensures that all melt water produced inside the model domain reaches its margins. Particularly hydropotential surfaces of realistic model domains exhibit numerous hollows where upstream flux contribution would vanish without the above modifications. Figure 17e shows the modified hydraulic potential from Fig. 17d and how the flux is subsequently able to cross the filled-up and tapered hollow. Other authors (e.g., Le Brocq et al., 2009; Pattyn, 2010) follow an alternative approach to guarantee flux conservation by iteratively setting all minima in the hydraulic potential to the value of their neighbor's mean. In comparison to the above introduced algorithm this approach has the lower computational costs but tends to alter the locations where filled hollows overspill.

A balance flux algorithm for the computation of water flux beneath ice sheets should also take into account the possible presence of obstacles, e.g., Nunataks. They are defined as bedrocks which are locally protruding from the ice sheet. Following the definition of the hydraulic potential (Eq. 49) they act as a potential barrier for the basal water flux. In the ice model RIMBAY grid cells can be defined as Nunataks independent of their hydraulic potential. An extra check in the implementation ensures the redirection of the water flux around them, shown in Fig. 17f.

MODELING ANTARCTIC SUBGLACIAL HYDROLOGY

For the study of the hydraulic system beneath the Antarctic Ice Sheet the above introduced hydraulic modeling approaches are applied on a continental scale. In this way, insights into the topography of the basal hydraulic potential are gained and locations and extents of potential subglacial lakes can be predicted. This method is evaluated by a comparison of the results with the latest inventory of Antarctic subglacial lakes and a selective interpretation of radar profiles from radio-echo sounding (RES) flight campaigns by the Alfred Wegener Institute (AWI). The findings are used to estimate the number and extent of Antarctic subglacial lakes yet to be discovered. In addition, the pathways of basal melt water are simulated allowing the analysis of general drainage patterns, particular lake drainage pathways and the correlation between basal hydrology and observed ice velocities.

4.1 BASAL HYDRAULIC POTENTIAL

The hydraulic potential (Shreve, 1972) at the base of the Antarctic Ice Sheet is defined by basal water pressure and bedrock elevation. Its gradients determine the flow of basal melt water which can accumulate in hollows of the hydraulic potential, forming subglacial lakes. These subglacial lakes belong to the distributed flow systems (Sec. 3.2.2) and therefore it is presumed that the effective pressure (ice overburden pressure minus water pressure) at the ice base above a subglacial lake is zero. This assumption allows to simplify the calculation of the hydraulic potential when the primary focus is on the investigation of distributed flow systems, respectively subglacial lakes. In that case, the hydraulic potential at the base of grounded ice can be calculated using bedrock elevation and ice pressure derived from ice thickness and ice density (Eq. 49, Sec. 3.3.1). The respective data sets for Antarctica are provided within the Bedmap2 data set (Fretwell et al., 2013) and are resampled to a grid resolution of 5 km.

Figure 18 shows the bedrock elevation, the calculated hydraulic potential and the surface elevation for the Antarctic Ice Sheet. The bedrock topography features distinct mountain ranges as well as regions with lower surface roughness. Elevations range from about -2 500 m in deep troughs beneath the central West Antarctic Ice Sheet (WAIS) to above 4 000 m in the Ellsworth and Transantarctic Mountains. About 45 % of the Antarctic bedrock (beneath grounded ice) are identified to be below sea level. Certain areas of the Antarctic bedrock in Fig. 18 seem quite featureless. They result from large-scale interpolations because locally only very sparse measured points are available. The ice sheet surface appears relatively smooth due to the flow properties of ice
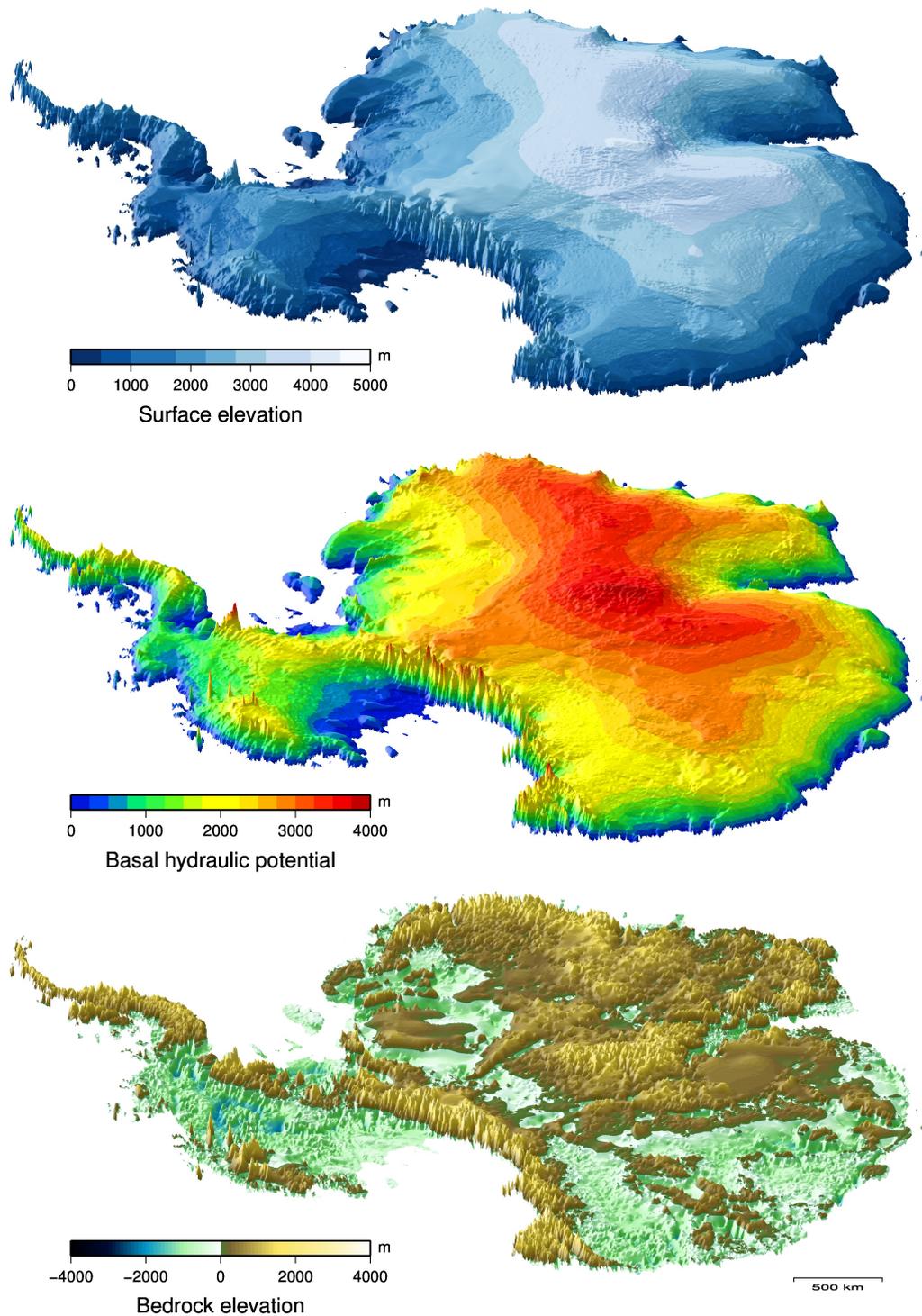
Figure 18: Surface and bedrock elevation (Bedmap2 data set, Fretwell et al., 2013) and calculated basal hydraulic potential for the Antarctic continent (confined to areas of grounded ice). The hydraulic potential is mainly influenced by the surface elevation but shows the attenuated imprint of the bedrock topography. Discussed geographical features are labeled in Fig. 2, Sec. 1.1.

which tends to equalize differences in surface elevation by internal deformation. The East Antarctic Ice Sheet (EAIS) rises above 4 000 m in its central part while the ice sheet surface is decreasing towards the coasts. The hydraulic potential is reflecting the combined influence of bedrock elevation and ice pressure and lies well defined above sea level. Its elevation is mainly governed by the elevation of the ice sheet but it does not show the smoothness of the ice surface. Instead, the surface of the hydraulic potential reflects the spatial variability of the bedrock elevation in an attenuated form.

4.2 PREDICTING SUBGLACIAL LAKES

In this section, positions and extents of subglacial lakes in Antarctica are predicted following a method which is solely based on the observed topography of the Antarctic Ice Sheet and the underlying bedrock.

4.2.1 *Assumptions and method*

Model results of Pattyn (2010) show that about 55 % of the Antarctic Ice Sheet base is at its pressure melting point and could produce melt water while the rest of the ice sheet might be frozen to the bedrock. The underlying ice temperature calculation (Eq. 38, Sec. 2.2.3) which is commonly used for ice flow modeling considers (besides advection and diffusion terms) several thermal influences: Internal heating by internal ice deformations and the mean annual air temperature at the ice sheet surface as well as the combined influence of the geothermal heat flux and frictional heat contributions at the ice-bed interface, resulting from the ice sliding over the bed. Especially these basal processes are assumed to have the major impact on the thermal balance of the ice sheet. The sliding of ice over bedrock is described by a number of theories (review by Fowler, 2010) which unfortunately can not be approved by observations due to the inaccessibility of the Antarctic Ice Sheet's base. The available geothermal heat flux data sets (Shapiro and Ritzwoller, 2004; Maule et al., 2005) show large differences and also a lack of confirmation by direct measurements. Consequently, the implementation of the thermally relevant basal processes in ice modeling is still on a very basic level and subject to large uncertainties.

In the following, it is assumed for reasons of simplicity that the whole Antarctic Ice Sheet base is at its pressure melting point and produces melt water, possibly leading to an overprediction of subglacial lakes which is corrected in Sec. 4.4 by a validation of the results using radar observations. The melt water follows the gradient of the hydraulic potential (Eq. 48) and pools within hollows of the hydraulic potential surface. Under the assumption that the hydraulic system is acting on much smaller time scales than the ice dynamics, the hydraulic system is in a quasi-stationary equilibrium state. Accordingly, all hollows of the hydraulic potential are assumed to be filled to their maximum level forming subglacial lakes.
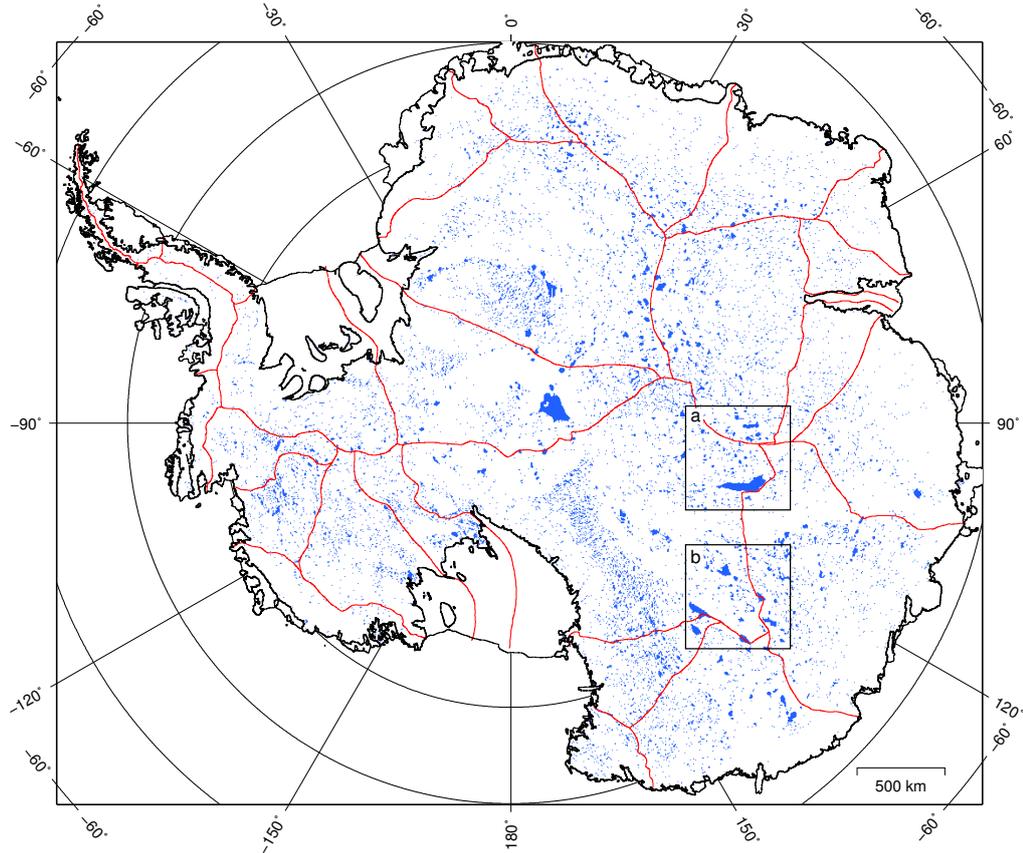
Figure 19: Antarctic Ice Sheet: Locations and extents of 10 183 predicted subglacial lakes (blue). Coast and grounding line (black) by NSIDC and ice divides (red) by AGAP. Map sections a/b are shown in detail in Fig. 22a/22b for a comparison with observed lakes.

The theoretical prediction of subglacial lakes in Antarctica is done within three steps: First, the basal hydraulic potential ic calculated as described in the section above. Second, the algorithm introduced in Sec. 3.3.2 is used to fill up all hollows in the hydraulic potential resulting in a modified hydraulic potential. And third, the predicted subglacial lake surfaces are obtained as the distribution of non-zero elements of the difference between the modified and the original hydraulic potential.

4.2.2 *Results and discussion*

With the above method, 10 183 hollows can be identified and filled in the basal hydraulic potential of the Antarctic Ice Sheet which are interpreted as potential or predicted subglacial lakes. The locations and extents of all predicted subglacial lakes are shown in Fig. 19. The majority of the lakes and particularly all larger lakes are clustered close to the ice divides. There, the ice sheet surface is relatively flat and the hydraulic potential is primarily influenced by the bedrock. Thus, troughs in the bedrock are also troughs in the hydraulic potential allowing the basal melt water to pool. Towards the ice sheet margins the lake concentration is decreasing because of the higher prevailing ice
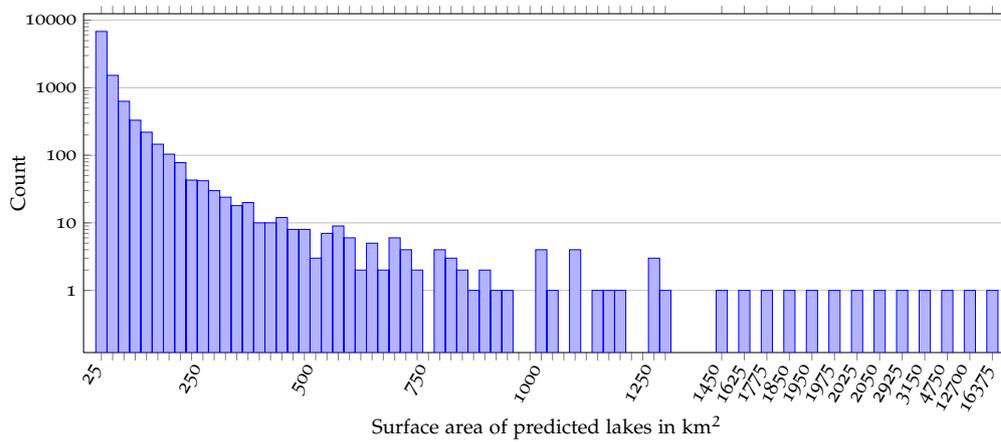
Figure 20: Surface area distribution of all 10 183 predicted lakes, linear scaled up to surfaces of 1 275 km^2 and as a list beyond.

sheet surface gradients. Their influence on the basal hydraulic potential is dominating the bedrock gradients by about one order of magnitude. As a consequence, hydraulic hollows and by association subglacial lakes occur only at comparatively deep bedrock depressions.

Furthermore, the local concentration of predicted lakes depends on the number of locally available RES flight lines which were used to reconstruct the bedrock topography. Currently, the bedrock is well surveyed in most Antarctic regions (e.g., Dronning Maud Land (DML) or the Siple Coast) but, also, there are still areas (e.g., beneath the EAIS) where it has to be reconstructed from a very sparse number of measurements (Fretwell et al., 2013). A higher resolution of the known bedrock elevation necessarily results in an increased number of hollows in the hydraulic potential and, thus, more predicted lakes. This additionally explains the spatially varying concentration of predicted lakes and is confirmed by the use of an earlier data set for Antarctic bedrock elevation and ice thickness based on far less comprehensive observations (Albmap by Le Brocq et al., 2010) where only 2 764 potential lakes are found.

Altogether, an area of 590 900 km^2 is found to be covered by surfaces of predicted Antarctic subglacial lakes (4.9 % of the area of Antarctic grounded ice). This is in agreement with estimates of Siegert (2000) stating that ≈5 % of the ice sheet base might be occupied by subglacial lakes and modeling results of Livingstone et al. (2013) who found a lake coverage of 3.7 % based on the prediction of 12 767 lakes with a similar distribution.

The areal extents of the particular predicted lakes ranges from 25 to 16 375 km^2 (Fig. 20). Their majority (6 829 lakes, 67 %) comprises surfaces of 25 km^2 corresponding to a single grid cell at the applied grid resolution of 5 km. The average lake size is 58 km^2 and only 30 predicted lakes (0.3 %) have surfaces of 1 000 km^2 and beyond.
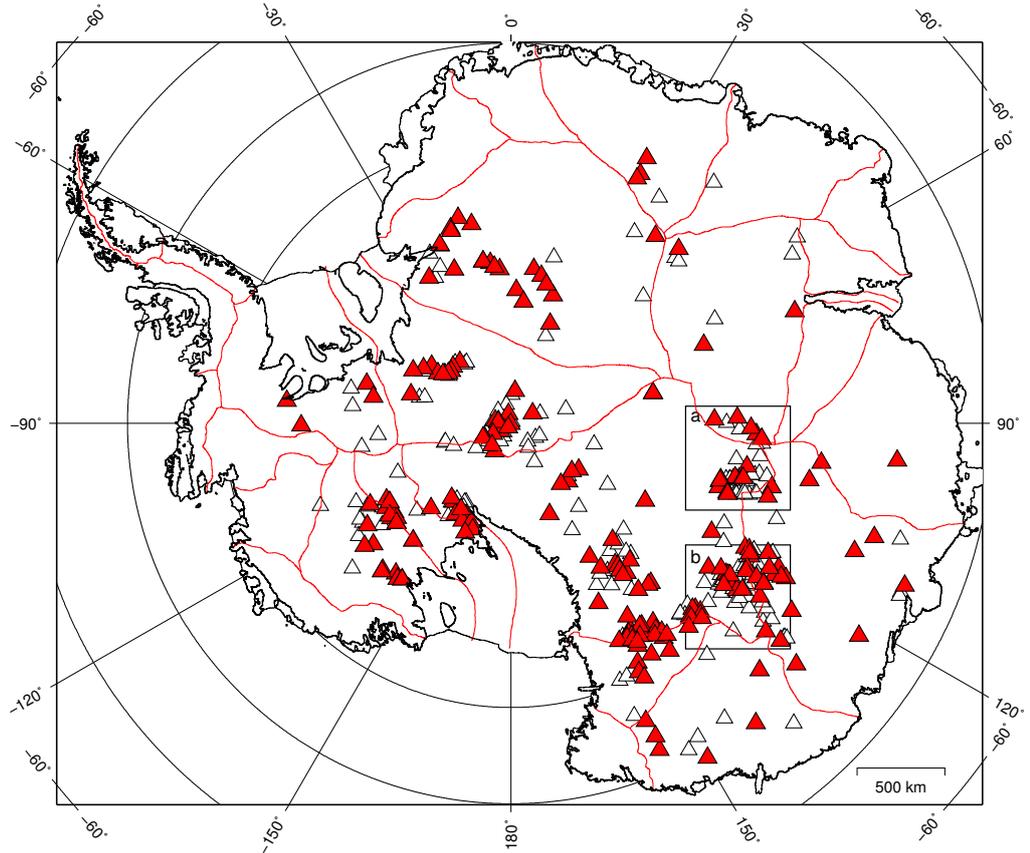
Figure 21: Antarctic Ice Sheet: Locations of all 379 observed subglacial lakes (triangles, inventory by Wright and Siegert, 2012). 206 of them (red triangles) were successfully predicted. Coast and grounding line (black) by NSIDC and ice divides (red) by AGAP. Map sections a/b are shown in detail in Fig. 22a/22b.

(a)

(b)
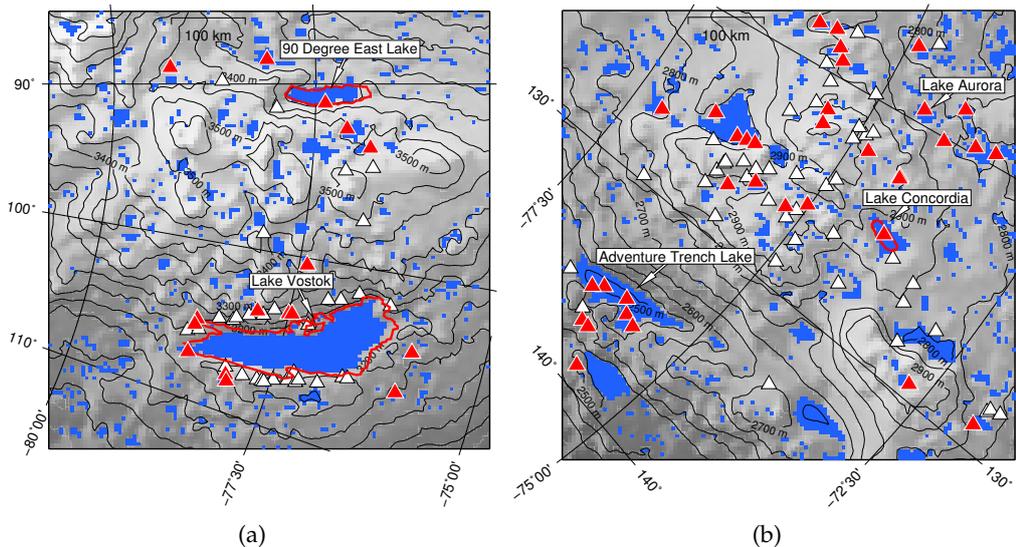
Figure 22: Hydraulic potential (gray) with predicted (blue) and observed subglacial lakes (triangles, inventory by Wright and Siegert, 2012) for two selected regions in central East Antarctica (Fig. 19 and 21). Observed lakes matching with a predicted lake are illustrated by red triangles, all other observed lakes by white triangles. Outlines of observed lakes (red lines) by Filina et al. (2008) and Studinger et al. (2003).

4.3 COMPARISON OF PREDICTED AND KNOWN SUBGLACIAL LAKES

In order to test the validity of the introduced method to predict subglacial lakes in Antarctica, the locations of the predicted lakes are compared to the locations of in situ observed subglacial lakes.

4.3.1 *Method and results*

So far, 379 lakes have been identified beneath the Antarctic Ice Sheet using satellite altimetry, airborne RES or seismic investigations. They are listed in an inventory compiled by Wright and Siegert (2012). For the following comparison, the listed geographic positions of the observed lakes are interpreted as the central lake positions, because for only 7 of these lakes an estimate of their outlines exists while for 131 lakes not even a length is given. For all predicted lakes the outlines are determined and expanded by a buffer zone of 5 km which is thought to compensate the uncertainties originating from the 5 km grid resolution. A predicted subglacial lake is considered to successfully match an observed subglacial lake if the central position of the observed lakes is situated inside the expanded outlines of the predicted lake.

With this method 206 observed Antarctic subglacial lakes (54 % of all known lakes) are found to be correctly predicted. Figure 21 shows an overview of the entire inventory of Antarctic subglacial lakes and highlights the successfully predicted lakes. Additionally, the names and geographic positions of the successfully predicted lakes are provided in a tabular form in the appendix in Sec. A.1. The area around Lake Vostok and the so-called Lake District in East Antarctica are shown in detail in Fig. 22. All larger lakes like Lake Vostok, Lake 90 Degree East, Adventure Trench Lake, Lake Concordia and Lake Aurora were successfully predicted. Particularly for the known outlines of Lake Vostok, Lake 90 Degree East and Lake Concordia the congruence with the predicted lake extents is outstanding.

4.3.2 *Discussion and implications*

The correct prediction of the majority of the known subglacial lakes demonstrates the good performance of the introduced method. In comparison, Livingstone et al. (2013) recalled 61 % of the known lakes with similar predictions but using larger buffer zones depending on the lake size for the matching. At first view, these prediction success rates are astonishing since the lake surface reflectors are incorporated in the bedrock topography and ice thickness data in the used Bedmap2 data set (Fretwell et al., 2013). For this reason, no hollows in the hydraulic potential should occur at the locations of existing subglacial lakes. Indeed, this is the case for lakes which are filled with water up to their hydraulic lip and might account for some of the observed subglacial lakes which could not been theoretically predicted. A high percentage

of the known subglacial lakes in the current inventory, however, was detected by ice sheet surface elevation changes and therefore belongs to the group of active subglacial lakes (e.g., Smith et al., 2009). These kind of lakes are periodically filling and draining and might have had an intermediate filling level at the time of the respective RES bedrock elevation and ice thickness survey. The difference between the actual lake surface and the highest possible water level would then be interpreted as hydraulic hollow and consequently as a predicted lake. Another reason for the successful identification of known subglacial lakes, despite the incorporation of the lake surface reflector in the topography data sets, could be justified by the processing of the topography data. Although the originally along-track resolution of RES records is comparatively high, the interpolation onto a grid size in the order of kilometers could smooth out the elevation of a narrow lake outlet. In this manner, the rim of an existing and water-filled basal hydraulic hollow would be artificially raised, what again leads to a detection of a hydraulic hollow and therefore to the prediction of a subglacial lake at this spot.

Interpolation artefacts, originating from bedrock geometry processing and creating hydraulic hollows, can also be a reason for the over-prediction of subglacial lakes and explain the large discrepancy between 10 183 predicted and so far only 379 observed subglacial lakes in Antarctica. Another argument to explain the above discrepancy in the number of lakes can be found in the surface area distribution of the predicted lakes (Fig. 20). The majority of the predicted lakes has surfaces of $25\,km^2$, corresponding to an idealized circular lake diameter of 5.6 km. Buried beneath ice thicknesses of up to 4 km, such small lakes have no impact on the appearance of the ice surface. The ice column above these lakes is mainly supported by the lateral ice sheet and not in floating equilibrium (e.g., Wright and Siegert, 2011). Accordingly, no surface flattening occurs at the ice sheet surface above such small lakes, which in contrast is characteristic above lakes with the size of several times the ice thickness (e.g., Bell et al., 2007; Smith et al., 2009). The inventory of Antarctic subglacial lakes by Wright and Siegert (2012) mostly includes lakes which were identified by ice sheet surface features observed by satellite laser altimetry (Sec. 3.1.2). Consequently, the current inventory might be lacking a large amount of these so far undiscovered smaller lakes. This hypothesis will be investigated in the next section, where the existence of uncharted predicted lakes is verified on the basis of AWI RES profiles.

4.4   RADAR-BASED VALIDATION OF PREDICTED LAKES

In this section, the specific analysis of RES profiles at the locations of predicted lakes is used as a tool to estimate the predictive value of the applied method regarding the prediction of so far uncharted subglacial lakes.

4.4.1 *Matching with flight lines and analysis*

Numerous RES flight campaigns of the AWI surveyed large parts of the Antarctic Ice Sheet during the summer seasons of the Southern Hemisphere in the last decade. In this study, all RES flight lines[1] between 1994 and 2013 (there were no campaigns in 1999/2000, 2006/07 and 2009/10) are taken into consideration for a comparison with the locations of the 10 183 predicted subglacial lakes. Some of the RES records of the 2012/13 seasons are not readily processed to this date and could not be taken into account for that reason. At 804 locations a flight line is found to cross the outlines of a predicted lake. Restricting the search results to areas where the radar penetrated the ice sheet and reached the bedrock, 270 flight lines crossing 263 predicted subglacial lakes are obtained. For these flight lines images of the associated radar profiles are processed for the segment matching the extent of the predicted lake whereby this segment is expanded by 5 km at both sides. In a visual analysis of all 270 images the radar reflections at the ice sheet base are checked for lake surface signatures. Lakes at the ice base have a very characteristic appearance in radar profiles. The different dielectric properties of ice and water cause a much stronger reflection at ice-water interfaces than at ice-bedrock interfaces. Additionally, subglacial lake surfaces appear strikingly flat in contrast to the surrounding mostly undulated bedrock. In summary, it can be stated that surfaces of subglacial lakes produce extended flat and bright basal radar reflection, which the respective radar profiles are analyzed for. A thorough description of the identification of lakes at the base of ice sheets on the basis of RES records is given in Sec. 3.1.2.

4.4.2 *Results and interpretation*

The interpretation of 270 radar profiles at the locations of 263 predicted subglacial lakes yields the identification of potential subglacial lake surfaces in 40 flight lines crossing 33 predicted subglacial lakes (Fig. 23). Three of these flight lines cross known subglacial lakes: two Lake Vostok and one the Adventure Trench Lake (red triangles). As expected, the associated radar profiles show clearly recognizable lake surface reflections. The radar profiles of the remaining 36 flight lines show potential basal lake surfaces at the locations of 31 predicted and so far uncharted subglacial lakes (blue triangles). In 230 of the analyzed radar profiles no typical basal water reflections are found (gray triangles).

Figure 24 shows three selected radar profiles in DML of locations where so far uncharted lakes are predicted. The radar profiles show the surface and the internal stratigraphy of the ice sheet as well as the bedrock beneath the ice sheet. The extents of the predicted lakes are indicated and show a very good correlation with the extents of the hollows in the bedrock topography. For these

---

1 Geographical positions of flight lines and associated radar profiles provided by Daniel Steinhage (AWI)
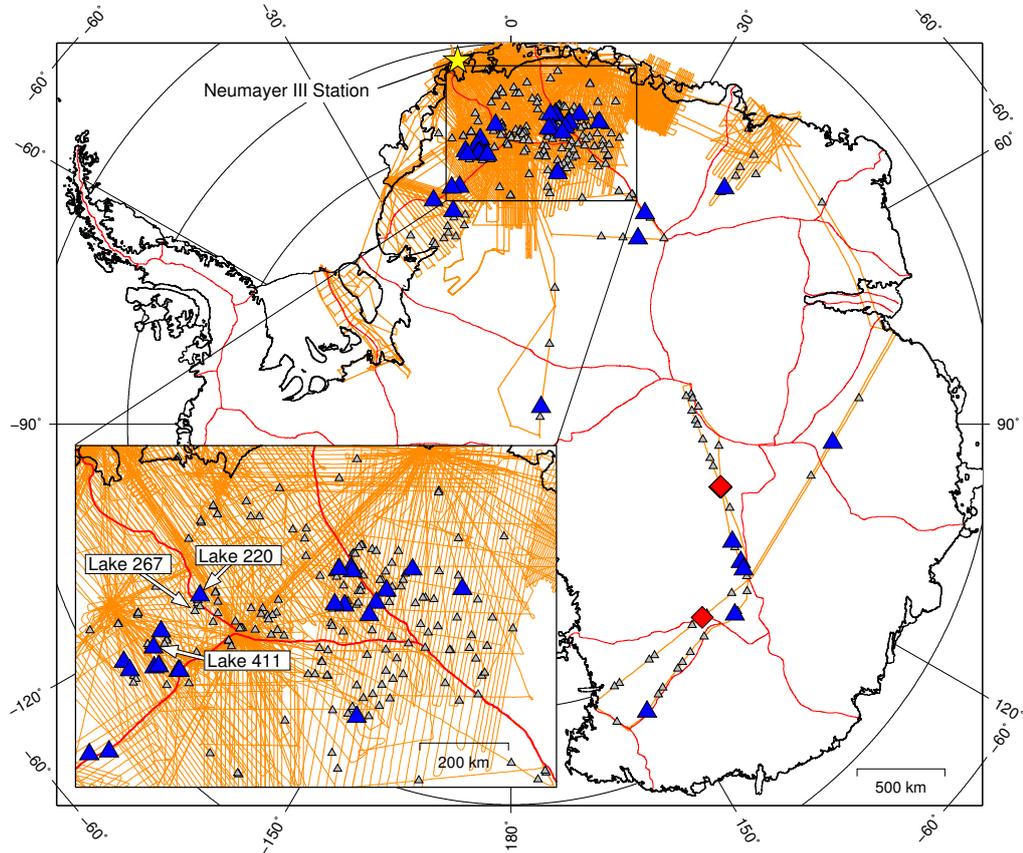
Figure 23: All AWI RES flight lines (orange) in Antarctica from 1994 to 2013 with locations marked by triangles where flight lines cross the outline of a predicted subglacial lake. Red diamonds indicate predicted and already known subglacial lakes (Lake Vostok and Adventure Trench Lake) ascertained by a cleary visible lake surface reflection in the associated radar profile. Gray triangles stand for predicted and so far uncharted subglacial lakes where no lake-surface could be detected in the radar profiles. Predicted and so far uncharted subglacial lakes where a potential lake surface reflection is found in the radar profile are pointed out by blue triangles. For three selected predicted lakes the radar profile is shown in Fig. 24. Coast and grounding line (black) by NSIDC and ice divides (red) by AGAP.

(a) Flight line 032003, predicted lake 220

(b) Flight line 982406, predicted lake 411

(c) Flight line 032006, predicted lake 267
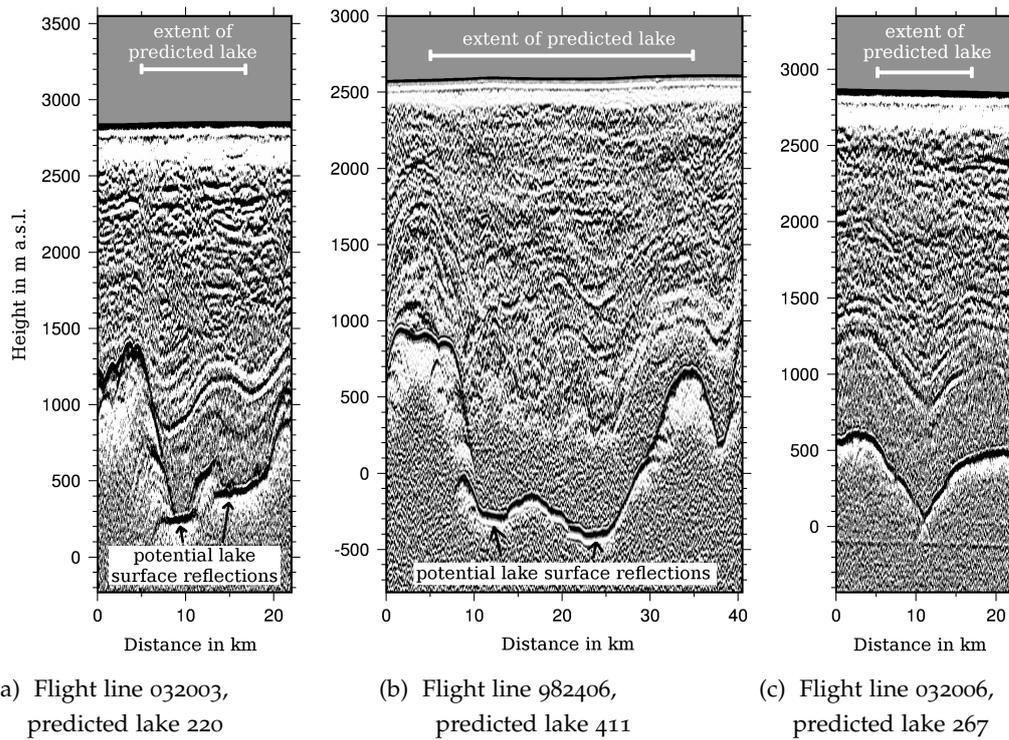
Figure 24: Selected radar profiles of AWI RES flight lines crossing predicted and so far uncharted subglacial lakes (Fig. 23). All three profiles show a hollow in the bedrock topography in good agreement with the predicted maximum possible lake extent. Profile (a) and (b) show strong and flat lake-like radar reflections at the bottom of the bedrock troughs. The basal reflections in profile (c) show no indications for the existence of accumulated basal water.

selected profiles, the hydraulic potential is mainly governed by the bedrock topography because the ice sheet surface is flat compared to the variations of the bedrock elevations. Assuming the bedrock hollows filled by water to their maximum level, exactly the predicted lake extents are identified. Although the predictions are based on data sets where bedrock and ice sheet geometry were interpolated onto grids with spatial resolutions of 5 km, the predictions and observations show a remarkably precise congruence. This approves the validity of the applied algorithm to identify and fill hollows in the hydraulic potential.

The radar profiles in Fig. 24a and 24b additionally show bright and flat reflections at the bottom of the bedrock hollows. These reflectors are interpreted as the surfaces of subglacial lakes which have lengths between 3 and 5 km. Their existence reveals that the ice sheet locally is at its pressure melting point and produces melt water. However, the observed bedrock trough is not filled to its maximum level. This might have two different reasons: The identified lakes might have a narrow outlet in the direction orthogonal to the orientation of the flight line which is not incorporated in the topography data set due to the density of locally available measured data and the applied interpolation method (Fretwell et al., 2013). They also might be active subglacial lakes which recently drained and therefore are not filled to their possible maximum extent (Smith et al., 2009).

In Fig. 24c the basal radar reflections around the bedrock trough show no evidence for the occurence of accumulated water despite the prediction of a subglacial lake at this position. A possible explanation could be again an existing outlet in the direction orthogonal to the orientation of the flight line which is not incorporated in the used gridded data set. Available melt water would then not be able to accumulate but would flow further downstream the hydraulic potential. Another possibility for the observed absence of a predicted lake despite the existence of an appropriate hydraulic hollow could be found in the local thermal regime of the ice sheet. Possibly, the ice sheet base is not at its pressure melting point at this location. In this particular case, the ice would be frozen to the bedrock and no melt water would be produced. Consequently, even hydraulic hollows would stay dry.

4.4.3   *Conclusion and estimates*

Out of 263 predicted lakes which are crossed by AWI flight lines, 33 lakes could be identified by analyzing the associated RES profiles. Beside two already known subglacial lakes 31 new subglacial lakes are found. In general, the interpretation of radar profiles does not always provide unambiguous results and in some cases additional investigations (e.g., seismic explorations) might be necessary to achieve clarity. Therefore, the uncertainty with respect to the number of identified subglacial lakes is estimated to eight. In this way, a corresponding prediction success rate of $13\pm3\,\%$ is obtained. This rate is

gained almost exclusively by the evaluation of AWI RES flights covering DML, the region southeast of the Neumayer III Station. (Fig. 23). Despite the very good coverage by remote sensing campaigns, only a very few subglacial lakes have been found in this region so far (Fig. 21, Wright and Siegert, 2012). According to model results from Pattyn (2010), the ice sheet base for some parts of DML could not be at its pressure melting point. As a consequence, locally no melt water would be available to form subglacial lakes. This study is based on the simplified assumption that the Antarctic Ice Sheet is wholly warm-based which might lead to an over-prediction of subglacial lakes in this particular region. For this reason, the prediction success rate of 13$\pm$3 % should be considered as a lower boundary for estimates concerning the entire Antarctic Ice Sheet. Furthermore, the predictive power might be increased in future studies by combining the applied approach with other methods regarding the automated analysis of bedrock roughness (Steinhage et al., in prep.) and basal radar reflection strength along flight lines (Kasper et al., in prep.).

Ensuing from the results of the radar-based validation of predicted subglacial lakes in DML, the overall number and surface area of Antarctic subglacial lakes can be estimated. In total, 10 183 subglacial lakes with an overall surface of 590 900 km^2 are predicted. Corresponding to the obtained prediction success rate of 13$\pm$3 %, 1 300$\pm$300 subglacial lakes are estimated to exist beneath the grounded Antarctic Ice Sheet. Compared to the current inventory (Wright and Siegert, 2012) which lists 379 subglacial lakes, there are still 921$\pm$300 lakes to be discovered, indicating that only about 30 % of all existing lakes are known so far. Due to the explanations above, the applied success rate and, by implication, the obtained number of undiscovered lakes should be considered as a lower boundary of the estimate. Applying the obtained prediction success rate on the overall predicted subglacial lake surface, the area of approximately 77 000$\pm$18 000 km^2 (0.64$\pm$0.15 %) beneath the Antarctic Ice Sheet is estimated to be covered by subglacial lakes. Wright and Siegert (2011) assessed the total surface of known subglacial lakes to be approx. 50 000 km^2 using the circular approx. for lakes crossed by just a single survey line. This means that about 65 % of the subglacial lake surfaces are already charted while only about 30 % of the estimated number of subglacial lakes is known so far. Consequently, the majority of the undiscovered subglacial lakes is estimated to be comparatively small with an average surface extent of approx. 29 km^2. This finding is very reasonable since all larger subglacial lakes can be supposed to be already discovered by satellite altimetry.

4.5 SIMULATION OF BASAL MELT WATER PATHWAYS

The melt water flow pattern beneath the Antarctic Ice Sheet is computed in order to gain a better understanding of the structure of the basal hydraulic network, particularly subglacial lake drainage pathways and spatial correlations between basal hydrology and ice stream locations.

4.5.1   *Motivation and method*

A wide-spread hydraulic network beneath the Antarctic Ice Sheet transports basal melt water over thousands of kilometers from the center of the continent to the grounding lines (e.g., Wright et al., 2012). On its way from the interior of the ice sheet to the ocean this water typically feeds and drains several subglacial lakes (e.g., Wingham et al., 2006b; Carter et al., 2009b; Fricker et al., 2010). The knowledge of the spatial configuration of this subglacial drainage system reveals information about how and which subglacial lakes are connected (e.g., Siegert et al., 2009) and where particular subglacial lakes drain at the Antarctic coast line (e.g., Wright et al., 2008). Additionally, spatial patterns of basal water flow can be used to explain the positions of ice streams. Depending on the flow regime (Sec. 3.2) the presence of basal water can lower the basal friction at the ice base and, thus, lead to increased ice flow.

In the following, the potential pathways of melt water beneath the Antarctic Ice Sheet are calculated with the ice model RIMBAY. First, the ice sheet geometry of the Bedmap2 data set (Fretwell et al., 2013) is used to calculate the hydraulic potential at a model resolution of 10 km, according to Sec. 4.1. Second, the scalar balance flux of basal melt water is computed following Budd and Warner (1996), where the hydraulic potential was modified in order to guarantee flux conservation (Sec. 3.3.3). The uncertainties related to the knowledge, respectively modeling, of the local basal melt rates are avoided by prescribing a constant basal melt rate for the entire grounded ice sheet. In this manner, the computed scalar balance water flux can be converted into flux values which locally express the percentage of the entire grounded ice sheet being drained.

This method provides an update to the work presented by other authors who modeled basal water pathways for Antarctica: Pattyn (2010) computed the balance flux as above but used the older Bedmap data set (Lythe et al., 2001). Wright et al. (2008) (using Bedmap) and Livingstone et al. (2013) (using Bedmap2) applied a routing algorithm from the ArcHydro package (part of the GIS software ArcMap). This algorithm directs the water flow at every grid cell entirely into the direction of the largest hydraulic gradient which is particularly unrealistic when both gradients are of a similar order. The balance flux scheme is more diffusive in such cases and thus better capable to describe natural water flow.

4.5.2   *Patterns of basal water flow*

Figure 25 shows the modeled subglacial melt water flow for Antarctica. At large scales the basal water flow follows the general surface gradient of the Antarctic Ice Sheet from the ice divides to the grounding lines. Several distinct catchment areas are revealed by the flow patterns. They are separated by watersheds which are largely congruent with the ice divides.
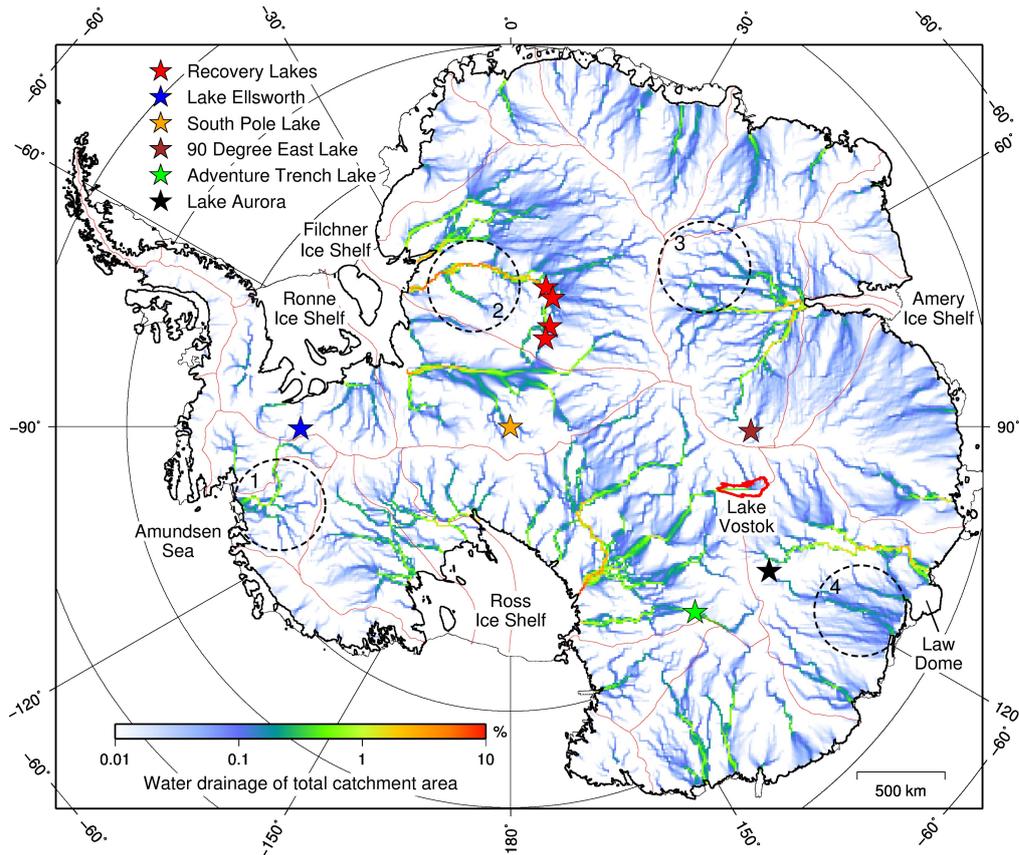
Figure 25: Simulated basal melt water pathways for the Antarctic Ice Sheet (topography by Bedmap2, Fretwell et al., 2013). The color scale shows the water drainage in percent of the total catchment area. Dashed circles mark exemplary regions with (1) angular, (2) distributary, (3) dendritic and (4) parallel drainage patterns. Particular drainage pathways can be tracked for a selected number of subglacial lakes (stars). Coast and grounding line (black) by NSIDC, ice divides (red) by AGAP.

The patterns of simulated basal water flow are not uniform but show variations between different Antarctic regions because they are determined by slope and structure of the hydraulic potential. Twidale (2004) (who investigated patterns of surface rivers) distinguishes between parallel, radial and distributary flow patterns which are mainly induced by slope and straight, angular, trellis and annular arrangements produced by structure. Four of these patterns are identified to dominate the simulated subglacial water flow in Antarctica (exemplary regions are marked by circles in Fig. 25):

1. *Angular* drainage patterns are mostly found in West Antarctica and caused by strong variations of the bedrock elevation, originating from the local geology.

2. *Distributary* flow patterns defined as the convergence of distinctly delimited distributaries are found, e.g., in the area around the tributaries of the Recovery Ice Stream. They reflect the basal topographic focusing of basal melt water flow by bedrock troughs which attract all surrounding available water due to their low hydraulic potential.

3. Close to the ice divides in the interior of the ice sheet classical *dendritic* flow patterns dominate the drainage. There, the prevalent low surface gradients allow the melt water to flow mainly under the influence of the bedrock topography and build up arborescent networks.

4. At the ice sheet margins the direction of basal melt water flow is primarily controlled by the high surface gradients and therefore *parallel* drainage patterns predominate.

The general pattern of the simulated melt water pathways is in good agreement with previous results of other authors. Compared to Pattyn (2010) who used the older Bedmap data set (Lythe et al., 2001), the drainage system is shown in much more detail. Due to the higher amount of available data points in the used Bedmap2 data set (Fretwell et al., 2013) especially the dendritic drainage patterns illustrate also smallest water tributaries. Wright et al. (2008) and Livingstone et al. (2013) chose another approach and are capable to identify single flow lines. However, they can not reveal the variability in the diffusivity of water flow. That is the strength of the used balance flux concept. It also yields distinct flow lines where the hydraulic potential is well structured. In contrast, it shows a more diffusive flow where the hydraulic potential is featureless and flat. Thus, no precision regarding to the obtained flow patterns is pretended which is not given in regions of flat or bad surveyed (and large-scale interpolated) bedrock topography.

4.5.3   *Drainage pathways of subglacial lakes*

The simulated pattern of melt water flow beneath the Antarctic Ice Sheet gives evidence which subglacial lakes are connected by basal water flow and which

lakes are hydrologically separated from each other. Additionally, it can be stated where every particular subglacial lake drains into the Antarctic Ocean. Below, these considerations are performed exclusively for a selection of prominent lakes: the Recovery Lakes, Lake Ellsworth, South Pole Lake, 90 Degree East Lake, Adventure Trench Lake, Lake Aurora and Lake Vostok (Fig. 25).

The Recovery Lakes are four large smooth basins situated at the onset of the Recovery Ice Stream (Bell et al., 2007). Similar to results derived from radar observations (Langley et al., 2011), the simulated water flow pattern shows that these lakes are connected and drain through a joint outlet underneath the Filchner Ice Shelf.

Lake Ellsworth is located slightly east of an ice divide in the Ellsworth Mountains in West Antarctica but west of the shifted corresponding watershed. Therefore, it is found to drain into the Amundsen Sea ($\approx$560 km) and not underneath the much closer Ronne Ice Shelf ($\approx$160 km) similar to estimates from Vaughan et al. (2007).

The South Pole Lake is clearly identified to drain underneath the Filchner-Ronne Ice Shelf and the 90 Degree East Lake to drain underneath the onset of the Amery Ice Shelf. Water draining Lake Aurora could be identified to flow comparatively straight towards the coast line east of the Law Dome (Wright et al., 2012).

The largest subglacial lake, Lake Vostok, as well as the Adventure Trench Lake are confirmed to drain on different pathways through the mountain range of the Transantarctic Mountains underneath the Ross Ice Shelf (e.g., Wright et al., 2008; Livingstone et al., 2013). Following Wright et al. (2008) the drainage pathway of the Adventure Trench Lake is highly sensitive to small changes of the ice sheet. The authors stated that a change of ice sheet surface elevation in the order of meters can redirect the drainage pathway on a continental scale. This result is also demonstrated in Fig. 25 which shows the Adventure Trench Lake to be situated very close to a watershed. A minor future change of the local ice sheet geometry has the potential to redirect the lake's outflow towards the hydrological tributaries of the David Glacier (Fig. 26) and thus possibly cause a speed-up of its velocity.

4.5.4   *Locations of ice streams and enhanced basal water flow*

Considering observed ice surface velocities of the Antarctic Ice Sheet (Rignot et al., 2011a) many areas of significantly increased ice flow can be identified (Fig. 26a). These ice streams and fast flowing glaciers reach velocities of several hundred meters per year and are feeding into adjacent ice shelves or the ocean. Their precise locations are determined by several controls, as for instance, subglacial melt water routing (Winsborrow et al., 2010). Particularly, distributed basal water flow regimes are capable to decrease friction at the ice-bed interface and thus lead to enhanced ice sliding velocities (Sec. 3.2). The computed basal water pathways in Fig. 26b follow the gradients of the basal hydraulic
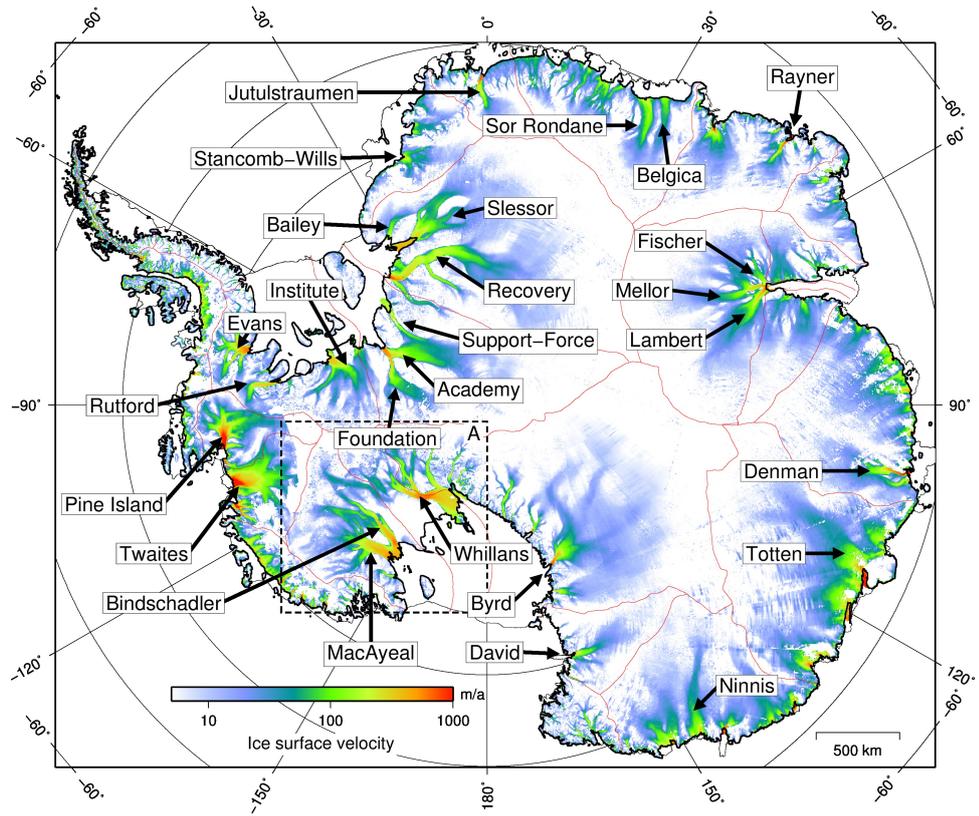
(a) Ice surface velocities for grounded ice (Rignot et al., 2011a)
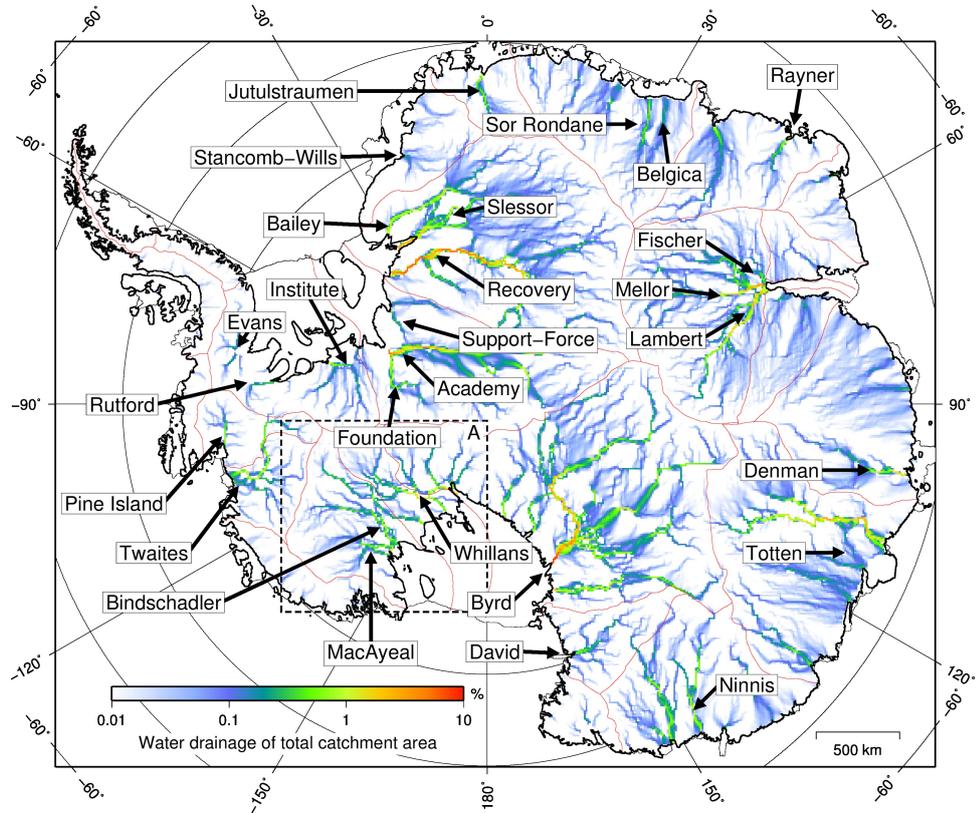
(b) Simulated basal melt water pathways

Figure 26: The locations of Antarctic ice streams and fast flowing glaciers showing a very good correlation with areas of enhanced and focused subglacial melt water flow. The dashed rectangle (A) marks the hydrologically enclosed study area of the following chapter. Coast and grounding line (black) by NSIDC, ice divides (red) by AGAP

Lake predicted	Lake in inventory	Lake outline crossed by flight line	Lake identified in radar profile	Count	Symbol	Figure
✓				10 183	(blue lake)	19, 22
	✓			379	△+▲	21, 22
✓	✓			206	▲	21, 22
✓	✓	✓		2	◆	23
✓	✓	✓	✓	2	◆	23
✓		✓		263	△+▲	23
✓		✓	✓	31	▲	23

Table 2: Summary of the results for the prediction of subglacial lakes and their inventory- and radar-based validation including the associated symbols and figures where they appear.

potential. It is calculated under the assumption that the effective basal water pressure is zero and is therefore valid for distributed water flow.

A comparison of the patterns of ice velocity and basal water drainage in Fig. 26 reveals a high correlation between fast ice flow and areas of enhanced and focused water flow. The locations and extents of all large ice streams and fast flowing glaciers can be successfully traced back to congruent basal drainage patterns. Even details like the southern tributary of the Recovery Ice Stream and the three tributaries of the Slessor Glacier are depicted in both the velocity field and in the drainage structure.

Additionally, it is found that the basal water flow originating from 22.5 % of the subglacial Antarctic hydraulic catchment area is draining into the ocean at only four spots: the mouth of the Byrd Glacier (8.1 %) at the Ross Ice Shelf and the mouthes of the Recovery Ice Stream (6.5 %), the Slessor Glacier (3.0 %) and the confluent Academy Glacier and Foundation Ice Stream (4.9 %) at the Filchner-Ronne Ice Shelf. Depending on the basal melt rates in the respective upstream areas, this spatially concentrated fresh water entry into ice shelf cavities could be huge and considerably affect ocean currents (e.g., Hellmer et al., 2012).

The dashed rectangle in Fig. 26b delimits a hydrologically enclosed region around the Siple Coast. The observed temporal variability of ice streams makes it the perfect study area for the further investigation of the interplay between ice dynamics and basal water flow in the next chapter.

4.6 SUMMARY

Based on the calculated basal hydraulic potential for the Antarctic Ice Sheet the locations and extents of 10 183 potential subglacial lakes covering 4.9 % of the

ice sheet base are predicted (Tab. 2). The validity of this method is approved by the successful theoretical prediction of 206 observed subglacial lakes in the current inventory (379 lakes, Wright and Siegert, 2012). A comparison of AWI RES flight lines and predicted lake outlines yields 263 matches, where in 33 of these radar profiles basal water reflections are identified. Two of them are associated with already known subglacial lake surfaces and 31 reveal the locations of so far uncharted subglacial lakes. Based on the obtained prediction success rate, the total number of Antarctic subglacial lakes can be estimated to $1\,300\pm300$. The estimated surface area of these lakes adds up to $77\,000\pm18\,000\,\text{km}^2$, corresponding to approx. $0.6\,\%$ of the ice-bed interface. Respective to assessments of the current inventory (Wright and Siegert, 2011) it can be stated that $30\,\%$ of all Antarctic subglacial lakes and $65\,\%$ of the total estimated lake-covered area are discovered at present. The simulation of Antarctic basal melt water flow unveils complex subglacial drainage patterns. It is found that melt water contributions from about $23\,\%$ of the basal water catchment area are draining into the ocean at only four particular spots. Connections and drainage pathways of selected subglacial lakes are discussed and the striking spatial correlation of simulated enhanced basal water flow and observed ice streams are demonstrated.

INTERACTIONS OF SUBGLACIAL HYDROLOGY AND ICE DYNAMICS AT THE SIPLE COAST, ANTARCTICA

This chapter focuses on the West Antarctic Ice Sheet (WAIS) and the local interactions of subglacial hydrology and ice dynamics. The spatial and temporal variability of the Ross Ice Streams at the Siple Coast is investigated and possible controls on their locations are discussed. The mass balance of this area is determined, using results from two different satellite altimetry campaigns: ICESat and CryoSat-2. The observed patterns of ice surface elevation change are interpreted and the influence of subglacial water routing on the ice dynamics is estimated. After that, present-day pathways and catchment areas of water flow beneath the Ross Ice Streams are simulated and compared to observed patterns of fast ice flow. The evolution of the basal drainage system is simulated by applying the satellite-observed ice surface changes to the present-day ice sheet topography. Finally, the results are discussed, regarding their implications for the future evolution of the Ross Ice Streams.

5.1 STUDY AREA AND MOTIVATION

The ice volume of the WAIS is estimated to 2.2 million km^3 (Lythe et al., 2001), hence it contains about 10 % of the Antarctic ice. The approximately 97 % ice-covered WAIS (Fretwell et al., 2013) is mainly marine based, meaning that the majority of the bedrock lies below sea level. Therefore, the WAIS is assumed to be potentially unstable under future climate warming where a partial collapse could contribute to global eustatic sea level rise by 3.3 m (Bamber et al., 2009). Consequently, the understanding of the hydrology and ice dynamics concerning future developments is essential.

For the investigation of the WAIS system a domain is chosen which encompasses parts of Marie Byrd Land and the Siple Coast (see rectangle A in Fig. 27). The study area is enclosed by ice divides in the north and in the east (please note the orientation of the map where south is in the upper right corner). These ice divides also perform as subglacial watersheds, whereby the area of interest can be considered as hydrologically enclosed at these margins (Fig. 26b, Chap. 4). Beyond the Transantarctic Mountains a small part of the East Antarctic Ice Sheet (EAIS) is included, because it belongs to the basal hydrological catchment area of the Siple Coast. In the west, the area of investigation is bounded by the Ross Ice Shelf.
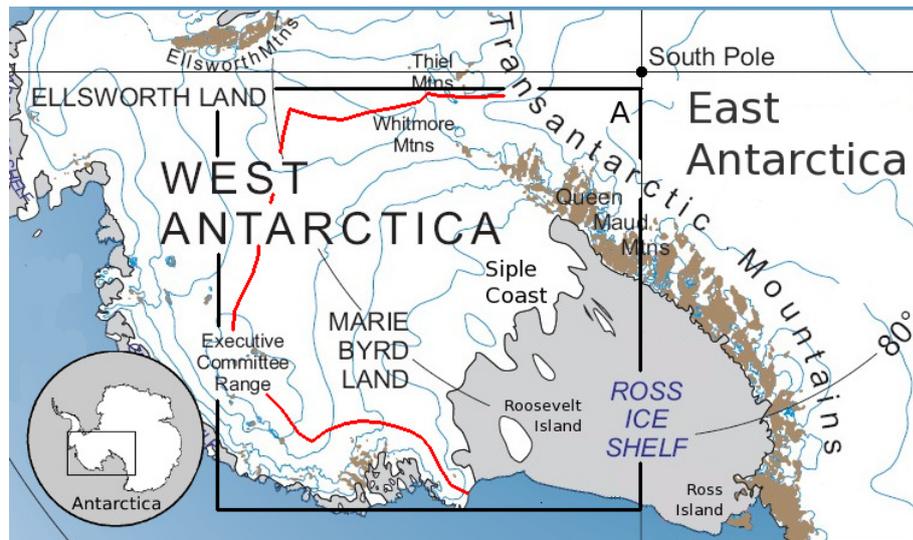
Figure 27: West Antarctica with Marie Byrd Land, Siple Coast and Ross Ice Shelf. The study area is defined by rectangle A and relevant ice divides (AGAP) are marked in red (Fig. after British Antarctic Survey, 2007).

5.2   THE ROSS ICE STREAMS

The Ross Ice Streams, being responsible for the vast majority of the ice transport from the interior of the WAIS towards the Ross Ice Shelf, are introduced in this section. Their variability in the past and local controls on their locations are discussed as well as observations and estimates of the hydraulic system underneath.

5.2.1   *Present-day configuration and variability in the past*

The ice dynamics at the Siple Coast (subdivided into Gould Coast, Siple Coast and Shirase Coast) are clearly dominated by several major ice streams, also called the Ross Ice Streams. Initially, they were refered to as Ice Stream A to F but meanwhile all of them were named. Figure 28 shows their outlines and ice catchment areas plus the ice ridges in between. The southernmost Mercer Ice Stream (A) is separated by the Conway Ice Ridge from the confluent Van der Veen (B1) and Whillans Ice Stream (B2) at the Gould Coast. The lower part of these two converging ice streams is named for the dominant tributary of the Whillans Ice Stream and refered to as Ice Stream B in the following. The former Kamb Ice Stream (C) is located at the central Siple Coast and flanked by the Engelhardt Ice Ridge in the south and the Raymond Ice Ridge and the Siple Dome in the north. At the Shirase Coast the Bindschadler (D) and MacAyeal Ice Stream (E) are divided by the Shabtaie Ice Ridge before they unite in the Ross Ice Shelf. The northernmost Echelmeyer Ice Stream (F), isolated by the Harrison Ice Rigde, is much smaller then the other Ross Ice Streams and will be neglected in the following considerations for this reason.
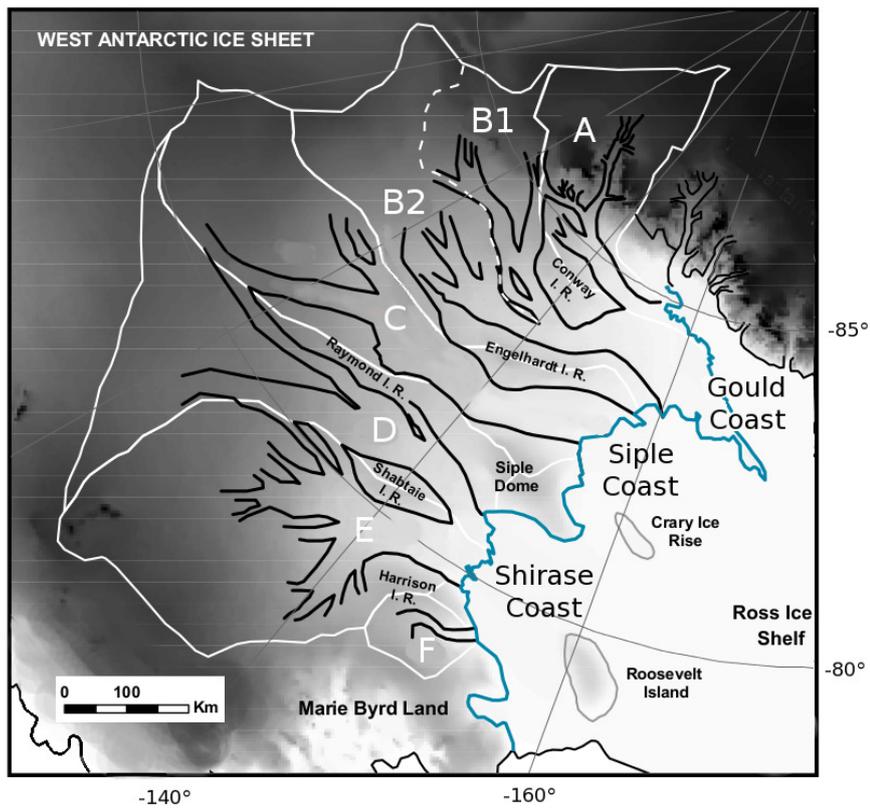
Figure 28: The Ross Ice Stream with ice drainage basins in white and ice stream outlines in black following RAMP imagery: A – Mercer, B1 – Van der Veen, B2 – Whillans, C – Kamb, D – Bindschadler, E – MacAyeal and F – Echelmeyer Ice Stream. For location of map section see Fig. 27. (Fig. after Joughin et al., 2002)

The Kamb Ice Stream, measuring 745 km from the onset of the northern-most tributary to the grounding line, began to stagnate ~150 years ago (Rose, 1979). Its former position is reconstructed from short-pulse radar profiles (Fig. 28). They show scatter from buried crevasses, which are presumed at the surface when the ice stream was still active. The thickness of the undis-turbed ice layers over these crevasses allows a back dating and reveals a se-quential stagnation. The stagnation wave had its initiation at the grounding line of the ice stream 130±25 years ago, followed by the slow-down of the middle part 100±30 years ago and finally ended at the upstream part only ~30 years ago (Retzlaff and Bentley, 1993; Anandakrishnan et al., 2001; Catania et al., 2006). Surface-based ice-penetrating radar profiles show an undulating internal stratigraphy and thus prove its former fast flow conditions with pre-stagnation flow velocities exceeding $350 \, \mathrm{m \, a^{-1}}$ in the trunk of the ice stream (Ng and Conway, 2004). With the same observation techniques evidence for a former ice stream crossing Ice Stream C to D at the northeast flank of the Siple Dome was found (Jacobel et al., 1996). But also the existing Whillans Ice Stream was detected to decelerate. Over the period 1974–97 Joughin et al. (2002) estimated a velocity loss of about 23 % with a combination of conven-tional interferometry and speckle-tracking methods applied to RADARSAT-1 data. This was confirmed by Scheuchl et al. (2012) using full Interferometric Synthetic Aperture Radar (InSAR), revealing a velocity change of $-100 \, \mathrm{m \, a^{-1}}$ (–25.3 %) for the Whillans Ice Stream and $-40 \, \mathrm{m \, a^{-1}}$ (–16,7 %) for the Mercer Ice Stream at their grounding lines between the years 1997 and 2009.

5.2.2   *Local controls on ice stream locations*

Observations reveal a high variability in the mass flux of the Ross Ice Streams as well as a significant short-term variability in ice stream shear margin and grounding line positions (Catania et al., 2012). Since the ice streams are re-sponsible for the majority of the mass export from the inner ice sheet to the grounding line their evolution plays a key role for the future mass balance of the WAIS. In order to understand or even predict their dynamic behavior, seven potential controls on ice stream locations are defined by literature (e.g., Winsborrow et al., 2010): topographic focusing, topographic steps, macro-scale bed roughness, calvin margins, subglacial geology, geothermal heat flux and subglacial melt water routing. They are likely to influence the spatial and temporal dynamics of ice streams.

Following Winsborrow et al. (2010) the primary controls most commonly associated with fast ice flow are topographic focusing, calving margins, sub-glacial geology and subglacial melt water routing which are discussed below regarding their particular influence on the Ross Ice Streams.

TOPOGRAPHIC FOCUSING   For the Ross Ice Streams the topographic focus-ing is given only for the southern tributary of the Mercer Ice Stream. It crosses

(a) Ice surface velocity and subglacial lakes   (b) Bedrock topography
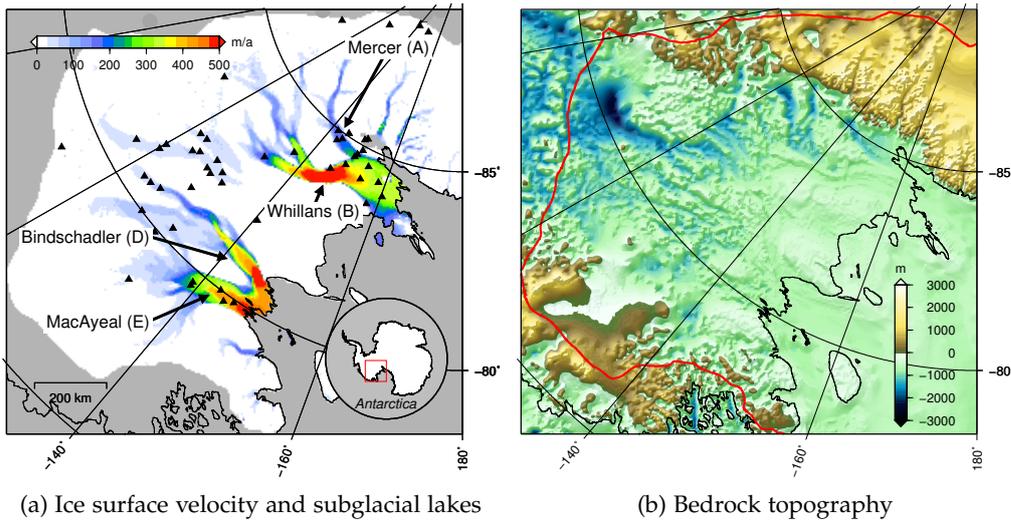
Figure 29: Siple Coast: (a) Present-day ice surface velocity (Rignot et al., 2011a) with Ross Ice Streams and positions of observed subglacial lakes (black triangles, inventory by Wright and Siegert, 2012). Velocity color scale is truncated, maximum values reach up to 709 m a^{-1} in the Whillans and 668 m a^{-1} in the Bindschadler Ice Stream. (b) Bedrock topography (Bedmap2, Fretwell et al., 2013) with ice divides (red) by AGAP and grounding line (black) by NSIDC.

the Transantarctic Mountains between Ohio and Wisconsin Range and is thus fixed at this location. All other ice streams are located at the comparatively flat submarine bedrock of the Siple Coast which does not feature any considerable trenches or canyons in correlation with the existing patterns of fast flowing ice (Fig. 29b).

CALVIN MARGINS   There is no existing calving margin associated to the ice streams in this area. The Ross Ice Shelf covers the Siple Coast in its entirety and thus uniformly buttresses the flow of ice across the grounding line (Fig. 27).

SUBGLACIAL GEOLOGY   The prime control which creates the precondition for ice streams to evolve in the area of investigation is clearly given by the subglacial geology. Numerous seismic campaigns detected a layer of till under the Ross Ice Streams (e.g, Rooney et al., 1987). Beneath the Whillans Ice Stream this unconsolidated layer of sediment was estimated to be 5–6 m thick on average and presumed to be glacial till (e.g., Alley et al., 1986). The ratio of till viscosity to effective ice viscosity is small (MacAyeal, 1989). Consequently, the vertical shear associated with horizontal flow is confined to the deforming bed alone and thus the deformation of till can be regarded as the primary mechanism by which the ice streams move (Alley et al., 1987). Borehole measurements with a *tethered stake* apparatus by Engelhardt and Kamb (1998) yielded a basal sliding in the amount of 83–100 % of the total ice motion. However, rigid bedrock substrata may contact the ice base beside the deformable till in small areas and cause vorticity in the velocity field. At these

spots the ice surface appears rumpled, visible, e.g., at Landsat images of the MacAyeal Ice Stream (MacAyeal, 1992). In seismic reflections upstream of the Kamb and Bindschadler Ice Streams Peters et al. (2006) observed sedimentary basins, which are considered to control the onsets of these ice streams. The inland termination of these sediments suggests that a possible future migration of the latter onsets is unlikely (Siegert et al., 2004). At the grounding line of the Whillans Ice Stream Alley et al. (1989) discovered a till delta tens of meters thick and tens of kilometers long. These sediments originate from upstream locations and are transported downstream by the moving ice. Beyond, this sedimentary wedge at the grounding line is believed to stabilize the position of the grounding line even despite moderate changes in sea level (Anandakrishnan et al., 2007).

SUBGLACIAL MELT WATER ROUTING   The observed existence of till gives the precondition for the development of ice streams at the Siple Coast. However, their exact locations are defined by the pathways of melt water flow. The general prevalence of basal water at the Siple Coast was confirmed by a range of radar sounding campaigns (e.g., Alley et al., 1986; Bentley et al., 1998; Jacobel et al., 2009). They found high reflection strengths at the trunk of the ice streams, interpreted as wet bed, and low reflections at the ice rises in between, interpreted as dry bed. The transitions between the areas with detected wet and dry beds show exact correlation with ice stream margins. Boreholes drilled to the ice bottom confirm that the ice base is at melting point inside the confines of the ice streams and reveal a dry bed outside (e.g., Engelhardt et al., 1990; Engelhardt, 2004). In addition, seismic investigation approved a highly porous basal till layer which is saturated by water (e.g., Blankenship et al., 1987, at the Whillans Ice Stream).

Particularly the observed spatial and temporal variability of the Ross Ice Streams can be most likely explained with the variable melt water pathways, which act on much shorter time scales than other controls, e.g., the variability of the subglacial geology or the geothermal heat flux.

5.2.3   *Subglacial lakes and melt rates beneath the ice streams*

The discovery of many subglacial lakes (Wright and Siegert, 2011) gives clear evidence for the presence of basal water. Furthermore, satellite laser altimeter elevation profiles show patterns of varying ice surface elevation which are interpreted as the surface expression of subglacial water movement through a system of channels between linked lakes (e.g., Fricker et al., 2007; Fricker and Scambos, 2009). A striking feature of these active lakes is their clustering within the confines of ice streams (Smith et al., 2009) (Fig. 29a), such as the subglacial Lake Whillans beneath the Whillans Ice Stream (Horgan et al., 2012; Christianson et al., 2012). For example, in a tributary of the Kamb Ice Stream an area of $\sim$125 km^2 slumped vertically downwards by up to 0.5 m between

September 26 and October 18, 1997 (Gray et al., 2005). Such single lake discharge events can cause temporal subglacial water fluxes from 20 to 300 m^3 s^{-1} (Gray et al., 2005; Fricker et al., 2007; Fricker and Scambos, 2009; Carter and Fricker, 2012). Although these observations reveal a widespread, dynamic subglacial water system that may exert an important control on ice flow and mass balance, the precise local melt rates are barely known since they elude direct measurements. Analytical model results, e.g., for the Whillans Ice Stream, indicate melt rates between 3–7 mm a^{-1} for the upstream and 20–50 mm a^{-1} for the downstream domain (Beem et al., 2010). With another modeling approach Joughin et al. (2003) found, that most melting occurs beneath the tributaries where larger basal shear stresses and thicker ice favor higher melt rates in the order of 10–20 mm a^{-1}. The ice stream tributaries and the inland ice are accounted for about 87 % of the total melting generated beneath the Ross Ice Streams including their catchments (Joughin et al., 2004). Following Parizek et al. (2003) this melt water transports latent heat from beneath inland ice to the base of the ice streams. The temperature at the bottom of the ice streams itself and accordingly the melt rates are low, caused by the scarce internal ice deformation and the consequently lacking internal frictional heating. This was confirmed by temperature measurements in boreholes at the Whillans Ice Stream and is consistent with observations of its deceleration over the last decades which might lead to a possible shutdown in the future (Joughin et al., 2004).

5.3   ICE SURFACE ELEVATION CHANGE OBSERVED BY SATELLITE ALTIMETRY

In this section, ice surface elevation change rates gained by two different satellite campaigns are used to estimate the mass balance at the Siple Coast. Observed patterns of elevation change are compared and discussed, regarding particularly the impact of basal hydrology on the ice dynamics.

5.3.1   *Origin and processing of ICESat and CryoSat-2 data*

Satellite altimetry data originating from the ICESat and CryoSat-2 mission are used. Here, a short introduction of the two satellite campaigns and the onboard instruments is given:

ICESAT   The Ice, Cloud and Land Elevation Satellite (ICESat, Zwally et al., 2002) mission from 2003 to 2009 was part of the National Aeronautics and Space Administration (NASA) Earth Observing System. The onboard Geoscience Laser Altimeter System (GLAS) measured cloud and aerosol heights, land topography, vegetation characteristics and ice sheet mass balance. The satellite provided multi-year elevation data needed to determine ice sheet mass balance as well as cloud property information. In addition to the polar-specific cover-

age of the Antarctic and Greenland Ice Sheets and the Arctic up to latitudes of 86° north and south, it provided topography and vegetation data around the globe.

CRYOSAT-2   The satellite CryoSat-2 (description only published for the similar CryoSat-1, which crashed shortly after its launch, by Wingham et al., 2006a) was launched by the European Space Agency (ESA) in 2010. It carries a radar altimeter which is able to operate in Synthetic Aperture Radar (SAR) and Interferometric mode and is therefore called Synthetic Aperture Radar Interferometric Radar Altimeter (SIRAL). CryoSat-2 is orbiting the earth at a higher inclination than ICESat, reaching latitudes of 88° north and south. Its radar altimeter SIRAL was particularly designed for accurate measurements of icy surfaces and is capable of detecting annual thickness variations of sea ice and small elevation changes of ice sheet surfaces.

In the ICESat mission the rate of surface height change was measured by using a time series of repeat-track satellite laser altimeter from 2003 to 2008 (Pritchard et al., 2009, 2012). In the processing of the data[1] for the Siple Coast region, all values exceeding 0.8 m of absolute elevation change are regarded as discordant values and ignored. The remaining data points are bilinear interpolated onto a 10 km grid and smoothed out with a Gaussian filter of 60 km width. The CyroSat-2 surface elevation change rates are gained by the comparison of surface elevation measurements in 2011 and the 2012 (Helm et al., 2014), where a cross point analysis yields about one million data points for the Siple Coast region. To transfer the data onto a 10 km grid a blockmedian filter with a radius of 15 km is applied. Thereafter, all values exceeding 0.8 m of absolute elevation change are ignored and remaining data values are smoothed out with a Gaussian filter of 60 km width, similar to the ICESat data processing.

5.3.2 *Mass balance derived from surface elevation change rates*

The surface elevation change rates derived from both ICESat and CryoSat-2 measurements are shown in Fig. 30. The depicted values comprise all effects on the local mass balance: snow accumulation, surface snow drift by wind, ice thickness changes by horizontal ice in- and out-flow as well as basal melting and refreezing. Summing up the rates of surface height change for all grounded ice nodes, a slightly positive mass balance is found for both campaigns. According to the ICESat observations with a given uncertainty of $\pm 0.07\,\mathrm{m\,a^{-1}}$ for the surface change rates (Pritchard et al., 2009), the grounded ice volume is rising by $50 \pm 63\,\mathrm{km^3\,a^{-1}}$ (0.0036 %). For an assumed average ice density of $\rho_i = 910\,\mathrm{kg\,m^{-3}}$ the latter volume change corresponds to a growth of $46 \pm 57\,\mathrm{Gt\,a^{-1}}$ (gigatons per year) . The CryoSat-2 observations reveal a 28 %

---

1 ICESat surface elevation change rates provided by Hamish Pritchard (BAS), personal communication.
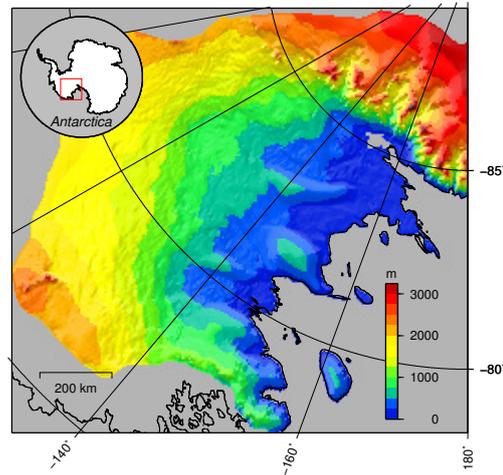
(a) Ice sheet surface elevation
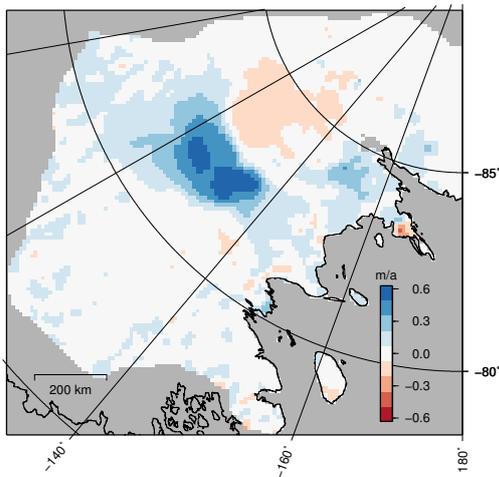
(b) ICESat – Ice surface change
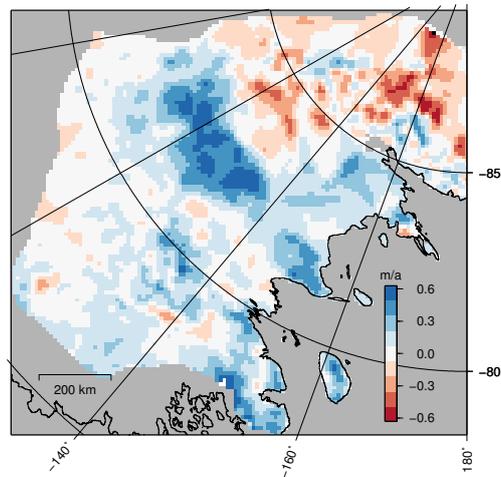
(c) CryoSat-2 – Ice surface change

Figure 30: Siple Coast: (a) Ice sheet surface elevation (Fretwell et al., 2013) and ice surface elevation change rates (dS/dt) derived from (b) ICESat (Pritchard et al., 2012) and (c) CryoSat-2 measurements (Helm et al., 2014). Bounding ice divides by AGAP and grounding line (black) by NSIDC.

larger volume increase of $64\pm63\,\mathrm{km^3\,a^{-1}}$ (0.0046 %) for grounded ice, corresponding to $58\pm57\,\mathrm{Gt\,a^{-1}}$ mass accretion. Here, an uncertainty similar to the ICESat measurements was assumed, because the estimation of the uncertainty for the CryoSat-2 measurements is still in progress (Helm et al., 2014). Calculating the mean for the above satellite campaigns a mass grows of $52\pm57\,\mathrm{Gt\,a^{-1}}$ is indicated. Joughin and Tulaczyk (2002) used ice-flow velocity measurements from synthetic aperture radar to reassess the mass balance of the Ross Ice Streams. They also found strong evidence for ice sheet growth ($26.8\pm14.9\,\mathrm{Gt\,a^{-1}}$), in contrast to earlier estimates by Shabtaie and Bentley (1987) which indicated a mass deficit ($-20.9\,\mathrm{Gt\,a^{-1}}$). Although the measured mass balance at the Siple Coast by ICESat, CryoSat-2 and Joughin and Tulaczyk (2002) shows variations and the given uncertainties are large, they all indicate a slightly growth of the ice mass.

5.3.3 *Spatial elevation changes and basal hydrology*

The average thickening corresponds to approximately 25% of the accumulation rate, with most of this growth occurring on the former Kamb Ice Stream. There, the surface elevation changes reach maximum values of $+0.65\,\mathrm{m\,a^{-1}}$, clearly visible as the central blue patch in Fig. 30 for both satellite campaigns. The stagnation of the Kamb Ice Stream approximately 150 years ago might be caused by a subglacial topographic change which redirected lubricating basal water to the adjacent Whillans Ice Stream (Anandakrishnan and Alley, 1997). That might have initiated the sequential slow down of the Kamb Ice Stream, beginning at the grounding line and proceeding upstream (Sec. 5.2.1). Consequently, the upstream tributaries (still visible in the present-day ice velocity field in Fig. 29a) feed into the now stagnant Kamb and cause the observed thickening. The resulting bulge again boosts the diversion of melt water towards the adjacent Whillans Ice Stream. Currently, it is not clarified whether the redirection of basal melt water by a subglacial topographic change caused the stagnation of the Kamb Ice Stream (Anandakrishnan and Alley, 1997) or the ice stream stagnation caused the redirection of water through the resulting thickening (Price et al., 2001; Conway et al., 2002). Surface change rates from both satellite campaigns consistently reveal a surface elevation loss at a maximum of $0.38\,\mathrm{m\,a^{-1}}$ in the area of the Whillans Ice Stream (red patch south of the blue Kamb bulge in Fig. 30). This can be interpreted as an enforced transport of ice towards the grounding line due to enhanced basal lubrication. Following Joughin and Tulaczyk (2002) the Whillans Ice Stream, which was thought to have a significantly negative mass balance, is close to balance, reflecting its continuing slowdown (Scheuchl et al., 2012). Furthermore, Joughin and Tulaczyk (2002) speculated, that the overall positive mass balance may signal an end to the Holocene retreat of these ice streams. In contrast, Conway et al. (2002) stated, that caution is needed drawing conclusions about the large-scale mass balance of the entire ice sheet when using the observation of short-term

mass changes. Catania et al. (2012) supported this statement, interpreting the stagnation of the Kamb Ice Stream as just one stage in the thermodynamic cycle of an ice stream in that region due to the interplay of the ice streams and the internal variability of the entire coupled complex system.

5.4   MODELING BASAL WATER PATHWAYS AND CATCHMENT AREAS

At the Siple Coast, the recent stagnation of the Kamb Ice Stream and the discovery of numerous relict ice-flow features indicate a steady competition between several preferred ice-flow paths of the Ross Ice Streams. Subglacial melt water routing is considered to be the main control on the ice stream locations at the Siple Coast (Sec. 5.2.2) and has the potential to explain their observed variability in the past (Sec. 5.2.1). In this section, the prevailing basal water flow regime at the Siple Coast is estimated based on in-situ observations. Present-day and prognostic pathways and catchment areas of basal melt water flow are simulated and investigated with respect to correlations with present-day ice velocity observations and implications for future locations and velocities of the Ross Ice Streams.

5.4.1   *Present-day ice sheet simulation*

Borehole measurements and seismic investigations reveal the prevalence of a meters-thick layer of unconsolidated sediments (glacial till) at the ice base of the Siple Coast. This layer is highly porous and saturated by water. The water pressure was determined to be within 0.5 to 1.5 bar (50 to 150 kPa) of the overburden ice pressure (e.g. Alley et al., 1986; Blankenship et al., 1987; Engelhardt et al., 1990; Kamb, 2001). For example, a column of 1 000 m ice (a common ice thickness at the main trunk of the Whillans Ice Stream) with an ice density of $910 \, \mathrm{kg \, m^{-3}}$ applies a gravitational pressure of 89.27 bar (8 927 kPa) to the bed. The measured difference between basal water and ice pressure of 0.5 to 1.5 bar corresponds to a deviation of only 0.6 to 1.7 % for the above example. Hence, the water pressure at these measuring sites is very close to the ice pressure and one can assume an effective pressure (ice minus water pressure) of zero. Consequently, the basal flow regime is expected to be distributed and it can be taken advantage of the balance flux concept (Sec. 3.3.3) to calculate the melt water pathways and catchment areas.

In the following model runs, the *Revised Ice Model Based on Frank Pattyn* (RIM-BAY) is forced with a constant basal melt rate for all grounded ice nodes. In this way, the influence of the whole basal water catchment area is equally represented and the fluxes can be expressed as percentage of the total catchment area. Thus, the uncertainties related to the calculation of basal melt rates beneath the Ross Ice Streams (Sec. 5.2.3) are avoided and the focus is set on the water pathways and catchment areas sizes. The flow of basal melt water is assumed to follow the basal hydraulic potential. This is calculated under the

assumption of a distributed water flow system (Sec. 3.3.1) using the bedrock elevation and ice thickness data provided by the Bedmap2 data set (Fretwell et al., 2013). The Bedmap2 data set has a resolution of 1 km for whole Antarctica, which is resampled to data sets with grid sizes of 5, 10 and 20 km for the Siple Coast region. The basal water volume flux is computed with the Budd and Warner (1996) balance flux algorithm corresponding Sec. 3.3.1 whereby flux conservation is guaranteed.

5.4.2   *Present-day subglacial hydrology*

Figure 31 shows the pathways of basal melt water for the three different model resolutions of 5, 10 and 20 km grid size. The color scale illustrates the local drainage in percent of the total catchment area. For the 5 and 10 km model resolution the outflow concentrates towards 6 embayments at the grounding line (5 embayments for the 20 km resolution). This finding is consistent with results from Carter and Fricker (2012) who investigated the variable supply of subglacial melt water to the grounding line, using a similar steady-state water model and estimates for lake volume change derived from ICESat data.

The simulated basal water pathways match very good with the areas of fast ice flow depicted in Fig. 31d. That significantly supports the assumption, that the locations of the ice streams are controlled by subglacial water routing. Furthermore, the flow patterns of the two coarser model resolutions clearly show how upstream water tributaries of the former Kamb Ice Stream (C) are partly draining into the Willans Ice Stream. The 5 km model run reveals a more finely branching flow system which also covers the trunks of all present-day ice streams. However, there are still non-neglectable melt water contributions towards the downstream part of the stagnated Kamb Ice Stream. This does not necessarily mean the model results are wrong. Airborne radio echo sounding field campaigns detected a wet bed derived from strong reflections for the main trunk of the Whillans *and* the stagnated Kamb Ice Stream (e.g., Bentley et al., 1998). The detected transitions towards dry bed areas in the inter-ice stream regions match precisely the margins of the Kamb Ice Stream, which already slowed down 150–30 years ago (Sec. 5.2.1). Within the former Kamb Ice Stream margins low radar reflectivity was limited to so-called sticky spots (small areas with high basal ice traction) and along the Kamb margins (Jacobel et al., 2009). A borehole drilled to the ice bottom at a sticky spot also found a dry bed there (Jacobel et al., 2009). That supports the hypothesis that sticky spots control the stagnation and possible reactivation of ice streams, once the basal melting passes a certain threshold (Joughin et al., 2004). Anandakrishnan and Alley (1997) assumed that the loss of lubrication on localized sticky spots at the ice bed interface can cause the shutdown or the redirection of an entire ice stream. On the other hand sticky spots, often observed to be located along the ice streams margins, act as water sources and supply the ice stream with melt water. The ice sliding at high basal traction in combination with strong

(a) Basal water pathways – 5 km grid

(b) Basal water pathways – 10 km grid

(c) Basal water pathways – 20 km grid

(d) Ice surface velocity – 5 km grid
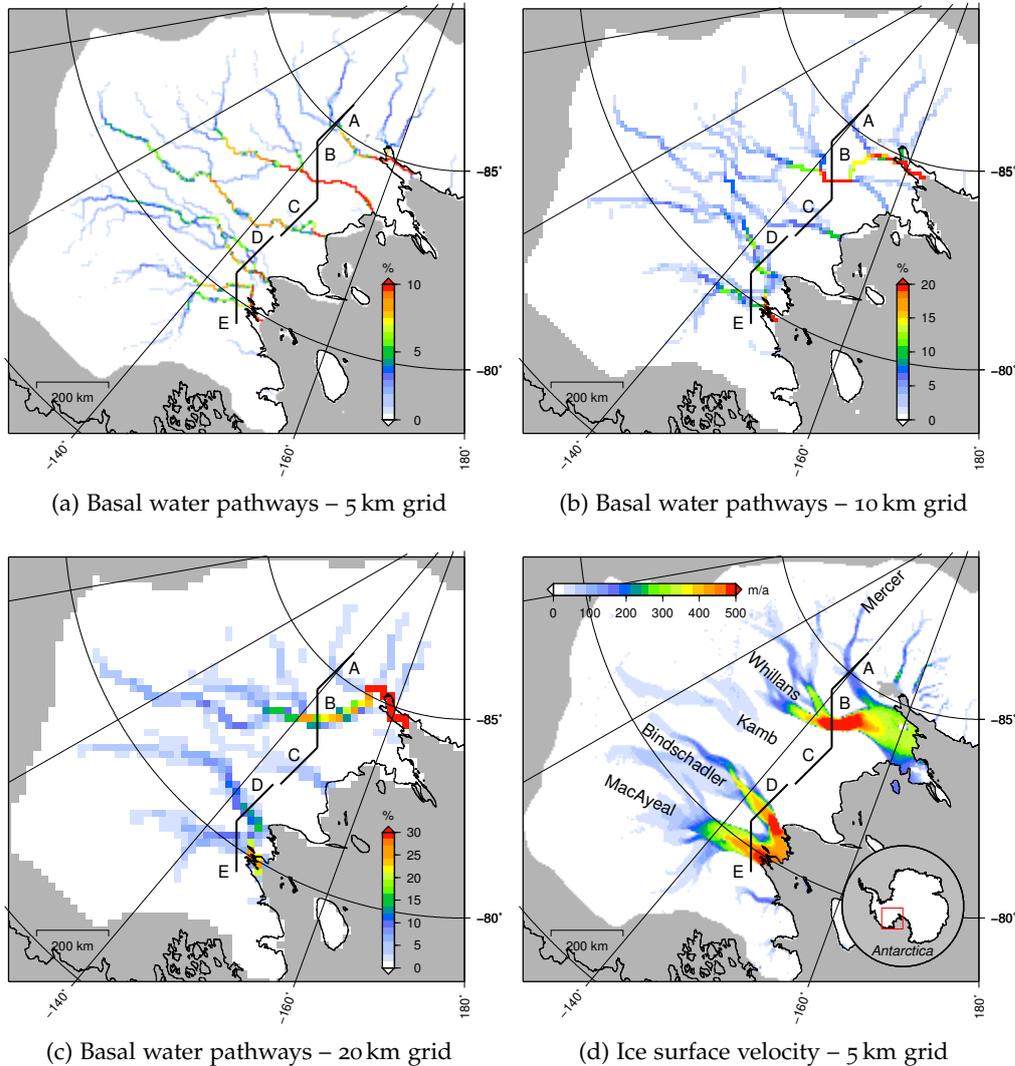
Figure 31: (a-c) Simulated basal water pathways at the Siple Coast for present-day bedrock elevation and ice thickness (Fretwell et al., 2013). The color scale shows the drainage in percent of the total catchment area and is truncated for a better visibility of the pathways, maximum values at the grounding line are 20 % (5 km), 31 % (10 km) and 42 % (20 km). (d) Ice surface velocity (Rignot et al., 2011a), color scale is truncated, maximum values are 709 m a^{-1} in the Whillans and 668 m a^{-1} in the Bindschadler Ice Stream. All figures contain 5 defined cross sections, corresponding to the locations of the Ross Ice Streams (A–E) to quantify the associated water drainage in the following. Bounding ice divides by AGAP and grounding line (black) by NSIDC.

(a) 5 km grid   (b) 10 km grid   (c) 20 km grid
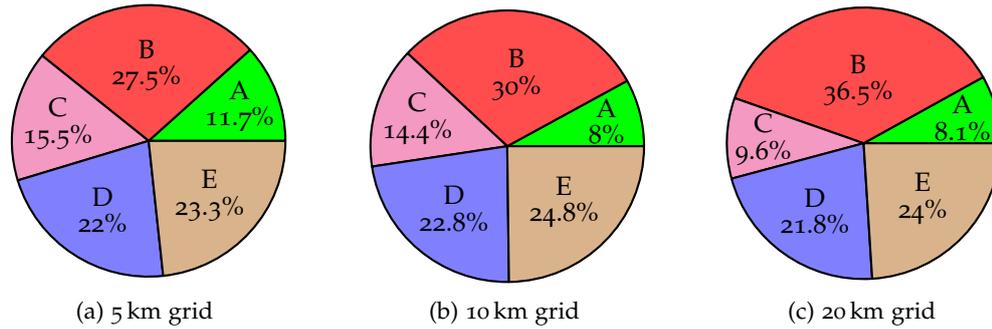
Figure 32: Relative hydraulic catchment areas upstream of the defined cross sections for the Ross Ice Streams (A–E, Fig. 31) as a percentage for three different model resolutions. At present, the largest water catchment area is draining underneath the Whillans Ice Stream (B).

internal deformation provides a powerful heat source for basal melting from which the adjacent ice stream, which itself is comparatively cold, benefits by enhanced lubrication. Additionally, the ice-thickness perturbations induced by ice flow over variable traction create local hydraulic minima. That explains the observed collocation of sticky spots and subglacial lakes (Sergienko and Hulbe, 2011).

The relative sizes of the water catchment areas for all Ross Ice Streams are illustrated in Fig. 32 for the different model resolutions. They reference to the total upstream area of 5 defined cross sections of approximately 140 km length, corresponding to the locations of the main trunks of the 5 major ice streams (Fig. 31).

Beside small variations caused by the applied model resolution they agree very well. The Whillans Ice Stream (B) overspreads the heaviest flow of water which is draining $32 \pm 4.5\,\%$ of the upstream catchments (mean value and error range are derived from the results of the three different model resolutions, Fig. 32). This supports the fact, that Whillans Ice Stream is the fastest flowing Ross Ice Streams with ice surface velocities up to $709\,\mathrm{m\,a^{-1}}$. Beneath Bindschadler (D) and MacAyeal Ice Stream (E) drain the comparable percentages of $22.3 \pm 0.5\,\%$ and $24.1 \pm 0.8\,\%$ of the total catchment area, well-fitting to their similar velocities of up to $668\,\mathrm{m\,a^{-1}}$. As expected, the flow beneath the smaller and slower Mercer Ice Stream (A) drains the smallest part with $9.9 \pm 1.9\,\%$ of the total upstream catchment. Despite the fact that the Kamb Ice Stream (C) stagnated tens of years ago, the basal flow underneath drains the considerable amount of $12.6 \pm 3\,\%$ of the total upstream Siple Coast catchment. Here, complex and yet not fully understood control mechanisms at the ice base appear to rule the ice motion in the face of a observation-proved wet bed as already discussed above.

5.4.3   *Prognostic simulation using ICESat and CryoSat-2 ice surface elevation change rates*

The evolution of the basal drainage network at the Siple Coast is investigated by altering the present-day ice sheet geometry and, thus, the basal pressure conditions according to measured ice surface change rates. In two experiments, using the ice model RIMBAY, the surface elevation change rates observed by the ICESat and the CryoSat-2 campaign (Sec. 5.3, Fig. 30) are added to the present-day ice sheet thickness (Fretwell et al., 2013) at model resolutions of 5, 10 and 20 km. In this way, the ice surface change exactly corresponds to the ice thickness change for grounded ice. However, for floating ice an observed surface change dS/dt refers to a change in ice thickness H according to

$$\frac{dH}{dt} = \frac{1}{1 - \rho_i/\rho_o} \cdot \frac{dS}{dt} \tag{60}$$

where ρ_i and ρ_o are the average densities of the ice shelf and the ocean water. The conversion factor in Eq. 60 is roughly 9, depending on the local ice shelf density. The grounding line, which is the border between grounded and floating ice and the associated different application of the observed dS/dt to the evolution of the ice thickness H, is recalculated in RIMBAY every time step and hence variable. The pattern of the observed dS/dt is based on a fixed grounding line, which is in the majority of cases not exactly collocated with the modeled grounding line. This mismatch leads to huge overestimates of the ice thickness change in the vicinity the actual grounding line, given by the ice model. Since the evolution of the ice shelf thickness is not particularly important for the prognostic calculation of the melt water pathways, the observed surface elevation change rates is simply added to both the thickness of grounded and floating ice nodes, without taking into account Eq. 60. In this way, the error of the thickness evolution is minimized in the area around the grounding line but underestimate the thickness change for the ice shelf which is not relevant for subglacial water tracing.

Again, a constant basal melt rate is prescribed for all grounded ice nodes because the primarily interest goes to the water pathways and the catchment area sizes. This melt rate does not affect the ice thickness in these simulations and is only used for the calculation of the balance flux. The hydraulic potential is recalculated for every time step and is modified accordingly to guarantee flux conservation before the application of the Budd & Warner balance flux scheme (Sec. 3.3.3). Starting with the present-day ice thickness, the satellite derived surface elevation change rates are applied for an extended period of 200 years. This alters the basal hydraulic potential resulting in a modification of the basal water pathways.

5.4.4   *Prognostic subglacial hydrology*

The results for the three different model resolutions are depicted in Fig. 33. The color scale illustrates the percentual drainage of the total catchment area and the 5 cross sections mark the locations of the Ross Ice Streams. Beneath the outer ice streams Mercer (A) and MacAyeal (E) the water flow patterns show no remarkable changes within the next 200 years. However, underneath the central three ice streams the water pathways show a very dynamic behavior. Here, in the middle part of the stagnated Kamb Ice Stream (C), the strongest growth in ice thickness occurs following the satellite observations (compare with Fig. 30). This area is marked with a red circle in all figures. The arising ice bulge increasingly diverts the basal melt water at this spot and leads to a lateral separation of the flow patterns. At present, a major upstream water tributary (tagged with a red star) is feeding into the Kamb (C) and the Whillans Ice Stream (B) area. Within the next 200 years this water influx will be entirely redirected towards the Bindschadler Ice Stream (D). Consequently, the water flow beneath the Kamb Ice Stream will be lacking this contributions. This main characteristic of the computed future water pathways is found consistently for both satellite surface change data sets at model resolution of 5 and 10 km emphasizing the significance of the result. The 20 km resolution model runs reveal this redirection to a lesser extent. Obviously, this resolution is too coarse to point out such details in the water flow patterns.

The basal volume water fluxes towards the grounding line through 5 cross sections corresponding to the locations of the trunks of the Ross Ice Streams under the influence of the ICESat and CryoSat-2 surface change rates are balanced for the next 200 years (Fig. 31). Due to the chosen constant melt rate, the temporal evolution of the water catchment area upstream of every cross section can be computed as a percentage of the total upstream catchment area of all cross sections. Figure 34 shows the evolution of the catchment areas for the model runs with 5 km resolution at a time step of 1 year. The graphs confirm the above analysis of the water pathways. The water catchment areas feeding underneath Mercer (A) and MacAyeal Ice Stream (E) remain stationary over the period of the next 200 years. The water catchment area of the Kamb Ice Stream (C) first gains about 2 % in size from the Whillans (B) catchment within the next 10 years. After that it continuously looses area in favour of the Bindschadler Ice Stream (D). Again the analogy of the influences of the two satellite derived surface change rates on the evolution of the basal hydraulic system is striking. Additionally, the black line in Fig. 34 shows the development of the total upstream catchment areas which reveal very slight variations in size due to the shifting of water sheds by the applied ice thickness changes. Remarkable features are the occurring steps within all graphs. They indicate points in time when larger water tributaries are linked to (or delinked from) a catchment due to the dynamics of the basal water pathways.

(a) 5 km, present-day

(b) 5 km, +200 yr, ICESat

(c) 5 km, +200 yr, CryoSat-2

(d) 10 km, present-day

(e) 10 km, +200 yr, ICESat

(f) 10 km, +200 yr, CryoSat-2

(g) 20 km, present-day

(h) 20 km, +200 yr, ICESat

(i) 20 km, +200 yr, CryoSat-2
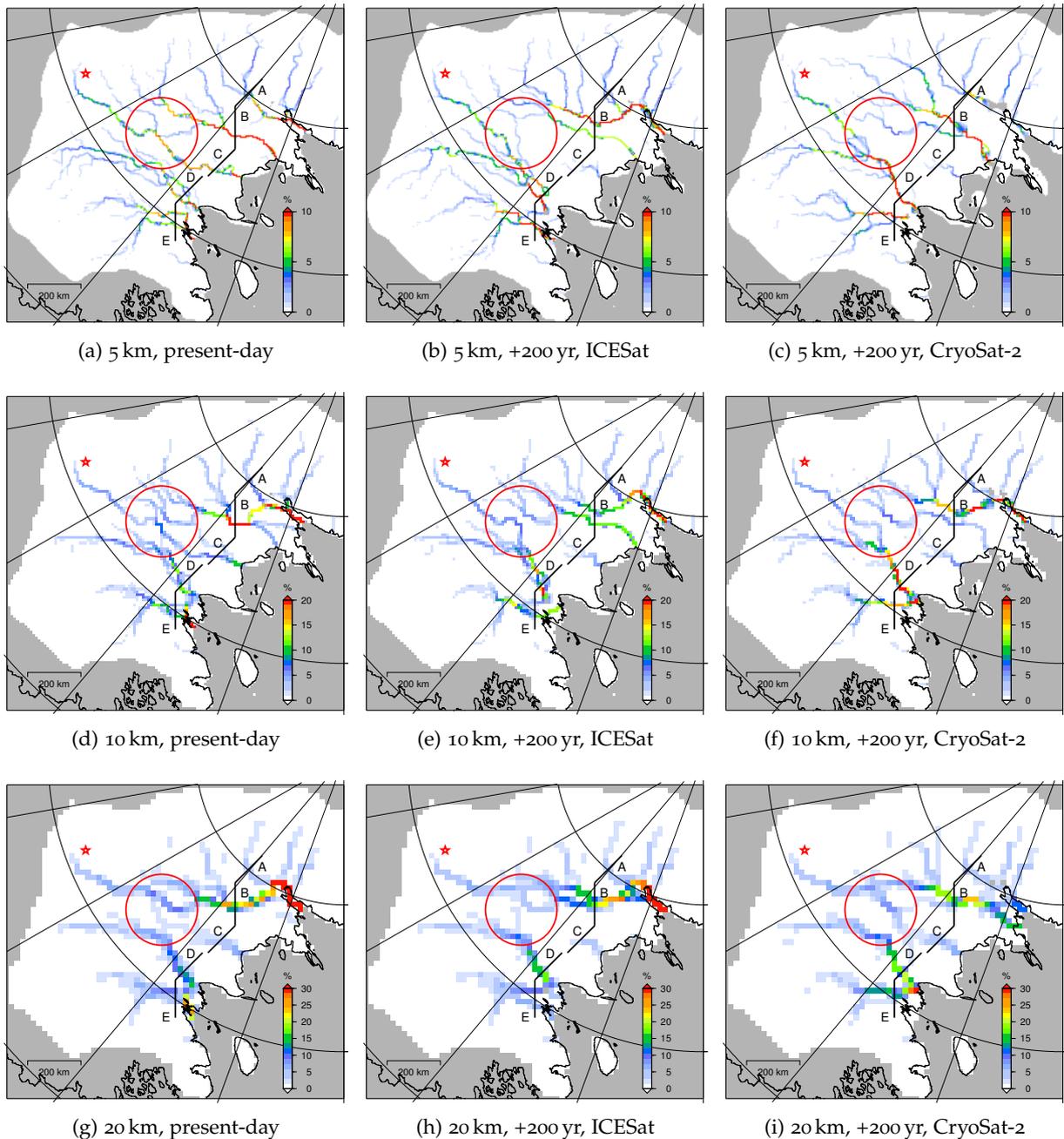
Figure 33: Simulated present-day basal water pathways beneath the Ross Ice Streams (A-E) and their simulated positions after 200 years using ICESat and CryoSat-2 surface elevation change rates at three different model resolutions. The color scale shows the drainage in percent of the total catchment area. The red circle marks the area where a redirection of a major hydraulic tributary (marked with a red star) of the Kamb (C) and Whillans Ice Stream (B) to the Bindschadler Ice Stream (D) takes place at the higher model resolutions. Bounding ice divides by AGAP and grounding line (black) by NSIDC. The designation of longitudes and latitudes is omitted due to the lack of space, for location of map section see, e.g., Fig. 31.

(a) 200 yrs catchment evolution (ICESat)   (b) 200 yrs catchment evolution (CryoSat-2)
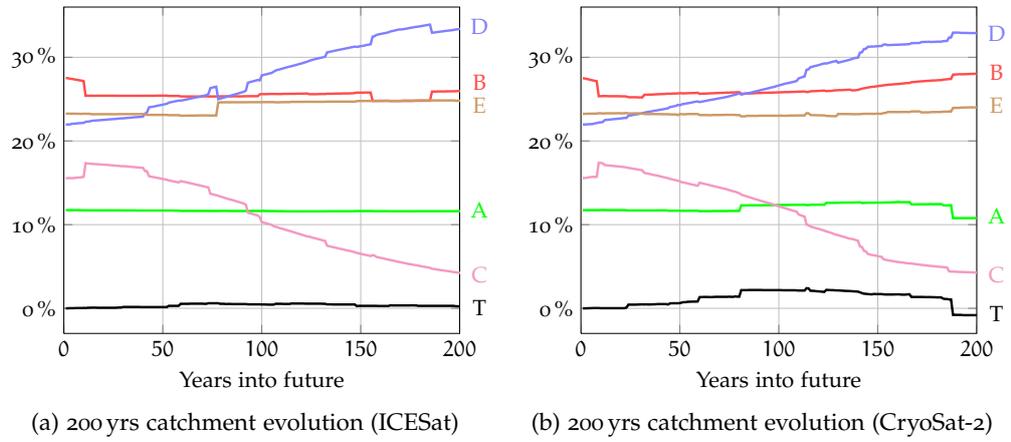
Figure 34: The temporal evolution of the water catchment areas upstream of the defined cross sections for all Ross Ice Streams (A–F, Fig. 33) under the impact of the observed surface elevation changes from (a) ICESat and (b) CryoSat-2 for the next 200 years. T shows the variation of the total upstream catchment area. Model resolution is 5 km.

(a) Catchment change after 200 yrs (ICESat)   (b) Catchment change after 200 yrs (CryoSat-2)
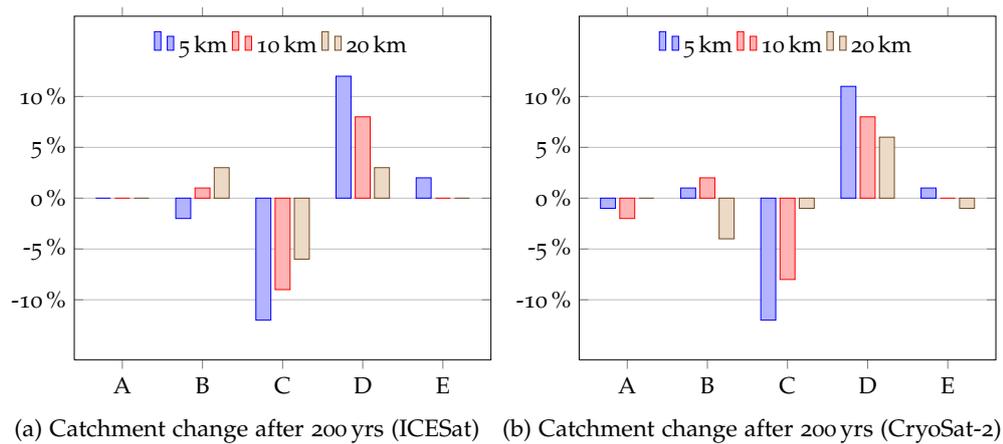
Figure 35: The percentual change of the water catchment areas of the Ross Ice Streams (A–E) after the application of (a) ICESat and (b) CryoSat-2 surface elevation change rates for 200 years at 5, 10 and 20 km model resolution.

The percentual variations of all catchment areas at all model resolutions for the next 200 years are summarized in Fig. 35. Both the ICESat and the CryoSat-2 surface change rates indicate a future loss of about 12 % (at 5 km model resolution) of the water catchment area feeding underneath the Kamb Ice Stream (C) while the water catchment area of the Bindschadler Ice Stream (D) increases by the same amount. In this way, the water catchment area of the Bindschadler Ice Stream grows by roughly 50 % and the lower part of the stagnated Kamb Ice Stream becomes almost hydrologically separated from the upper regions of the Siple Coast. Due to the found spatial correlations between simulated basal water flow and observed ice surface velocities in Sec. 5.4.2, this might be a continuation of the processes which caused the stagnation of the Kamb Ice Stream in the past and could lead to an acceleration of the Bindschadler Ice Stream in the future.

5.5 SUMMARY

The Ross Ice Streams transport mass from the inner WAIS towards the grounding line with velocities of up to several hundred meters per year (Rignot et al., 2011a). However, their positions and velocities are found to be very variable in the past. For instance, observations revealed a stagnation of the Kamb Ice Stream during the last 150 years (e.g., Rose, 1979) and a deceleration of the Whillans Ice Stream by −25.3 % between 1997 and 2009 (Joughin et al., 2002). Since the Ross Ice Streams are dominating the ice dynamics at the Siple Coast, their evolution plays a key role concerning the future mass balance of the WAIS. In order to understand triggers for their spatial and temporal dynamic behavior, the availability of the primary controls on locations of ice streams (Winsborrow et al., 2010) are investigated for the particular region of the Siple Coast. A widely spread and meters thick basal layer of unconsolidated sediments (e.g., Alley et al., 1986) creates the precondition for fast ice flow by bed deformation due to the viscosity of the till, which is significantly lower than the viscosity of ice (e.g., MacAyeal, 1989). The exact locations of the ice streams, however, are determined by the pathways of subglacial melt water flow (e.g., Bentley et al., 1998). This hypothesis is supported by the analysis of ice surface elevation change rates obtained from the ICESat and CryoSat-2 satellite campaigns (Pritchard et al., 2009; Helm et al., 2014). The interpretation of surface change patterns reveals, that redirections of subglacial flow paths are most likely the reason for the observed variability of the central Ross Ice Streams. In addition, the mass balance of the Siple Coast is estimated using satellite altimetry and found to be slightly positive with 52±57 gigatons per year, corresponding to an ice volume growth of about 0.004 %.

The regime of water flow beneath the Ross Ice Streams is assessed to be distributed and the basal water pathways are simulated for the present-day ice sheet topography following the balance flux concept. All current ice stream outlines are found to be clearly associated with areas of enhanced water flow.

Furthermore, the ice velocities of the ice streams are found to be related to the water catchment area sizes draining underneath.

Applying satellite-derived present-day surface elevation changes to the present-day ice sheet surface for 200 years allows an estimation of future basal drainage routes. According to this simulation, the basal water pathways at the Siple Coast are highly sensitive to small ice thickness changes due to the smooth bedrock. A major hydraulic tributary of the Kamb and Whillans Ice Stream is estimated to be redirected underneath the Bindschadler Ice Stream within the next 200 years. Accordingly, the water catchment area feeding underneath the Bindschadler Ice Stream is estimated to grow by about 50 percent while the lower part of the stagnated Kamb Ice Stream becomes increasingly separated from the upper hydraulic tributaries of the Siple Coast. This might be a continuation of the subglacial hydraulic processes which caused the past stagnation of the Kamb Ice Stream. Furthermore, this might also lead to a future increase of the ice velocity within the Bindschadler Ice Stream.

COUPLED MODELING OF ICE DYNAMICS, SUBGLACIAL LAKES AND BASAL DRAINAGE NETWORKS IN A SYNTHETIC DOMAIN

In this chapter, the complex interactions between ice flow dynamics and sub-glacial hydrology are investigated in a coupled modeling study using the *Revised Ice Model Based on Frank Pattyn* (RIMBAY). A new hydrological concept is presented, covering the dynamic evolution of subglacial water drainage pathways and subglacial lakes. The benefits of this new approach are demonstrated in the application to a synthetic model domain and the comparison with the balance flux concept within five different experiments.

6.1 A NEW BALANCED WATER LAYER CONCEPT

A realistic modeling approach has to incorporate several interactions in the evolution of the ice dynamics and the basal hydraulic system of an ice sheet: Ice thickness and bedrock elevation locally define the pressure conditions at the ice-bedrock interface (e.g., Shreve, 1972). Thus, the pathways of basal water flow and the locations of subglacial lakes are determined. Basal water in turn lubricates the base of the ice sheet locally and thus reduces the basal drag of the overlying ice. As a result, fast flowing ice streams can evolve above areas of enhanced subglacial water flow (e.g., Joughin et al., 2004) and the ice velocity increases over subglacial lakes (e.g., Kwok et al., 2000; Pattyn et al., 2004; Thoma et al., 2010, 2012). The basal sliding velocity and the related basal friction influence the thermal regime of the ice sheet and thereby control the basal melt rate (e.g., Parizek et al., 2003; Joughin et al., 2003). The filling or draining of subglacial lakes causes a lifting or lowering of the floating ice above and thus affects the ice sheet geometry (e.g., Gray et al., 2005; Wingham et al., 2006b; Fricker and Scambos, 2009; Smith et al., 2009).

The prediction of subglacial lakes by identifying hollows in the hydraulic potential (Sec. 3.3.2 and 4.2) and the balance flux concept (Sec. 3.3.3) are no appropriate methods to meet the above described requirements of coupled modeling. They do not include the filling and draining of subglacial lakes which depends on the availability of upstream generated melt water and changes of the ice sheet geometry. For this reason, they do not cover the variability of basal water flow downstream of subglacial lakes, too. Another disadvantage of the balance flux concept is the lacking mass conservation on realistic topographies: only a fraction of the melt water produced inside the model domain reaches its margins, because upstream flux contributions are lost at
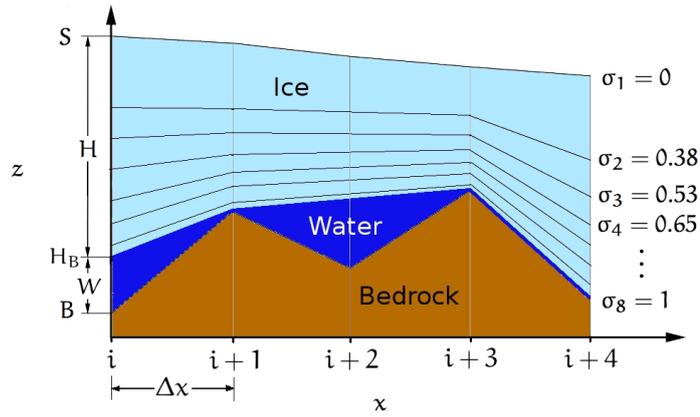
Figure 36: Schematic cross-section of an ice sheet as an example for a FD discretization with 8 terrain-following σ-coordinates, becoming closer from the ice surface S towards the ice base H_B. In the following model runs 21 σ-levels are used. The ice thickness is given by $H = S - H_B$. The water layer W is situated between ice base H_B and bedrock B and can locally also have a thickness of zero.

local minima of the hydro-potential surface. Additional computational effort is necessary to conserve the flux over these hollows (Sec. 3.3.3).

To transfer the advantages of the balance flux concept and to overcome its weaknesses, the balanced water layer concept is introduced (Goeller et al., 2013). This new approach assumes a distributed flow regime and is fully mass conservative on any topography without the necessity of any additional modifications. For inclined regions of the hydraulic potential it yields the balance flux. In addition, this concept allows water to accumulate in hollows of the hydraulic potential and hence to form subglacial lakes. Once lakes are filled to their maximum level, melt water generated upstream flows through the lakes to their discharge point and thus contributes to downstream flow.

6.1.1 *General formulation*

For distributed subglacial water flow regimes the basal hydraulic potential p (Shreve, 1972) at the ice-bedrock interface can be expressed as

$$p = \rho_{\text{water}} gB + \rho_{\text{ice}} gH \tag{61}$$

where B is the bedrock elevation, H is the ice thickness, g is the gravitational acceleration and ρ_{water} and ρ_{ice} are the densities of fresh water and ice (Sec. 3.3.1). Defining a water layer with thickness W (Fig. 36) between bedrock with elevation B and ice base H_B leads to

$$p = \rho_{\text{water}} g(B + W) + \rho_{\text{ice}} gH \tag{62}$$

where p is the hydraulic potential at the top of the water layer respectively at the ice base. Equation 62 with $[p] = \text{Pa}$ is converted into the water equivalent

hydraulic potential $P = p/(\rho_w g)$ with $[P] = m$ a.s.l.. In addition, a time index t is added, reflecting the fact, that bedrock B, ice thickness H, water layer thickness W and consequently the hydraulic potential P are time-dependent in general:

$$P^t = B^t + W^t + H^t \frac{\rho_{ice}}{\rho_{water}}. \tag{63}$$

The balance equation for the evolution of the water layer W^t is given by

$$\frac{\partial W^t}{\partial t} = -\operatorname{div}(W^t \bar{v}^{(water)}) + M_b^t \tag{64}$$

where $\bar{v}^{(water)}$ is the vertical averaged water velocity and M_b^t is the basal melt rate. The values for bedrock elevation B^t, ice thickness H^t and basal melt rate M_b^t are provided by an ice model, which is coupled to the hydrology model. Presuming that the water velocity is much higher than the ice velocity, the hydrology can be brought to an equilibrium state with the ice sheet geometry on every time step. Stating that the water velocity follows the gradient of the hydraulic potential, Eq. 64 can be solved iteratively: First the current water layer thickness W^t is computed by adding the melt water input $M_b^t \cdot \Delta t$ to the water layer thickness W^{t-1} of the previous time step. Then the available water is redistributed along the gradient of the hydraulic potential (Eq. 63) in an iterative way until a stationary basal water distribution W^t is found.

This basic concept is applicable to all kind of ice models, whether they use a finite difference, finite element or finite volume discretization. The ice model RIMBAY is based on FD. Consequently, the implementation of the hydrology model is formulated in FD, too, allowing a direct coupling of both models.

6.1.2 *Implementation for finite differences*

The potential $P_{i,j}^t$ for a grid cell (i,j) at time step t is composed of a constant part $P_{i,j}^{*t} = B_{i,j}^t + H_{i,j}^t \, \rho_{ice}/\rho_{water}$ and the adjustable water layer thickness $W_{i,j}^t$, which has to be balanced out with respect to the potential $P_{i,j}^t$. The iteration is all done for time step t, so the time index is omitted for reasons of clarity.

$$P_{i,j} = P_{i,j}^* + W_{i,j} \tag{65}$$

The balanced water layer concept operates on an Arakawa C-grid (Arakawa and Lamb, 1977). Hence, the gradients of the hydraulic potential $P_{i,j}$ are defined at the margins of the grid cells as

$$\frac{\partial P_{i,j}}{\partial x} = \frac{P_{i+1,j} - P_{i,j}}{\Delta x} \quad \text{and} \quad \frac{\partial P_{i,j}}{\partial y} = \frac{P_{i,j+1} - P_{i,j}}{\Delta y}. \tag{66}$$

The instantaneous transport of water between adjacent grid cells for one iterative step is expressed by $T_{i,j}^x$ and $T_{i,j}^y$, where the sign gives the direction and the product with the grid size $\Delta x \Delta y$ the volume of the water transport (Fig. 37). In
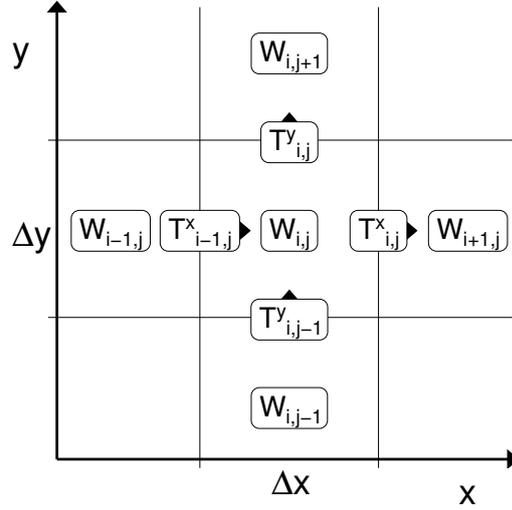
Figure 37: Notation for staggered Arakawa C-grid: at the grid center: basal water layer thickness $W_{i,j}$, hydraulic potential $P_{i,j}$, normalization $N_{i,j}$, water flux $\phi_{i,j}$ (for coupling to an A-grid ice model), at the grid cell edges: water transport $T_{i,j}^x$ and $T_{i,j}^y$, hydraulic gradients $\partial P_{i,j}/\partial x$ and $\partial P_{i,j}/\partial y$, water flux $\phi_{i,j}^x$ and $\phi_{i,j}^y$ (for coupling to an C-grid ice model).

order to normalize all directional water transports *out* of a grid cell (i,j), the norm $N_{i,j}$ is introduced with

$$
\begin{aligned}
N_{i,j} = {} & \max\left(\frac{\partial P_{i-1,j}}{\partial x}, 0\right) + \max\left(-\frac{\partial P_{i,j}}{\partial x}, 0\right) \\
& + \max\left(\frac{\partial P_{i,j-1}}{\partial y}, 0\right) + \max\left(-\frac{\partial P_{i,j}}{\partial y}, 0\right).
\end{aligned}
\tag{67}
$$

The differences of the potential between adjacent grid cells are defined as

$$
\begin{aligned}
\Delta_x P_{i,j} &= |P_{i+1,j} - P_{i,j}| \\
\Delta_y P_{i,j} &= |P_{i,j+1} - P_{i,j}|.
\end{aligned}
\tag{68}
$$

So the water transports $T_{i,j}^x$ and $T_{i,j}^y$ with $[T_{i,j}^{x/y}] = \mathrm{m}$ can be calculated for all grid cell edges by

$$
T_{i,j}^x = -\frac{\partial P_{i,j}}{\partial x}
\begin{cases}
\dfrac{\min(W_{i,j}, \varepsilon\,\Delta_x P_{i,j})}{N_{i,j}}, & \dfrac{\partial P_{i,j}}{\partial x} < 0 \\[2.2ex]
\dfrac{\min(W_{i+1,j}, \varepsilon\,\Delta_x P_{i,j})}{N_{i+1,j}}, & \text{else}
\end{cases}
$$

$$
\tag{69}
$$

$$
T_{i,j}^y = -\frac{\partial P_{i,j}}{\partial y}
\begin{cases}
\dfrac{\min(W_{i,j}, \varepsilon\,\Delta_y P_{i,j})}{N_{i,j}}, & \dfrac{\partial P_{i,j}}{\partial y} < 0 \\[2.2ex]
\dfrac{\min(W_{i,j+1}, \varepsilon\,\Delta_y P_{i,j})}{N_{i,j+1}}, & \text{else}.
\end{cases}
$$

with the convergence parameter $\varepsilon \in (0,1)$. They are determined by the direction, the amount and the normalization of the water transfer. The sign of the hydraulic gradient (Eq. 66) gives the direction of the water transport in

Eq. (69). The normalization is done by the ratio of the hydraulic gradient and $N_{i,j}$ of the water-contributing (upstream) grid cell. To achieve convergence, a water amount corresponding to a fraction ε of the differences of the potential (Eq. 68) is transported. These transfered amounts are bounded by the maximum available volume of water so that $\varepsilon \Delta_x P_{i,j}$ or $\varepsilon \Delta_y P_{i,j}$ will never exceeds $W_{i,j}$.

Finally, the water layer for the next iteration step is obtained by

$$W_{i,j}^{(\text{iter.}+1)} = W_{i,j}^{(\text{iter.})} + T_{i-1,j}^x - T_{i,j}^x + T_{i,j-1}^y - T_{i,j}^y, \tag{70}$$

and it is started again at Eq. (65), until the change of the water layer thickness for all n grid cells is found under a certain threshold $\Delta W^{(\text{threshold})}$

$$\frac{1}{n} \sum_{i,j} \left| W_{i,j}^{(\text{iter.}+1)} - W_{i,j}^{(\text{iter.})} \right| \leqslant \Delta W^{(\text{threshold})}. \tag{71}$$

Here, the target precision of the basal water distribution rules the choice of $\Delta W^{(\text{threshold})}$, where a smaller value leads to a better levelness of subglacial lake surfaces but needs further iterations.

Closed lateral boundary conditions for the balanced water layer concept (e.g., at ice-nunatak interfaces) can be easily implemented by setting the water transport to zero at the respective grid cell edges. Open lateral boundaries do not require a special treatment. However, one can sum up all outward water transports at these margins to yield a water flux in order to force another coupled model, e.g. an ocean model at ice-ocean interfaces.

6.1.3   *Scalar and vector water fluxes on C- and A-grids*

The scalar volume flux Φ with $[\Phi] = \text{m}^3\text{s}^{-1}$ defines the total water volume which is horizontally transfered between adjacent grid cells within time step Δt. On a C-grid, consequently, $\Phi_{i,j}^x$ and $\Phi_{i,j}^y$ are obtained, which are defined at the grid cell edges. These volume fluxes are computed by adding up all instantaneous water transports (Eq. 69) during the above iteration:

$$\Phi_{i,j}^x = \frac{\Delta x \Delta y}{\Delta t} \sum_{\text{iter.}} T_{i,j}^x, \qquad \Phi_{i,j}^y = \frac{\Delta x \Delta y}{\Delta t} \sum_{\text{iter.}} T_{i,j}^y. \tag{72}$$

As the volume flux (Eq. 72) between two grid cells can be considered to be orthogonal to the grid cell edges, the vector flux ϕ with $[\phi] = \text{m}^2\text{s}^{-1}$ is directly derived by

$$\phi_{i,j}^x = \frac{\Phi_{i,j}^x}{\Delta y}, \qquad \phi_{i,j}^y = \frac{\Phi_{i,j}^y}{\Delta x}. \tag{73}$$

It is fairly simple to couple the water flux calculated by the balanced water layer concept to an ice model running on a C-grid, because both water flux and ice velocities are determined at the edges of a grid cell.

Some more transformations are required if one wants to derive a scalar and vector water flux at the grid cell center for a coupling with an A-grid ice model. First, the total volume flux $\Phi_{i,j}^{(out)}$ through a grid cell is approximated by the outflows $\Phi_{i,j}^{x}$ and $\Phi_{i,j}^{y}$ across the grid cell edges to

$$
\begin{aligned}
\Phi_{i,j}^{(out)} = &\max\left(-\Phi_{i-1,j}^{x}, 0\right) + \max\left(\Phi_{i,j}^{x}, 0\right) \\
&+ \max\left(-\Phi_{i,j-1}^{y}, 0\right) + \max\left(\Phi_{i,j}^{y}, 0\right).
\end{aligned}
\tag{74}
$$

Then the flux direction $\theta_{i,j}$ relative to the grid orientation is determined by fitting a plane to the hydraulic potentials of the next four neighbor cells. According to Budd and Warner (1996) the vector flux $\phi_{i,j}$ at the center of a grid cell with side length $L = \Delta x = \Delta y$ is similarly to Eq. 59 in Sec. 3.3.3 given by

$$
\phi_{i,j} = \frac{\Phi_{i,j}^{(out)}}{L\left(|\cos\theta_{i,j}| + |\sin\theta_{i,j}|\right)}.
\tag{75}
$$

The obtained balance vector flux $\phi_{i,j}$ is the steady-state solution of the water balance equation (Eq. 64) with $\operatorname{div}\phi_{i,j} = M_{i,j}$.

6.2   COUPLING OF HYDROLOGY AND ICE MODEL

The three-dimensional thermomechanical finite differences ice-flow model RIM-BAY is applied in Shelfy Stream Approximation mode (Eq. 24 and 25, Sec. 2.2.2) (e.g., MacAyeal, 1989; Pattyn, 2010; Thoma et al., 2014). The Shelfy Stream Approximation is chosen for grounded ice instead of the Shallow Ice Approximation to incorporate shear stress coupling between adjacent grid cells (e.g., Greve and Blatter, 2009). The computations for the ice dynamics are all performed on an Arakawa A-Grid (Arakawa and Lamb, 1977), treating model variables, e.g., bedrock elevation, ice thickness and velocity, as located at the grid center.

WATER LAYER − ICE GEOMETRY   With the surface elevation S in the horizontal ice velocity calculation (Eq. 24, Sec. 2.2.2) and the relation $S = B + W + H$ the geometry of the ice model is directly coupled to the hydrology model by the basal water layer W (Eq. 63 and 64). The basal water layer, which is situated between bedrock and ice base, can gain a certain thickness and thus lift the overlying ice by this amount.

WATER LAYER / LAKE − ICE SLIDING   All grid cells where the basal water layer thickness W exceeds one meter are treated as subglacial lakes and the basal friction parameter β^2 (Eq. 25, Sec. 2.2.2) for the calculation of the horizontal ice velocity (Eq. 24, Sec. 2.2.2) is fixed to zero there.

WATER FLUX − ICE SLIDING   To parameterize the hydrology-dependent basal ice sliding a relevant coupling variable would be the basal water pressure (e.g., Clarke, 2005; Cuffey and Paterson, 2010; Schoof, 2010), which is not

provided by the balanced water layer approach. Similar balance flux applications (e.g., Le Brocq et al., 2009) assume a laminar water flow and then couple the sliding to the steady-state water-film depth. In order to avoid further assumptions about the particular type of the distributed water flow regime, a simple physically plausible correlation of the sliding rate C (Eq. 30, Sec. 2.2.2) and the subglacial water flux ϕ (Eq. 75) is introduced. It enhances the common calculation of the basal friction parameter β^2 (Eq. 33, Sec. 2.2.2) by introducing a water flux dependent sliding rate $C(\phi)$:

$$C(\phi) = C_0 \, \exp^{-m\frac{\phi}{\phi_0}} \tag{76}$$

with sliding coefficient $m = 1/3$, $C_0 = 10^7 \, \mathrm{Pa\,m^{-1/3}\,s^{1/3}}$ (Pattyn et al., 2013) and the reference flux ϕ_0, scaling this correlation. Consequently, an increased flux ϕ implies a smaller ice sliding rate $C(\phi)$ and thus an enhanced slipperiness, which decreases β^2 to a possible minimum of zero. A reasonable reference flux ϕ_0 can be obtained by adapting it to observed ice surface velocities. An overview of indirectly estimated basal water fluxes for Antarctica is given in Sec. 3.2.1.

WATER LAYER – BASAL MELTING   The ice temperature is calculated by solving the energy conservation equation and neglecting the horizontal diffusion for 21 terrain-following vertical layers, which become thinner towards the ice base (Fig. 36). The basal melt rate M_b is calculated with Eq. 41 in Sec. 2.2.3 and forces the water layer thickness W in every time step (Sec. 6.1.1).

6.3 MODEL DOMAIN, EXPERIMENTS AND RESULTS

In the present study, a rectangular model domain on the scale of $60 \times 200 \, \mathrm{km^2}$ with a grid resolution of 2 km is used (Fig. 38). Closed free-slip boundaries are defined at the lateral ice sheet margins and the ice divide. At the ice sheet front a free-flux boundary allows mass loss, which could be interpreted as calving into an adjacent ocean. In experiments, where a hydrological model is applied (Tab. 3), the ice sheet front is treated as an open and the lateral margins and the ice divide as closed hydrological boundaries.

The bedrock consists of randomly distributed peaks with a linear increasing random amplitude up to 1 km. This artificial topography with mountains and troughs roughly mimics typical characteristics of observations, e.g. in the Gamburtsev Mountains region in East Antarctica (Fig. 40b, Bell et al., 2011) or the Ellsworth Mountains (Woodward et al., 2010) in West Antarctica. Although the used terrain generation algorithm overestimates the number of enclosed bedrock basins compared to observations (e.g., Anderson and Anderson, 2010), it is well suitable to demonstrate the balanced water layer concept.

In this study, the glacial isostatic adjustment is omitted and a constant bedrock elevation B is applied for simplicity (Eq. 63). All experiments are car-
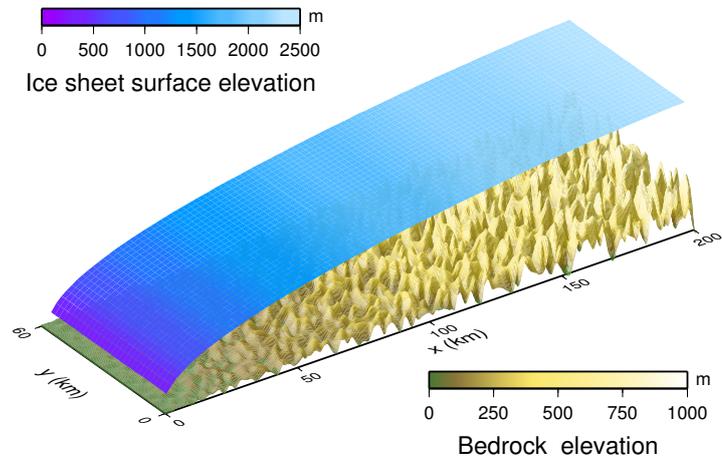
Figure 38: Model domain with mountainous bedrock and steady-state ice sheet topography in the control run (CR).

	Hydrology model	Coupling Hydrology		Ice
BW	Balanced water layer concept	Water layer	⇄ →	Geometry Melting Sliding
BWF	Balanced water layer concept	Water layer ↓ Water flux	⇄ →	Geometry Melting Sliding
BF, BF$^+$	Balance flux concept	Water flux	⇄ →	Melting Sliding

Table 3: Schematic overview of the coupling between hydrology and ice model for all coupled experiments.

(a) Absolute ice velocities

(b) Basal melt rates
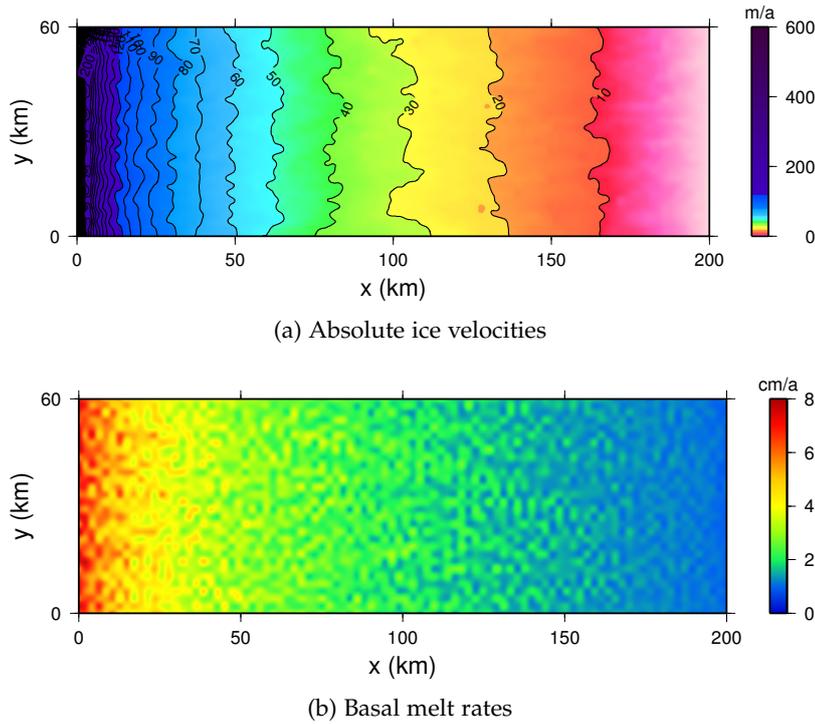
Figure 39: Control run (CR)

ried out with the same bedrock topography to guarantee comparability and are run for 20 000 years until both the ice dynamics and the hydrological system are in a steady state. A time step Δt of 1 year guarantees a compliance with the Courant-Friedrich-Levy criterium:

$$|\vec{v}|\,\frac{\Delta t}{\Delta x} \leqslant 1. \tag{77}$$

The ice surface temperature T_s is set to $-10\,^{\circ}\text{C}$, the accumulation rate M_S is $0.5\,\text{m}\,\text{a}^{-1}$, and the geothermal heat flux G is $0.15\,\text{W}\,\text{m}^{-2}$ all over the model domain. Compared to measurements in Antarctica, the above surface temperature (Comiso, 2000) and accumulation rate (Arthern et al., 2006) is relatively high. Also the chosen geothermal heat flux is in the upper range of the estimated spectrum for Antarctica (Shapiro and Ritzwoller, 2004; Maule et al., 2005), which simply leads to higher melting rates and thus to a faster convergence of the basal hydraulic system in the model runs.

6.3.1 *Control run without hydrology (CR)*

All experiments start with the same steady-state ice sheet (Fig. 38), which is called the control run (*CR*). The total accumulation balances the mass loss at the ice sheet front at an ice volume of 17 001 km^3. The ice thickness of this parabolic ice sheet varies from 2 294 m at the ice divide to 263 m at the ice sheet front, where the ice velocity increases up to 535 m a^{-1}. The variations of the ice velocity show clearly the influence of the mountainous bedrock (Fig. 39a). The melt rate (Eq. 41) is taken into account for the calculation of the ice thickness

evolution (Eq. 44) and the vertical ice velocity. However, no subglacial hydrology model has been applied. Accordingly, there is no flux-sliding-coupling (Eq. 76) incorporated and $C(\phi)=C_0$. Figure 39b shows the melt rates, which are lowest in the interior of the ice sheet, where the ice velocities are low and thus the melting is governed by the geothermal heat flux (Eq. 41). In the vicinity of the ice divide they range from about $1\,\mathrm{mm\,a^{-1}}$ to maximum values of $15\,\mathrm{mm\,a^{-1}}$ in deep bedrock troughs, where the ice thickness reaches its maximum and thus insulates the ice sheets base best from the surface temperature. Towards the ice sheet front the ice velocities increase and the melting is clearly dominated by frictional heating, reaching values up to $76\,\mathrm{mm\,a^{-1}}$. The modeled melt rates are higher than estimates for the Antarctic Ice Sheet (e.g., Carter et al., 2009a; Pattyn, 2010), due to the chosen thermal boundary conditions for a faster convergence of the hydraulic system in the next experiments.

6.3.2 *Balanced water layer: lake-sliding coupling (BW)*

Starting from the control run, the balanced water layer concept is applied with $C(\phi) = C_0$. As a consequence melt water is able to accumulate in hollows of the hydraulic potential and starts to form subglacial lakes. The convergence parameters are set to $\Delta W^{(\mathrm{threshold})} = 10^{-10}$ m and $\varepsilon = 0.5$, which is a good compromise between fast convergence and reasonable accuracy. The hydraulic system reaches a steady state after running the model for 20 000 years, meaning all subglacial hollows are filled and the entire generated melt water of $0.288\,\mathrm{km^3\,a^{-1}}$ is leaving the model domain at the ice sheet front. Grid cells, where the basal water layer thickness exceeds one meter, are defined as subglacial lakes. Above these lakes a stress-free ice base is assumed. In total, 266 subglacial lakes are found covering $2\,256\,\mathrm{km^2}$ with a water volume of $372\,\mathrm{km^3}$. The percentage of the bed covered with subglacial lakes is 18.8 % for the model domain. Compared to estimates of the lake coverage for the whole Antartic continent with $\approx 0.4\,\%$ ($\approx 50\,000\,\mathrm{km^2}$ of known lakes, Wright and Siegert, 2011) this number is high. The discrepancy can be explained by the used topography. It is meant to loosely resemble particular Antarctic areas with a mountainous bedrock (and even for these it overestimates the number of enclosed basins) and is thus not representative for the whole Antarctic continent. Fitting to observations the majority of the lakes in *BW* is situated close to the ice divide, where the ice surface gradient is low and the bedrock elevation gradients are high (Tabacco et al., 2006). The surfaces of the lakes are inclined due to the basal pressure conditions resulting from the ice thickness gradients over the lakes (Fig. 40a). This corresponds to observations in Antarctica (Fig. 40b), where lake surfaces reflect the ice surface slope with an amplification of factor nine (e.g., Bell et al., 2011). The largest lakes reach up to $100\,\mathrm{km^2}$ extent and water depths up to $636\,\mathrm{m}$ (Fig. 41a). The ice velocity in *BW* shows clear evidence of spatial variations in basal stresses, as there are many spots with an enhanced velocity
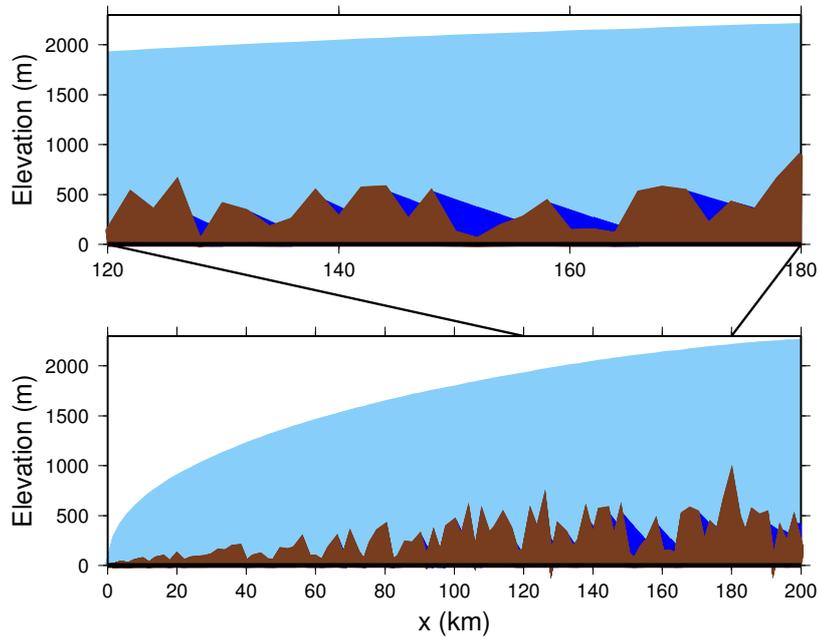
(a) Model results
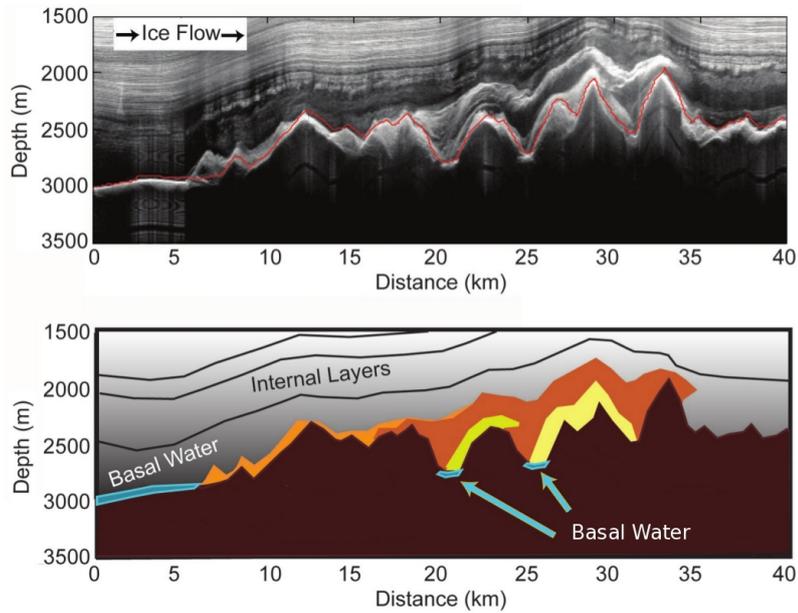
(b) Observations

Figure 40: (a) Profile of the modeled ice sheet at y=22 km for experiment BW, showing several subglacial lakes and their inclined surfaces due to the ice thickness gradient. (b) Radar observations reveal basal water reflections in valleys of the Gamburtsev Mountains, Antarctica (Fig. after Bell et al., 2011).

(a) Water depths of subglacial lakes

(b) Absolute ice velocities
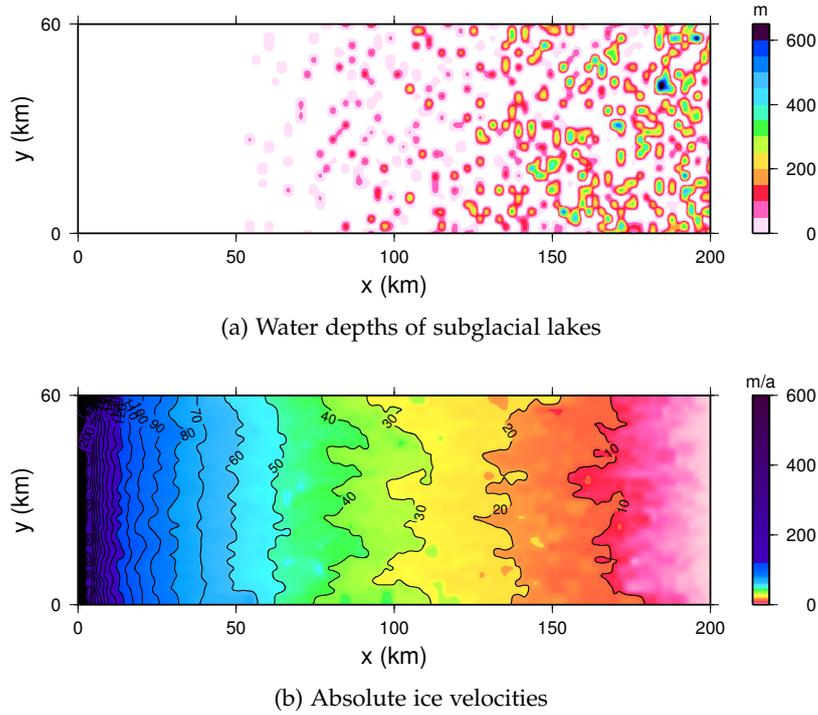
Figure 41: Balanced water layer concept with lake-sliding coupling (BW)

in correlation with the location of subglacial lakes (Fig. 41b), and the total ice volume decreases to $16\,443\,\text{km}^3$, which will be discussed in Sec. 6.4.

6.3.3 *Balanced water layer: lake- and flux-sliding coupling (BWF)*

In a second experiment *BWF*, again the balanced water layer concept is applied but extended *BW* by coupling the basal water flux (Eq. 75) to the basal sliding rate (Eq. 76). The reference flux is set to $\phi_0{=}10^4\,\text{m}^2\,\text{a}^{-1}$, which is just an example to illustrate the flux-sliding interaction. The generated melt water amounts to $0.286\,\text{km}^3\,\text{a}^{-1}$. Figure 42a shows the basal balance water flux with a maximum of $19\,794\,\text{m}^2\,\text{a}^{-1}$, forming a branching stream system. All the melt water from upstream areas flows through plenty of subglacial lakes towards the ice sheet front. The feedback of the flux-sliding coupling to the distribution and water volume of the subglacial lakes is minimal. In comparison to *BW* their total volume diminishes by only $2.2\,\%$ to $364\,\text{km}^3$. As a consequence of the flux-sliding coupling ice streams evolve above the very focused subglacial water streams. They are about $4\,\text{km}$ wide and move about $20\,\text{m}\,\text{a}^{-1}$ ($\approx 50\,\%$) faster than the adjacent ice (Fig. 42b). Arteries of increased ice velocities reach also far upstream into the ice sheet where velocity differences to *BW* of up to $5\,\text{m}\,\text{a}^{-1}$ ($\approx 25\,\%$) can be seen locally. The ice velocity reaches its maximum with $595\,\text{m}\,\text{a}^{-1}$ at the ice sheet front. Consequently, the total ice volume diminishes to $15\,769\,\text{km}^3$.

(a) Basal balance water flux

(b) Absolute ice velocities
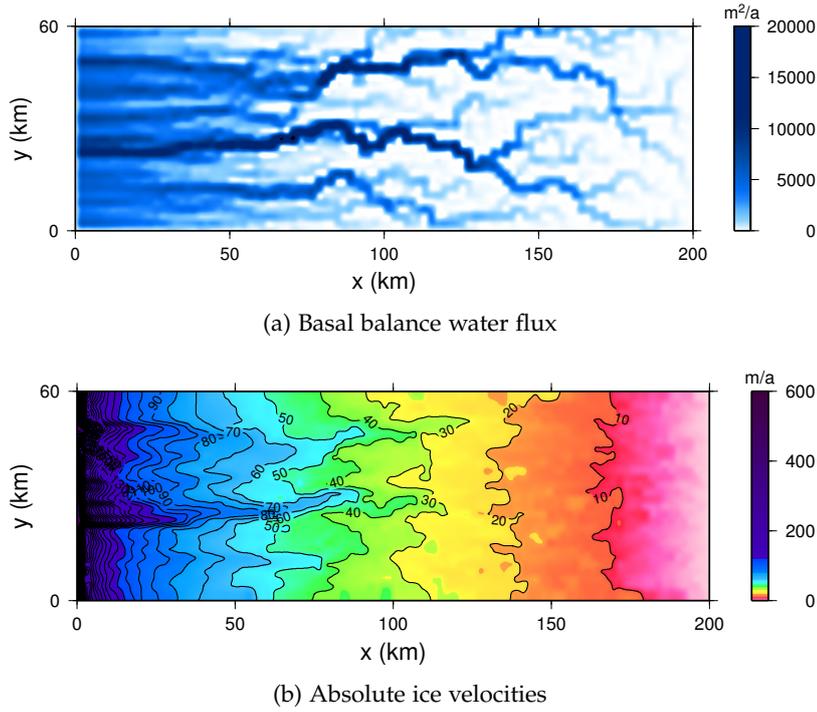
Figure 42: Balanced water layer concept with lake- and flux-sliding coupling (BWF)

6.3.4 *Balance flux: flux-sliding coupling (BF and BF⁺)*

Two more benchmark experiments are performed, where the Budd and Warner (1996) balance flux scheme (Sec. 3.3.3) is applied with the same flux-sliding coupling as in *BWF*. For the calculation of the balance flux the hydraulic potential (Eq. 63) is used with $W = 0$, because the balance flux scheme does not provide the accumulation of water within subglacial hollows.

In experiment *BF* $0.307\,\mathrm{km}^3\,\mathrm{a}^{-1}$ melt water is produced. But only a constant water flux of $0.166\,\mathrm{km}^3\,\mathrm{a}^{-1}$ (54 %) leaves the model domain at the ice sheet front, while the significant amount of $0.141\,\mathrm{km}^3\,\mathrm{a}^{-1}$ (46 %) is lost in hollows of the hydraulic potential. The ice volume diminishes as a consequence of the flux-sliding coupling to $16\,722\,\mathrm{km}^3$.

The limitation of *BF* are overcome in *BF⁺* by modifying the hydraulic potential before the calculation of the balance flux. All hollows in the hydraulic potential are filled up and the resulting flats are slightly tapered into the direction of their previously identified discharge point. In this way, flux conservation is guaranteed (comparable with, e.g., Le Brocq et al., 2009) and the entire generated melt water of $0.312\,\mathrm{km}^3\,\mathrm{a}^{-1}$ leaves the model domain at the ice sheet front. The flux-sliding coupling causes a decrease of the ice volume to $16\,224\,\mathrm{km}^3$.

6.4 COMPARISON AND DISCUSSION OF THE RESULTS

The comparison of the subglacial water balance for all experiments is shown in Fig. 43a. In *BF* 46 % of the generated melt water is lost inside the model domain.
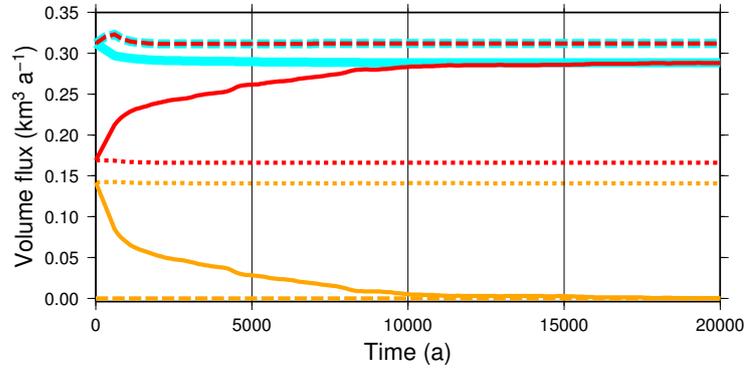
(a) Subglacial water balance
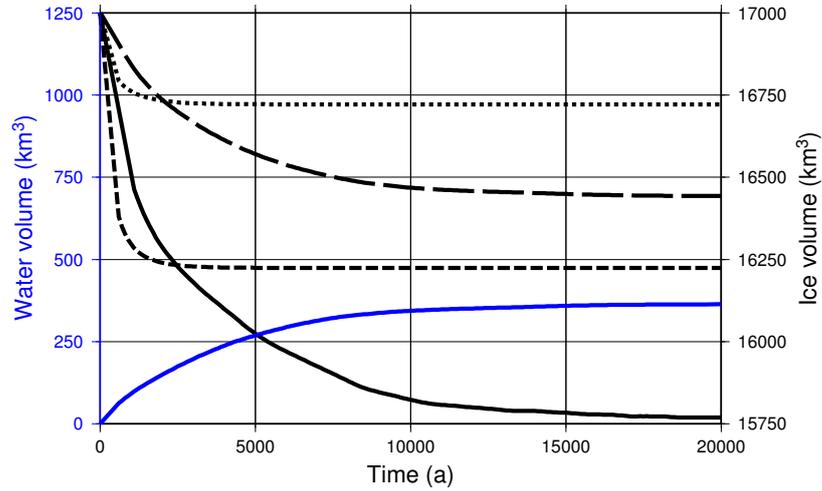
(b) Ice and subglacial lake volume

(c) Key

Figure 43: (a) Subglacial water balance and (b) ice and subglacial lake volume for all
experiments. (Experiments with very similar results share one line style.)

This confirms the necessity of the preceding modification of the hydraulic potential in BF^+ to obtain reasonable results with that method, which means an additional computational effort. This extra effort is not required for the balance water layer concept, which is water volume conserving on any hydraulic potential. Additionally, the fluxes into hollows of the hydraulic potential and over the model margin show a time-dependent behavior in $BW \& BWF$. Both start with the same values as BF. Then the flux into hollows of the hydraulic potential decreases as these slowly fill up. Simultaneously, the flux over the model margin increases. The small steps in the time series of the fluxes indicate the time when single hollows are filled and thus the entire melt water produced in their upstream catchment area starts contributing to downstream areas and the flux over the model margin. Once all hollows are filled, the entire generated melt water is transported through them and contributes to the flux over the model margin as in BF^+. So the balanced water layer concept is able to describe the transitional behavior of the hydraulic system between BF and BF^+.

The differences of the absolute ice velocity between the experiments and the control run reveal the influence of the basal hydraulic system on ice dynamics and mass balance. BW indicates that ice velocities above subglacial lakes are increased, while downstream of the lakes the velocity decreases again (Fig. 44a). This effect is consistent with observations of the surface velocity field based on radar interferometry, e.g., for Lake Vostok by Kwok et al. (2000), and could be reproduced by models for a single lake (Pattyn et al., 2004; Thoma et al., 2010, 2012). Although the velocity increase of the ice in BW is only a local phenomenon above subglacial lakes, they do have an impact on the mass balance of the entire ice sheet. Figure 43b shows the temporal development of the total ice and lake volume for the different experiments (Summary in Tab. 4). Compared to the control run, for BW an ice loss of $558 \, \mathrm{km^3 \, a^{-1}}$ (–3.3 %) is found. Taking into consideration the stored subglacial water volume of $372 \, \mathrm{km^3}$, which replaced the corresponding ice volume, there is still an overall volume ($V_{\mathrm{ice}} + V_{\mathrm{water}}$) loss of $186 \, \mathrm{km^3}$ (–1.1 %). In comparison to the direct mass loss caused by basal melting of $0.288 \, \mathrm{km^3 \, a^{-1}}$, the indirect contribution of the accumulated basal water to the mass balance of the ice sheet is large.

Due to the flux-sliding coupling the ice velocity field in BWF shows also the imprint of the basal water fluxes (Fig. 44b). Ice streams drain mass from the central areas and thus cause a thinning and flattening of the ice sheet. That again results in a lower basal shear stress (Eq. 32, Sec. 2.2.2), which is driven by the ice surface gradient. Consequently, less hydrologically active areas beside the ice streams show significantly lower ice velocities and therefore contribute to a stabilization of the ice sheet. Nevertheless, the mass balance of BWF compared to the control run is negative, since the ice volume is reduced by $1232 \, \mathrm{km^3}$ (–7.2 %.). The overall volume loss amounts to $868 \, \mathrm{km^3}$ (–5.1 %).
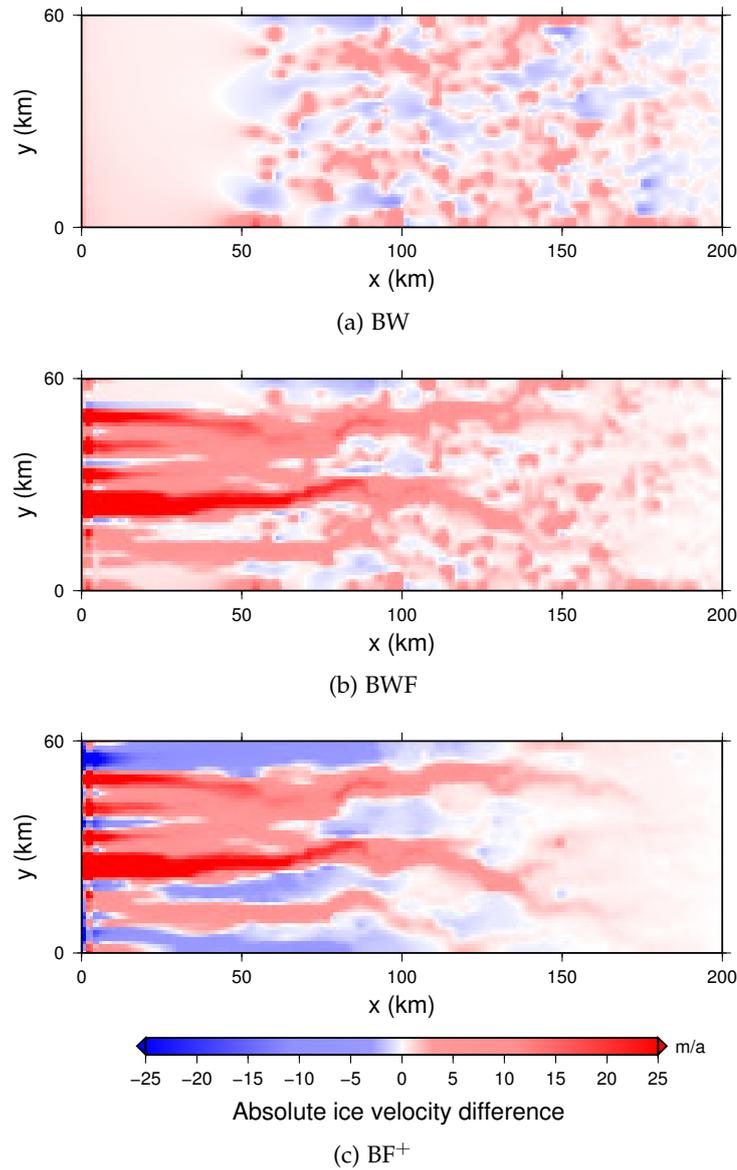
Figure 44: Absolute ice velocity variations of (a) BW, (b) BWF and (c) BF$^+$ compared to the control run (CR). Values are truncated at $\pm 25\,\mathrm{m\,a^{-1}}$.

In *BF* only 54 % of the melt water reaches the model margin, thus the effect of the flux-sliding coupling is relatively small and the ice volume solely decreases by 279 km^3 (–1.6 %). In *BF*$^+$ the ice velocity field shows the influence of the basal water fluxes (Fig. 44c) just as *BWF*. However, since this approach is not capable of storing melt water, the impact of the subglacial lakes on ice dynamics is missing. As a consequence the ice volume diminishes for the amount of 777 km^3 (–4.6 %) only.

6.5 SUMMARY

The introduced balanced water layer concept for subglacial hydrology takes a different approach than previous balance flux schemes (e.g., Budd and Warner,

	V_{ice} (km^3)	ΔV_{ice} (%)	V_{water} (km^3)
CR	17 001		0
BW	16 443	−3.3	372
BWF	15 769	−7.2	364
BF	16 722	−1.6	0
BF$^+$	16 224	−4.6	0

Table 4: Ice volume, change of ice volume compared to the control run (CR) and stored subglacial water volume for all experiments.

1996). It yields a mass conserving balance flux on any topography and is able to accumulate water in subglacial hollows where subglacial lakes can develop. The balanced water layer scheme is self-contained and can be coupled to any ice flow model, operating in Shallow Ice, Shallow Shelf or Higher Order Approximation on numerical Arakawa A- or C-grids. The water layer thickness modifies the geometry by lifting the ice base, while water fluxes can be parameterized to increase the basal ice velocities. Above subglacial lakes the basal shear stress of the ice vanishes completely.

Coupling this new hydrology concept to the ice model RIMBAY reveals the large impact of these interactions on the mass balance of a synthetic ice sheet. Particularly, the predominance of ice loss through water flow induced ice streams against the stabilizing influence of less hydrologically active areas leads to a significantly negative ice mass balance. In combination with the effect of subglacial lake surfaces, which locally cause an increased ice flow, the total ice volume decreases by −7.2 %. In comparison to the direct mass loss caused by basal melting, the indirect contributions of the basal water fluxes and water accumulations to the overall mass balance of the ice sheet are large. The established balance flux schemes quantify these effects only partially as their ability to store subglacial water is lacking. Consequently, the new hydrology approach, providing the dynamic generation of subglacial lakes and the self-organization of subglacial water drainage systems, combined with a flux-friction coupling significantly improves the modeled dynamics of glacial systems.

7

FINAL CONCLUSION AND OUTLOOK

The Antarctic subglacial environment is hidden beneath a kilometers-thick layer of ice and is one of the Earth's most unexplored regions. However, it plays a key role regarding the comprehension and prediction of ice sheet dynamics. Water at the ice-bedrock interface tends to lubricate the base of the ice sheet and thus leads to increased ice sliding rates of ice streams and outlet glaciers. These control the mass export of the Antarctic Ice Sheet and thus its contribution to global sea level rise which is of particular interest against the background of a warming climate. The objective of this thesis is the investigation of this subglacial hydrological environment and its interactions with ice flow dynamics.

This chapter summarizes the key findings of the Chapters 4, 5 and 6 and discusses their main implications, regarding the objectives of this thesis, listed in Sec. 1.2. The brief outlook finally describes potential subsequent studies and relevant future research questions.

7.1 CONCLUSION

This thesis aims for a better understanding of distribution and nature of water flow at the bed of the Antarctic Ice Sheet (AIS) and the interactions between subglacial hydrological environment and ice flow dynamics. Within this thesis the *Revised Ice Model Based on Frank Pattyn* (RIMBAY) has been successfully enhanced by a subglacial hydrology module. It provides the modeling of positions and extents of subglacial lakes and the simulation of basal melt water balance fluxes, following established concepts. In addition, a new hydrological approach has been developed and implemented, allowing the dynamic generation of subglacial lakes and covering the spatial and temporal variability of basal water drainage systems.[1] Thus, valuable insights into the distribution of Antarctic subglacial lakes and their drainage networks are obtained. Furthermore, the revealed dynamic interactions between subglacial hydrology and ice flow dynamics emphasize the importance of subglacial hydrological processes with respect to ice modeling. The new hydrological concept has the potential for better predictions of the mass export of large ice sheets under the influence of climate warming and thus their contribution to future global sea level rise.

---

[1] Co-authorship in Thoma et al. (2014), due to the implementation of the basal hydrology module in RIMBAY.

The main findings of the research Chapters 4, 5 and 6 are already summarized in their last sections. In the following, the key objectives of the above chapters are presented in a condensed form by answering the research questions (Sec. 1.2):

Chapter 4: **To which extent are subglacial lakes covering the base of the Antarctic Ice Sheet?** The distribution of Antarctic subglacial lakes has been modeled, using RIMBAY. The comparison of the model results with locations and extents of known subglacial lakes (Wright and Siegert, 2012) shows a good agreement. The validation of model predictions by the selective interpretation of radar profiles from radio-echo sounding (RES) flight campaigns of the Alfred Wegener Institute (AWI) in Dronning Maud Land (DML) reveals 31 locations of so far uncharted basal water surface and thus so far unknown subglacial lakes. Based on the above findings, the total number of subglacial lakes existing beneath the AIS is estimated to about 1 300±300. Their summarized surface area is assessed to cover about 77 000±18 000 km^2 (0.64±0.15%) of the Antarctic ice-bed interface. These findings indicate, that currently about 30% of the Antarctic subglacial lakes and about 65 % of the estimated total lake-covered area are discovered.

What are the drainage patterns of melt water flow beneath the Antarctic Ice Sheet on a continental scale? The water flow beneath the AIS has been modeled with RIMBAY using the balance flux concept. The basal water flow has characteristics very similar to observable surface rivers, showing angular, distributary, dendritic and parallel flow patterns. A widespread hydrological network is found to establish hydrological connections between subglacial lakes as well as from subglacial lakes towards the ocean within distinct catchment areas. The respective water sheds mainly follow observed positions of ice divides. The simulated flow of basal water underneath the AIS focuses towards the grounding line where strong spatial correlations between areas of enhanced water flow and observed locations of ice streams are revealed. About 23% of the total Antarctic subglacial water catchment area are found to drain into the ocean at only four particular spots: underneath the Byrd Glacier, the Recovery Ice Stream, the Slessor Glacier and the confluent Academy Glacier and Foundation Ice Stream.

Chapter 5: **What controls the spatial and temporal variability of the Ross Ice Streams at the Siple Coast?** Literature research showed, that seismic explorations detected a widely spread and meters thick basal layer of unconsolidated sediments beneath the ice sheet at the Siple Coast (e.g., Alley et al., 1986), creating the precondition for high basal sliding rates by sediment deformation (MacAyeal, 1989). Engelhardt and Kamb (1998) confirmed this hypothesis by measuring basal sliding velocities through a borehole which are found within 83 to 100% of the surface velocities. Radar investigations found a wet bed inside the confines of the Ross Ice Streams and a dry bed outside (e.g., Bentley

et al., 1998). This was approved by observations at the bottom of boreholes (e.g. Engelhardt et al., 1990) and seismic explorations (e.g., Blankenship et al., 1987). Additionally, the basal water pressure in boreholes was measured to be almost equal to the ice pressure (e.g., Kamb, 2001). In summary, it is concluded that the spatial and temporal variability of the ice streams at the Siple Coast is caused by variable basal melt water pathways: Basal water flow within a till layer at low effective pressure (ice minus water pressure) belongs to the distributed flow regimes, which are known to enhance the basal sliding of ice. Due to the smooth bedrock, the water pathways are assessed to be highly sensitive to small ice thickness perturbations and thus basal pressure-condition changes, explaining the observed variability of the Ross Ice Streams in the past. Own analyses and interpretations of ICESat (Pritchard et al., 2012) and recent CryoSat-2 (Helm, in prep.) ice surface elevation change rates explicitly confirms this conclusion and additionally reveal a slightly positive mass balance of the Siple Coast region, estimated to a growth of $52\pm57\,\mathrm{Gt\,a^{-1}}$.

Can modeled basal drainage patterns explain the current configuration of the Ross Ice Streams? Based on the above findings, the water flow beneath the Ross Ice Streams has been modeled with RIMBAY using the balance flux concept. All current ice stream outlines are found to be clearly associated with areas of enhanced water flow. Furthermore, the ice velocities of the ice streams are found to be related to the water catchment area sizes draining underneath.

Which potential impact have satellite-observed surface changes on the evolution of drainage pathways and what might be the implications for future ice stream dynamics? Applying satellite-observed present-day surface elevation changes to the present-day ice sheet configuration for 200 years allows an estimation of future basal drainage routes. According to this simulations, a major hydraulic tributary of the Kamb and Whillans Ice Stream is estimated to be redirected underneath the Bindschadler Ice Stream within the next 200 years. Accordingly, the water catchment area feeding underneath the Bindschadler Ice Stream is estimated to grow by about 50% while the lower part of the stagnated Kamb Ice Stream becomes increasingly separated from the upper hydraulic tributaries of the Siple Coast. This might be a continuation of the subglacial hydraulic processes which caused the past stagnation of the Kamb Ice Stream. Furthermore, this might also lead to a future increase of the ice velocities within the Bindschadlers Ice Stream and an increased ice drainage of the corresponding hinterland.[2]

Chapter 6: **How much do interactions of ice dynamics and subglacial hydrology affect the mass balance of an ice sheet?** This question is addressed, by the dynamic coupling of the hydrology and ice module in RIMBAY and an application to a synthetic model domain. Various complex feedback mechanisms between ice sheet geometry, subglacial lakes, basal melting, basal water

---

2 This chapter forms the basis for a manuscript that is going to be submitted to *Geophysical Research Letters* (Goeller et al., in prep.).

flow and shear stress at the base of an ice sheet reveal the performance of the new hydrology concept. It is demonstrated, that the ice loss through water flow induced ice streams dominates over the stabilizing influence of less hydrologically active areas. Subglacial lake surfaces reduce basal drag, causing increased ice velocities and thus leading to a further negative ice mass balance. At full complexity of the hydrology-ice coupling, the total ice volume of the investigated synthetic ice sheet decreases by –7.2%. In comparison, it is shown that the balance flux scheme (Budd and Warner, 1996) covers the above effects only partially because its ability to store subglacial water is lacking. It is concluded, that indirect contributions of basal water flow and water accumulations by interactions to the ice dynamics to the overall mass balance of the ice sheet are large even though the direct mass loss by basal melting might be small. Consequently, the new hydrology approach, providing the dynamic generation of subglacial lakes and the self-organization of subglacial water drainage systems, combined with a flux-friction coupling significantly improves the modeled dynamics of glacial systems.[3]

7.2 OUTLOOK

The research results presented in this thesis successfully address all proposed research questions. However, they also encourage further investigations in the following areas:

- In Chapter 4 the distribution of Antarctic subglacial lakes is modeled. The subsequent validation by the analysis of RES radar-profiles from DML revealed that about 13% of the modeled subglacial lakes could be identified by basal lake-surface reflections. In future studies, this predictive power might be significantly increased by combining the applied approach with other methods regarding the analysis of bedrock roughness (Steinhage et al., in prep.) and basal radar reflection strength along flight lines (Kasper et al., in prep.). Thus, the precision of estimates about the total Antarctic subglacial lakes coverage could be improved.

- In Chapter 5 future basal water pathways beneath the Ross Ice Streams are estimated by applying satellite-derived surface elevation change rates to the present day ice sheet configuration. Ice streams in other Antarctic regions are assumed to be controlled by basal hydrology, too. Consequently, the application of this method to other Antarctic regions would yield profound insights into the local variability of basal water flow and thus ice flow and mass export under the influence of climate warming and changing ice sheet geometries.

- Chapter 6 shows the potential of coupling subglacial hydrology and ice flow modeling. In subsequent studies, this approach can be applied to,

---

3 This chapter is based on Goeller et al. (2013), which has been published in *The Cryosphere*.

e.g., the Siple Coast. This would allow to make more precise statements about the future dynamics of the Ross Ice Streams because the feedback of subglacial hydrology towards the ice flow is included, which is not the case in the prognostic modeling approach in Chap. 5. In this way, assessments of the future mass balance would gain precision.

Although the theory of Robin (1955) about water at the base of glaciers and ice sheets has been confirmed by numerous remote-sensing and in-situ observations, details about the characteristics of basal water flows and their particular impact on the overlying ice dynamics are still unclear. Enhanced observation methods are necessary to confirm and improve current theoretical descriptions of subglacial water flow regimes and thus lead to a more comprehensive understanding of this utmost important processes for ice sheet dynamics and climate research.

Abyzov, S., Mitskevich, I., Poglazova, M., Barkov, N., Lipenkov, V. Y., Bobin, N., Koudryashov, B., Pashkevich, V., and Ivanov, M.: Microflora in the basal strata at Antarctic ice core above the Vostok lake, Advances in Space Research, 28, 701–706, doi:10.1016/S0273-1177(01)00318-0, 2001.

Alley, R.: Towards a hydrological model for computerized ice-sheet simulations, Hydrological Processes, 10, 649–660, doi:10.1002/(SICI)1099-1085(199604)10:4<649::AID-HYP397>3.0.CO;2-1, 1996.

Alley, R., Blankenship, D., Bentley, C., and Rooney, S.: Deformation of till beneath ice stream B, West Antarctica, doi:10.1038/322057a0, 1986.

Alley, R., Blankenship, D., Bentley, C., and Rooney, S.: Till beneath ice stream B: 3. Till deformation: evidence and implications, Journal of Geophysical Research: Solid Earth (1978–2012), 92, 8921–8929, doi:10.1029/JB092iB09p08921, 1987.

Alley, R., Blankenship, D., Rooney, S., and Bentley, C.: Sedimentation beneath ice shelves – the view from ice stream B, Marine Geology, 85, 101–120, doi:10.1016/0025-3227(89)90150-3, 1989.

Anandakrishnan, S. and Alley, R. B.: Stagnation of Ice Stream C, West Antarctica by water piracy, Geophysical Research Letters, 24, 265–268, doi:10.1029/96GL04016, 1997.

Anandakrishnan, S., Alley, R., Jacobel, R., and Conway, H.: The flow regime of Ice Stream C and hypotheses concerning its recent stagnation, The West Antarctic Ice Sheet: Behavior and Environment, pp. 283–296, doi:10.1029/AR077p0283, 2001.

Anandakrishnan, S., Catania, G. A., Alley, R. B., and Horgan, H. J.: Discovery of till deposition at the grounding line of Whillans Ice Stream, Science, 315, 1835–1838, doi:10.1126/science.1138393, 2007.

Anderson, R. S. and Anderson, S. P.: Geomorphology: the mechanics and chemistry of landscapes, Cambridge University Press, 2010.

Arakawa, A. and Lamb, V. R.: Methods of computational physics, vol. 17, Academic Press, 1977.

Arthern, R. J., Winebrenner, D. P., and Vaughan, D. G.: Antarctic snow accumulation mapped using polarization of 4.3-cm wavelength microwave emission, Journal of Geophysical Research: Atmospheres (1984–2012), 111, doi:10.1029/2004JD005667, 2006.

Aschwanden, A. and Blatter, H.: Mathematical modeling and numerical simulation of polythermal glaciers, Journal of Geophysical Research: Earth Surface, 114, doi:10.1029/2008JF001028, 2009.

Augustin, L., Barbante, C., Barnes, P. R., Barnola, J. M., Bigler, M., Castellano, E., Cattani, O., Chappellaz, J., Dahl-Jensen, D., Delmonte, B., et al.: Eight glacial cycles from an Antarctic ice core, Nature, 429, 623–628, doi:10.1038/nature02599, 2004.

Bamber, J. L., Riva, R. E., Vermeersen, B. L., and LeBrocq, A. M.: Reassessment of the potential sea-level rise from a collapse of the West Antarctic Ice Sheet, Science, 324, 901–903, doi:10.1126/science.1169335, 2009.

Beckmann, A. and Goosse, H.: A parameterization of ice shelf–ocean interaction for climate models, Ocean modelling, 5, 157–170, doi:10.1016/S1463-5003(02)00019-7, 2003.

Beem, L. H., Jezek, K. C., and Van der Veen, C.: Basal melt rates beneath Whillans Ice Stream, West Antarctica, Journal of Glaciology, 56, 647–654, doi:10.3189/002214310793146241, 2010.

Bell, R. E., Studinger, M., Shuman, C. A., Fahnestock, M. A., and Joughin, I.: Large subglacial lakes in East Antarctica at the onset of fast-flowing ice streams, Nature, 445, 904–907, doi:10.1038/nature05554, 2007.

Bell, R. E., Ferraccioli, F., Creyts, T. T., Braaten, D., Corr, H., Das, I., Damaske, D., Frearson, N., Jordan, T., Rose, K., Studinger, M., and Wolovick, M.: Widespread persistent thickening of the East Antarctic Ice Sheet by freezing from the base, Science, 331, 1592–1595, doi:10.1126/science.1200109, 2011.

Bennett, M. R.: Ice streams as the arteries of an ice sheet: their mechanics, stability and significance, Earth-Science Reviews, 61, 309–339, doi:10.1016/S0012-8252(02)00130-7, 2003.

Bentley, C., Lord, N., and Liu, C.: Radar reflections reveal a wet bed beneath stagnant Ice Stream C and a frozen bed beneath ridge BC, West Antarctica, Journal of Glaciology, 44, 149–156, 1998.

Bindschadler, R. A., Nowicki, S., Abe-Ouchi, A., Aschwanden, A., Choi, H., Fastook, J., Granzow, G., Greve, R., Gutowski, G., Herzfeld, U., et al.: Ice-sheet model sensitivities to environmental forcing and their use in projecting future sea-level (The SeaRISE Project), Journal of Glaciology, 59, 195–224, doi:10.3189/2013JoG12J125, 2013.

Blankenship, D., Bentley, C., Rooney, S., and Alley, R. B.: Till beneath Ice Stream B: 1. Properties derived from seismic travel times, Journal of Geophysical Research: Solid Earth (1978–2012), 92, 8903–8911, doi:10.1029/JB092iB09p08903, 1987.

Blankenship, D., Morse, D., Finn, C., Bell, R., Peters, M., Kempf, S., Hodge, S., Studinger, M., Behrendt, J., and Brozena, J.: Geologic controls on the initiation of rapid basal motion for West Antarctic ice streams: A geophysical perspective including new airborne radar sounding and laser altimetry results, The West Antarctic Ice Sheet: Behavior and Environment, pp. 105–121, doi:10.1029/AR077p0105, 2001.

Blatter, H.: Velocity and stress fields in grounded glaciers: a simple algorithm for including deviatoric stress gradients, Journal of Glaciology, 41, 333–344, 1995.

Bohleber, P., Wagner, N., and Eisen, O.: Permittivity of ice at radio frequencies: Part II. Artificial and natural polycrystalline ice, Cold Regions Science and Technology, 83, 13–19, doi:10.1016/j.coldregions.2012.05.010, 2012.

Bougamont, M., Price, S., Christoffersen, P., and Payne, A.: Dynamic patterns of ice stream flow in a 3-D higher-order ice sheet model with plastic bed and simplified hydrology, Journal of Geophysical Research: Earth Surface (2003–2012), 116, doi:10.1029/2011JF002025, 2011.

British Antarctic Survey: Antarctica Overview Map., http://lima.usgs.gov/documents/LIMA_overview_map.pdf, accessed: 2013-12-16, 2007.

British Antarctic Survey: The Exploration of Subglacial Lake Ellsworth., http://www.antarctica.ac.uk/press/images/ellsworth_graphic.jpg, accessed: 2013-12-16, 2008.

Budd, W. and Jenssen, D.: Numerical Modelling of the Large-Scale Basal Water Flux under the West Antarctic Ice Sheet, in: Dynamics of the West Antarctic Ice Sheet, edited by Veen, C. and Oerlemans, J., vol. 4 of *Glaciology and Quaternary Geology*, pp. 293–320, Springer Netherlands, 1987.

Budd, W. F. and Warner, R. C.: A computer scheme for rapid calculations of balance-flux distributions, Annals of Glaciology, 23, 21–27, 1996.

Bueler, E., Brown, J., and Lingle, C.: Exact solutions to the thermomechanically coupled shallow-ice approximation: effective tools for verification, Journal of Glaciology, 53, 499–516, doi:10.3189/002214307783258396, 2007.

Carter, S. and Fricker, H.: The supply of subglacial meltwater to the grounding line of the Siple Coast, West Antarctica, Annals of Glaciology, 53, 267–280, doi:10.3189/2012AoG60A119, 2012.

Carter, S. P., Blankenship, D. D., Peters, M. E., Young, D. A., Holt, J. W., and Morse, D. L.: Radar-based subglacial lake classification in Antarctica, Geochemistry, Geophysics, Geosystems, 8, doi:10.1029/2006GC001408, 2007.

Carter, S. P., Blankenship, D. D., Young, D. A., and Holt, J. W.: Using radar-sounding data to identify the distribution and sources of subglacial water:

application to Dome C, East Antarctica, Journal of Glaciology, 55, 1025–1040, doi:10.3189/002214309790794931, 2009a.

Carter, S. P., Blankenship, D. D., Young, D. A., Peters, M. E., Holt, J. W., and Siegert, M. J.: Dynamic distributed drainage implied by the flow evolution of the 1996–1998 Adventure Trench subglacial lake discharge, Earth and Planetary Science Letters, 283, 24–37, doi:10.1016/j.epsl.2009.03.019, 2009b.

Catania, G., Scambos, T., Conway, H., and Raymond, C.: Sequential stagnation of Kamb Ice Stream, West Antarctica, Geophysical Research Letters, 33, doi:10.1029/2006GL026430, 2006.

Catania, G., Hulbe, C., Conway, H., Scambos, T., and Raymond, C.: Variability in the mass flux of the Ross Ice Streams, West Antarctica, over the last millennium, Journal of Glaciology, 58, 741–752, doi:10.3189/2012JoG11J219, 2012.

Christianson, K., Jacobel, R. W., Horgan, H. J., Anandakrishnan, S., and Alley, R. B.: Subglacial Lake Whillans – Ice-penetrating radar and GPS observations of a shallow active reservoir beneath a West Antarctic ice stream, Earth and Planetary Science Letters, 331, 237–245, doi:10.1016/j.epsl.2012.03.013, 2012.

Clarke, G. K.: Subglacial processes, Annual Review of Earth and Planetary Sciences, 33, 247–276, doi:10.1146/annurev.earth.33.092203.122621, 2005.

Comiso, J. C.: Variability and trends in Antarctic surface temperatures from in situ and satellite infrared measurements, Journal of Climate, 13, 1674–1696, doi:10.1175/1520-0442(2000)013<1674:VATIAS>2.0.CO;2, 2000.

Conway, H., Catania, G., Raymond, C., Gades, A., Scambos, T., and Engelhardt, H.: Switch of flow direction in an Antarctic ice stream, Nature, 419, 465–467, doi:10.1038/nature01081, 2002.

Cuffey, K. M. and Paterson, W. S. B.: The Physics of Glaciers, Elsevier, Amsterdam, 4 edn., 2010.

Depoorter, M., Bamber, J., Griggs, J., Lenaerts, J., Ligtenberg, S., van den Broeke, M., and Moholdt, G.: Calving fluxes and basal melt rates of Antarctic ice shelves, Nature, 502, 89–92, doi:10.1038/nature12567, 2013.

Determann, J., Thoma, M., Grosfeld, K., and Massmann, S.: Impact of ice-shelf basal melting on inland ice-sheet thickness: a model study, Annals of Glaciology, 53, 129–135, doi:10.3189/2012AoG60A170, 2012.

Dowdeswell, J. A. and Siegert, M. J.: The physiography of modern Antarctic subglacial lakes, Global and Planetary Change, 35, 221–236, doi:10.1016/S0921-8181(02)00128-5, 2003.

Duxbury, N., Zotikov, I., Nealson, K., Romanovsky, V., and Carsey, F.: A numerical model for an alternative origin of Lake Vostok and its exobiological implications for Mars, Journal of Geophysical Research, 106, 1453–1462, doi:10.1029/2000JE001254, 2001.

Eisen, O., Hofstede, C., Miller, H., Kristoffersen, Y., Blenkner, R., Lambrecht, A., and Mayer, C.: A New Approach for Exploring Ice Sheets and Sub-Ice Geology, Eos, Transactions American Geophysical Union, 91, 429–430, doi:10.1029/2010EO460001, 2010.

Engelhardt, H.: Ice temperature and high geothermal flux at Siple Dome, West Antarctica, from borehole measurements, Journal of Glaciology, 50, 251–256, doi:10.3189/172756504781830105, 2004.

Engelhardt, H. and Kamb, B.: Basal sliding of ice stream B, West Antarctica, Journal of Glaciology, 44, 223–230, 1998.

Engelhardt, H., Humphrey, N., Kamb, B., and Fahnestock, M.: Physical conditions at the base of a fast moving Antarctic ice stream, Science, 248, 57–59, doi:10.1126/science.248.4951.57, 1990.

Filina, I. Y., Blankenship, D. D., Thoma, M., Lukin, V. V., Masolov, V. N., and Sen, M. K.: New 3D bathymetry and sediment distribution in Lake Vostok: Implication for pre-glacial origin and numerical modeling of the internal processes within the lake, Earth and Planetary Science Letters, 276, 106–114, doi:10.1016/j.epsl.2008.09.012, 2008.

Fischer, H., Severinghaus, J., Brook, E., Wolff, E., Albert, M., Alemany, O., Arthern, R., Bentley, C., Blankenship, D., Chappellaz, J., et al.: Where to find 1.5 million yr old ice for the IPICS "Oldest Ice" ice core, Climate of the Past Discussions, 9, 2771–2815, doi:10.5194/cpd-9-2771-2013, 2013.

Flowers, G. E., Björnsson, H., Pálsson, F., and Clarke, G. K.: A coupled sheet-conduit mechanism for jökulhlaup propagation, Geophysical Research Letters, 31, doi:10.1029/2003GL019088, 2004.

Fountain, A. G. and Walder, J. S.: Water flow through temperate glaciers, Reviews of Geophysics, 36, 299–328, doi:10.1029/97RG03579, 1998.

Fowler, A.: A sliding law for glaciers of constant viscosity in the presence of subglacial cavitation, Proceedings of the Royal Society of London. A. Mathematical and Physical Sciences, 407, 147–170, doi:10.1098/rspa.1986.0090, 1986.

Fowler, A.: Weertman, Lliboutry and the development of sliding theory, Journal of Glaciology, 56, 965–972, doi:10.3189/002214311796406112, 2010.

Fretwell, P., Pritchard, H., Vaughan, D., Bamber, J., Barrand, N., Bell, R., Bianchi, C., Bingham, R. G., Blankenship, D., Casassa, G., Catania, G., Callens, D., Conway, H., Cook, A., Corr, H., Damaske, D., Damm, V., Ferraccioli, F., Forsberg, R., Fujita, S., Gim, Y., Gogineni, P., Griggs, J., Hindmarsh,

R., Holmlund, P., Holt, J., Jacobel, R., Jenkins, A., Jokat, W., Jordan, T., King, E., Kohler, J., Krabill, W., Riger-Kusk, M., Langley, K., Leitchenkov, G., Leuschen, C., Luyendyk, B., Matsuoka, K., Mouginot, J., Nitsche, F., Nogi, Y., Nost, O., Popov, S., Rignot, E., Rippin, D., Rivera, A., Roberts, J., Ross, N., Siegert, M., Smith, A., Steinhage, D., Studinger, M., Sun, B., Tinto, B., Welch, B., Wilson, D., Young, D., Xiangbin, C., and Zirizzotti, A.: Bedmap2: improved ice bed, surface and thickness datasets for Antarctica, The Cryosphere, 7, 375–393, doi:10.5194/tc-7-375-2013, 2013.

Fricker, H. A. and Scambos, T.: Connected subglacial lake activity on lower Mercer and Whillans Ice Streams, West Antarctica, 2003–2008, Journal of Glaciology, 55, 303–315, doi:10.3189/002214309788608813, 2009.

Fricker, H. A., Scambos, T., Bindschadler, R., and Padman, L.: An active sub-glacial water system in west Antarctica mapped from space, Science, 315, 1544–1548, doi:10.1126/science.1136897, 2007.

Fricker, H. A., Scambos, T., Carter, S., Davis, C., Haran, T., and Joughin, I.: Synthesizing multiple remote-sensing techniques for sub-glacial hydrologic mapping: application to a lake system beneath MacAyeal Ice Stream, West Antarctica, Journal of Glaciology, 56, 187–199, doi:10.3189/002214310791968557, 2010.

Gagliardini, O. and Zwinger, T.: The ISMIP-HOM benchmark experiments performed using the Finite-Element code Elmer, The Cryosphere, 2, 67–76, doi:10.5194/tc-2-67-2008, 2008.

Gagliardini, O., Cohen, D., Råback, P., and Zwinger, T.: Finite-element mod-eling of subglacial cavities and related friction law, Journal of Geophysical Research: Earth Surface (2003–2012), 112, doi:10.1029/2006JF000576, 2007.

Gillet-Chaulet, F., Gagliardini, O., Seddik, H., Nodet, M., Durand, G., Ritz, C., Zwinger, T., Greve, R., and Vaughan, D. G.: Greenland ice sheet contribution to sea-level rise from a new-generation ice-sheet model, The Cryosphere, 6, 1561–1576, doi:10.5194/tc-6-1561-2012, 2012.

Goddard Space Flight Center: Components of the Cryosphere., http://svs.gsfc.nasa.gov/goto?3885, accessed: 2013-12-16, 2011.

Goeller, S., Thoma, M., Grosfeld, K., and Miller, H.: A balanced water layer concept for subglacial hydrology in large-scale ice sheet models, The Cryosphere, 7, 1095–1106, doi:10.5194/tc-7-1095-2013, 2013.

Goeller, S., Thoma, M., Grosfeld, K., Helm, V., and Miller, H.: Evolution of subglacial hydrology and ice dynamics at the Siple Coast, Antarctica, Geo-physical Research Letters, in prep.

Gray, L., Joughin, I., Tulaczyk, S., Spikes, V. B., Bindschadler, R., and Jezek, K.: Evidence for subglacial water transport in the West Antarctic Ice Sheet

through three-dimensional satellite radar interferometry, Geophysical Research Letters, 32, doi:10.1029/2004GL021387, 2005.

Greve, R.: A continuum–mechanical formulation for shallow polythermal ice sheets, Philosophical Transactions of the Royal Society of London. Series A: Mathematical, Physical and Engineering Sciences, 355, 921–974, doi:10.1098/rsta.1997.0050 , 1997a.

Greve, R.: Application of a polythermal three-dimensional ice sheet model to the Greenland ice sheet: response to steady-state and transient climate scenarios, Journal of Climate, 10, 901–918, doi:10.1175/1520-0442(1997)010<0901:AOAPTD>2.0.CO;2, 1997b.

Greve, R. and Blatter, H.: Dynamics of ice sheets and glaciers., Springer Verlag, 2009.

Grosfeld, K., Gerdes, R., and Determann, J.: Thermohaline circulation and interaction between ice shelf cavities and the adjacent open ocean, Journal of Geophysical Research: Oceans (1978–2012), 102, 15595–15610, doi:10.1029/97JC00891, 1997.

Gudmundsson, G. H., Krug, J., Durand, G., Favier, L., and Gagliardini, O.: The stability of grounding lines on retrograde slopes, The Cryosphere, 6, 1497–1505, doi:10.5194/tc-6-1497-2012, 2012.

Hellmer, H. H., Kauker, F., Timmermann, R., Determann, J., and Rae, J.: Twenty-first-century warming of a large Antarctic ice-shelf cavity by a redirected coastal current, Nature, 485, 225–228, doi:10.1038/nature11064, 2012.

Helm, V.: Elevation and elevation change of Greenland and Antarctica derived from CryoSat-2, Nature, in prep.

Helm, V., Humbert, A., and Miller, H.: Elevation and elevation change of Greenland and Antarctica derived from CryoSat-2, The Cryosphere Discussions, 8, 1673–1721, doi:10.5194/tcd-8-1673-2014, 2014.

Hewitt, I. J.: Modelling distributed and channelized subglacial drainage: the spacing of channels, Journal of Glaciology, 57, 302–314, doi:10.3189/002214311796405951, 2011.

Hewitt, I. J., Schoof, C., and Werder, M. A.: Flotation and free surface flow in a model for subglacial drainage. Part 2. Channel flow, Journal of Fluid Mechanics, 702, 157–187, doi:10.1017/jfm.2012.166, 2012.

Hindmarsh, R.: A numerical comparison of approximations to the Stokes equations used in ice sheet and glacier modeling, Journal of Geophysical Research, 109, F01012, doi:10.1029/2003JF000065, 2004.

Hooke, R.: Flow law for polycrystalline ice in glaciers: Comparison of theoretical predictions, laboratory data, and field measurements, Reviews of Geophysics, 19, 664–672, doi:10.1029/RG019i004p00664, 1981.

Horgan, H. J., Anandakrishnan, S., Jacobel, R. W., Christianson, K., Alley, R. B., Heeszel, D. S., Picotti, S., and Walter, J. I.: Subglacial Lake Whillans – Seismic observations of a shallow active reservoir beneath a West Antarctic ice stream, Earth and Planetary Science Letters, 331, 201–209, doi:10.1016/j.epsl.2012.02.023, 2012.

Humbert, A., Kleiner, T., Mohrholz, C.-O., Oelke, C., Greve, R., and Lange, M. A.: A comparative modeling study of the Brunt Ice Shelf/Stancomb-Wills Ice Tongue system, East Antarctica, Journal of Glaciology, 55, 53–65, doi:10.3189/002214309788608949, 2009.

Hutter, K.: Theoretical glaciology: material science of ice and the mechanics of glaciers and ice sheets, Reidel, 1983.

Huybrechts, P., Payne, T., EISMINT, I., et al.: The EISMINT benchmarks for testing ice-sheet models, Annals of Glaciology, 23, 1–12, doi:2115/34649, 1996.

IPCC: The Physical Science Basis. Contribution of Working Group I to the Fifth Assessment Report of the Intergovernmental Panel on Climate Change, in: Climate Change 2013, edited by Joussaume, S., Penner, J., and Tangang, F., pp. 1–2216, Cambridge University Press, Cambridge, United Kingdom and New York, NY, USA, 2013.

Jacobel, R. W., Scambos, T. A., Raymond, C. F., and Gades, A. M.: Changes in the configuration of ice stream flow from the West Antarctic Ice Sheet, Journal of Geophysical Research: Solid Earth (1978–2012), 101, 5499–5504, doi:10.1029/95JB03735, 1996.

Jacobel, R. W., Welch, B. C., Osterhouse, D., Pettersson, R., and MacGregor, J. A.: Spatial variation of radar-derived basal conditions on Kamb Ice Stream, West Antarctica, Annals of Glaciology, 50, 10, doi:10.3189/172756409789097504, 2009.

Johari, G. and Charette, P.: The permittivity and attenuation in polycrystalline and single-crystal ice Ih at 35 and 60 MHz, Journal of Glaciology, 14, 293–303, 1975.

Joughin, I. and Tulaczyk, S.: Positive mass balance of the Ross Ice Streams, West Antarctica, Science, 295, 476–480, doi:10.1126/science.1066875, 2002.

Joughin, I., Tulaczyk, S., Bindschadler, R., and Price, S. F.: Changes in West Antarctic ice stream velocities: Observation and analysis, Journal of Geophysical Research: Solid Earth, 107, 1–22, doi:10.1029/2001JB001029, 2002.

Joughin, I., Tulaczyk, S., MacAyeal, D. R., and Engelhardt, H.: Melting and freezing beneath the Ross Ice Streams, Antarctica, Journal of Glaciology, 50, 96–108, doi:10.3189/172756504781830295, 2004.

Joughin, I. R., Tulaczyk, S., and Engelhardt, H. F.: Basal melt beneath Whillans Ice Stream and Ice Streams A and C, West Antarctica, Annals of Glaciology, 36, 257–262, doi:10.3189/172756403781816130, 2003.

Kamb, B.: Basal zone of the West Antarctic ice streams and its role in lubrication of their rapid motion, Antarctic Research Series, 77, 157–199, doi:10.1029/AR077p0157, 2001.

Kapitsa, A., Ridley, J., Robin, G. d. Q., Siegert, M., and Zotikov, I.: A large deep freshwater lake beneath the ice of central East Antarctica, Nature, 381, 684–686, doi:10.1038/381684a0, 1996.

Kasper, D., Steinhage, D., and Humbert, A.: Determining a wet base of the ice sheet in East Antarctica by means of radio-echo sounding, in prep.

Kwok, R., Siegert, M. J., and Carsey, F. D.: Ice motion over Lake Vostok, Antarctica: constraints on inferences regarding the accreted ice, Journal of Glaciology, 46, 689–694, doi:10.3189/172756500781832710, 2000.

Langley, K., Kohler, J., Matsuoka, K., Sinisalo, A., Scambos, T., Neumann, T., Muto, A., Winther, J.-G., and Albert, M.: Recovery Lakes, East Antarctica: Radar assessment of sub-glacial water extent, Geophysical Research Letters, 38, doi:10.1029/2010GL046094, 2011.

Larour, E., Seroussi, H., Morlighem, M., and Rignot, E.: Continental scale, high order, high spatial resolution, ice sheet modeling using the Ice Sheet System Model (ISSM), Journal of Geophysical Research: Earth Surface, 117, doi:10.1029/2011JF002140, 2012.

Le Brocq, A. M., Payne, A. J., and Siegert, M. J.: West Antarctic balance calculations: Impact of flux-routing algorithm, smoothing algorithm and topography, Computational Geosciences, 32, 1780–1795, doi:10.1016/j.cageo.2006.05.003, 2006.

Le Brocq, A. M., Payne, A. J., Siegert, M. J., and Alley, R. B.: A subglacial water-flow model for West Antarctica, Journal of Glaciology, 55, 879–888, doi:10.3189/002214309790152564, 2009.

Le Brocq, A. M., Payne, A. J., and Vieli, A.: An improved Antarctic dataset for high resolution numerical ice sheet models (ALBMAP v1), Earth System Science Data, 2, 247–260, doi:10.5194/essdd-3-195-2010, 2010.

Lemieux, J.-F., Price, S. F., Evans, K. J., Knoll, D., Salinger, A. G., Holland, D. M., and Payne, A. J.: Implementation of the Jacobian-free Newton–Krylov method for solving the first-order ice sheet momentum balance, Journal of Computational Physics, 230, 6531–6545, doi:10.1016/j.jcp.2011.04.037, 2011.

Livingstone, S. J., Clark, C. D., Woodward, J., and Kingslake, J.: Potential subglacial lake locations and meltwater drainage pathways beneath the Antarctic and Greenland ice sheets, The Cryosphere, 7, 1721–1740, doi:10.5194/tc-7-1721-2013, 2013.

Lliboutry, L.: General theory of subglacial cavitation and sliding of temperate glaciers, Journal of Glaciology, 7, 21–58, 1968.

Lythe, M. B., Vaughan, D. G., and the BEDMAP Consortium: BEDMAP: A new ice thickness and subglacial topographic model of the Antarctic, Journal of Geophysical Research, 106, 11 335–11 351, doi:10.1029/2000JB900449, 2001.

MacAyeal, D. R.: Large-scale ice flow over a viscous basal sediment: Theory and application to Ice Stream B, Antarctica, Journal of Geophysical Research: Solid Earth, 94, 4071–4087, doi:10.1029/JB094iB04p04071, 1989.

MacAyeal, D. R.: The basal stress distribution of Ice Stream E, Antarctica, inferred by control methods, Journal of Geophysical Research: Solid Earth (1978–2012), 97, 595–603, doi:10.1029/91JB02454, 1992.

Martin, M., Winkelmann, R., Haseloff, M., Albrecht, T., Bueler, E., Khroulev, C., and Levermann, A.: The Potsdam Parallel Ice Sheet Model (PISM-PIK)– Part 2: Dynamic equilibrium simulation of the Antarctic ice sheet, The Cryosphere, 5, 727–740, doi:10.5194/tc-5-727-2011, 2011.

Maule, C. F., Purucker, M. E., Olsen, N., and Mosegaard, K.: Heat flux anomalies in Antarctica revealed by satellite magnetic data, Science, 309, 464–467, doi:10.1126/science.1106888, 2005.

McMillan, M., Corr, H., Shepherd, A., Ridout, A., Laxon, S., and Cullen, R.: Three-dimensional mapping by CryoSat-2 of subglacial lake volume changes, Geophysical Research Letters, doi:10.1002/grl.50689, 2013.

Morland, L.: Thermomechanical balances of ice sheet flows, Geophysical & Astrophysical Fluid Dynamics, 29, 237–266, doi:10.1080/03091928408248191, 1984.

Morland, L.: Unconfined ice-shelf flow, in: Dynamics of the West Antarctic Ice Sheet, pp. 99–116, Springer, doi:10.1007/978-94-009-3745-1_6, 1987.

National Science Foundation: An artist's cross-section of Lake Vostok, the largest known subglacial lake in Antarctica., http://www.nsf.gov/news/news_images.jsp?cntn_id=109587&org=NSF, accessed: 2013-12-16, 2007a.

National Science Foundation: An artist's representation of the aquatic system scientists believe is buried beneath the Antarctic Ice Sheet., http://www.nsf.gov/news/news_images.jsp?cntn_id=109587&org=NSF, accessed: 2013-12-16, 2007b.

Ng, F. and Conway, H.: Fast-flow signature in the stagnated Kamb Ice Stream, West Antarctica, Geology, 32, 481–484, doi:10.1130/G20317.1, 2004.

Nye, J.: Water at the bed of a glacier, IASH Publ. 95 (Symposium at Cambridge 1969 – Hydrology of Glaciers), pp. 477–489, 1973.

Oswald, G. and Robin, G. d. Q.: Lakes beneath the Antarctic ice sheet, Nature, 245, 251–254, doi:10.1038/245251a0, 1973.

Parizek, R., Alley, R. B., and Hulbe, C. L.: Subglacial thermal balance permits ongoing grounding-line retreat along the Siple Coast of West Antarctica, Annals of Glaciology, 36, 251–256, doi:10.3189/172756403781816167, 2003.

Pattyn, F.: Transient glacier response with a higher-order numerical ice-flow model, Journal of Glaciology, 48, 467–477, doi:10.3189/172756502781831278, 2002.

Pattyn, F.: A new three-dimensional higher-order thermomechanical ice sheet model: Basic sensitivity, ice stream development, and ice flow across subglacial lakes, Journal of Geophysical Research, 108, 1–15, doi:10.1029/2002JB002329, 2003.

Pattyn, F.: Comment on the comment by MJ Siegert on "A numerical model for an alternative origin of Lake Vostok and its exobiological implications for Mars" by NS Duxbury et al., Journal of Geophysical Research: Planets (1991–2012), 109, doi:10.1029/2004JE002329, 2004.

Pattyn, F.: Antarctic subglacial conditions inferred from a hybrid ice sheet/ice stream model, Earth and Planetary Science Letters, 295, 451–461, doi:10.1016/j.epsl.2010.04.025, 2010.

Pattyn, F., de Smedt, B., and Souchez, R.: Influence of subglacial Vostok lake on the regional ice dynamics of the Antarctic ice sheet: a model study, Journal of Glaciology, 50, 583–589, doi:10.3189/172756504781829765, 2004.

Pattyn, F., Perichon, L., Aschwanden, A., Breuer, B., de Smedt, B., Gagliardini, O., Gudmundsson, G. H., Hindmarsh, R. C. A., Hubbard, A., Johnson, J. V., Kleiner, T., Konovalov, Y., Martin, C., Payne, A. J., Pollard, D., Price, S., Rückamp, M., Saito, F., Souček, O., Sugiyama, S., and Zwinger, T.: Benchmark experiments for higher-order and full-Stokes ice sheet models (ISMIP-HOM), The Cryosphere, 2, 95–108, doi:10.5194/tc-2-95-2008, 2008.

Pattyn, F., Schoof, C., Perichon, L., Hindmarsh, R. C. A., Bueler, E., de Fleurian, B., Durand, G., Gagliardini, O., Gladstone, R., Goldberg, D., Gudmundsson, G. H., Huybrechts, P., Lee, V., Nick, F. M., Payne, A. J., Pollard, D., Rybak, O., Saito, F., and Vieli, A.: Results of the Marine Ice Sheet Model Intercomparison Project, MISMIP, The Cryosphere, 6, 573–588, doi:10.5194/tc-6-573-2012, 2012.

Pattyn, F., Perichon, L., Durand, G., Favier, L., Gagliardini, O., Hindmarsh, R. C. A., Zwinger, T., Albrecht, T., Cornford, S., Docquier, D., Fürst, J. J., Goldberg, D., Gudmundsson, G. H., Humbert, A., Hutten, M., Huybrechts, P., Jouvet, G., Kleiner, T., Larour, E., Martin, D., Morlighem, M., Payne, A. J., Pollard, D., Rückamp, M., Rybak, O., Seroussi, H., Thoma, M., and Wilkens, N.: Grounding-line migration in plan-view marine ice-sheet models: results

of the ice2sea MISMIP3d intercomparison, Journal of Glaciology, 59, 410–422, doi:10.3189/2013JoG12J129, 2013.

Peters, L., Anandakrishnan, S., Holland, C., Horgan, H., Blankenship, D., and Voigt, D.: Seismic detection of a subglacial lake near the South Pole, Antarctica, Geophysical Research Letters, 35, L23 501, doi:10.1029/2008GL035704, 2008.

Peters, L. E., Anandakrishnan, S., Alley, R. B., Winberry, J. P., Voigt, D. E., Smith, A. M., and Morse, D. L.: Subglacial sediments as a control on the onset and location of two Siple Coast ice streams, West Antarctica, Journal of Geophysical Research: Solid Earth (1978–2012), 111, doi:10.1029/2005JB003766, 2006.

Price, S., Bindschadler, R., Hulbe, C., and Joughin, I.: Post-stagnation behavior in the upstream regions of Ice Stream C, West Antarctica, Journal of Glaciology, 47, 283–294, doi:10.3189/172756501781832232, 2001.

Pritchard, H. D., Arthern, R. J., Vaughan, D. G., and Edwards, L. A.: Extensive dynamic thinning on the margins of the Greenland and Antarctic ice sheets, Nature, 461, 971–975, doi:10.1038/nature08471, 2009.

Pritchard, H. D., Ligtenberg, S., Fricker, H., Vaughan, D., Van den Broeke, M., and Padman, L.: Antarctic ice-sheet loss driven by basal melting of ice shelves, Nature, 484, 502–505, doi:10.1038/nature10968, 2012.

Quinn, P., Beven, K., Chevallier, P., and Planchon, O.: The prediction of hillslope flow paths for distributed hydrological modelling using digital terrain models, Hydrological Processes, 5, 59–79, doi:10.1002/hyp.3360050106, 1991.

Retzlaff, R. and Bentley, C. R.: Timing of stagnation of Ice Stream C, West Antarctica, from short-pulse radar studies of buried surface crevasses, Journal of Glaciology, 39, 1993.

Ridley, J. K., Cudlip, W., and Laxon, S. W.: Identification of subglacial lakes using ERS-1 radar altimeter, Journal of Glaciology, 39, 625–634, 1993.

Rignot, E., Mouginot, J., and Scheuchl, B.: Ice flow of the Antarctic ice sheet, Science, 333, 1427–1430, doi:10.1126/science.1208336, 2011a.

Rignot, E., Velicogna, I., van den Broeke, M., Monaghan, A., and Lenaerts, J.: Acceleration of the contribution of the Greenland and Antarctic ice sheets to sea level rise, GEOPHYSICAL RESEARCH LETTERS, 38, L05 503, doi:10.1029/2011GL046583, 2011b.

Robin, G. d. Q.: Ice movement and temperature distribution in glaciers and ice sheets, Journal of Glaciology, 2, 523–532, doi:10.3189/002214355793702028, 1955.

Robin, G. d. Q., Swithinbank, C., and Smith, B.: Radio echo exploration of the Antarctic ice sheet, International Association of Scientific Hydrology Publication, 86, 97–115, 1970.

Robin, G. d. Q., Drewry, D., and Meldrum, D.: International studies of ice sheet and bedrock, Philosophical Transactions of the Royal Society of London. B, Biological Sciences, 279, 185–196, doi:10.1098/rstb.1977.0081, 1977.

Robinson, R.: Experiment in visual orientation during flights inthe Antarctic, International Bulletin of the Soviet Antarctic Expeditions, 18, 28–29, 1960.

Roemer, S., Legrésy, B., Horwath, M., and Dietrich, R.: Refined analysis of radar altimetry data applied to the region of the subglacial Lake Vostok/Antarctica, Remote sensing of environment, 106, 269–284, doi:10.1016/j.rse.2006.02.026, 2007.

Roethlisberger, H.: Water pressure in intra- and subglacial channels, Journal of Glaciology, 11, 177–203, 1972.

Rooney, S., Blankenship, D., Alley, R., and Bentley, C.: Till beneath ice stream B: 2. Structure and continuity, Journal of Geophysical Research: Solid Earth (1978–2012), 92, 8913–8920, doi:10.1029/JB092iB09p08913, 1987.

Rose, K.: Characteristics of ice flow in Marie Byrd Land, Antarctica, Journal of Glaciology, 24, 63–75, 1979.

Sandhäger, H.: Quantifizierung eisdynamischer und massenhaushaltsrelevanter Basisgrößen eines antarktischen Inland-Schelfeis-Systems unter Einsatz eines numerischen Fließmodells, Ph.D. thesis, Westfälische Wilhelms-Universität Münster, 2000.

Sato, T. and Greve, R.: Sensitivity experiments for the Antarctic Ice Sheet with varied sub-ice-shelf melting rates, Annals of Glaciology, 53, 221–228, doi:10.3189/2012AoG60A042, 2012.

Scheuchl, B., Mouginot, J., and Rignot, E.: Ice velocity changes in the Ross and Ronne sectors observed using satellite radar data from 1997 and 2009, The Cryosphere, 6, 1019–1030, doi:10.5194/tc-6-1019-2012, 2012.

Schoof, C.: Ice-sheet acceleration driven by melt supply variability, Nature, 468, 803–806, doi:10.1038/nature09618, 2010.

Schoof, C., Hewitt, I. J., and Werder, M. A.: Flotation and free surface flow in a model for subglacial drainage. Part 1. Distributed drainage, Journal of Fluid Mechanics, 702, 126–156, doi:10.1017/jfm.2012.165, 2012.

Sergienko, O. V. and Hulbe, C. L.: 'Sticky spots' and subglacial lakes under ice streams of the Siple Coast, Antarctica, Annals of Glaciology, 52, 18–22, doi:10.3189/172756411797252176, 2011.

Shabtaie, S. and Bentley, C. R.: West Antarctic ice streams draining into the Ross Ice Shelf: Configuration and mass balance, Journal of Geophysical Research, 92, 1311–1336, doi:10.1029/JB092iB02p01311, 1987.

Shapiro, N. M. S. and Ritzwoller, M. H.: Inferring surface heat flux distributions guided by a global seismic model: particular application to Antarctica, Earth and Planetary Science Letters, 223, 213–224, doi:10.1016/j.epsl.2004.04.011, 2004.

Shepherd, A., Ivins, E. R., Geruo, A., Barletta, V. R., Bentley, M. J., Bettadpur, S., Briggs, K. H., Bromwich, D. H., Forsberg, R., Galin, N., et al.: A reconciled estimate of ice-sheet mass balance, Science, 338, 1183–1189, doi:10.1126/science.1228102, 2012.

Shreve, R. L.: Movement of water in glaciers, Journal of Glaciology, 11, 205–214, 1972.

Siegert, M., Behar, A., Bentley, M., Blake, D., Bowden, S., Christoffersen, P., Cockell, C., Corr, H., Cullen, D., Edwards, H., et al.: Exploration of Ellsworth Subglacial Lake: a concept paper on the development, organisation and execution of an experiment to explore, measure and sample the environment of a West Antarctic subglacial lake, Reviews in Environmental Science and Bio/Technology, 6, 161–179, doi:10.1007/s11157-006-9109-9, 2007.

Siegert, M. J.: Antarctic subglacial lakes, Earth-Science Reviews, 50, 29–50, doi:10.1016/S0012-8252(99)00068-9, 2000.

Siegert, M. J.: Which are the most suitable Antarctic subglacial lakes for exploration?, Polar Geography, 26, 134–146, doi:10.1080/789610135, 2002.

Siegert, M. J.: Comment on "A numerical model for an alternative origin of Lake Vostok and its exobiological implications for Mars" by NS Duxbury et al., Journal of Geophysical Research, 109, E02 007, doi:10.1029/2003JE002176, 2004.

Siegert, M. J., Dowdeswell, J., Gorman, M., and McIntyre, N.: An inventory of Antarctic subglacial lakes, Antarctic Science, 8, 281–286, 1996.

Siegert, M. J., Ellis-Evans, J. C., Tranter, M., Mayer, C., Petit, J.-R., Salamatin, A., and Priscu, J. C.: Physical, chemical and biological processes in Lake Vostok and other Antarctic subglacial lakes, Nature, 414, 603–609, doi:10.1038/414603a, 2001.

Siegert, M. J., Taylor, J., Payne, A. J., and Hubbard, B.: Macro-scale bed roughness of the Siple Coast ice streams in West Antarctica, Earth Surface Processes and Landforms, 29, 1591–1596, doi:10.1002/esp.1100, 2004.

Siegert, M. J., Carter, S., Tabacco, I., Popov, S., and Blankenship, D. D.: A revised inventory of Antarctic subglacial lakes, Antarctic Science, 17, 453–460, doi:10.1017/S0954102005002889, 2005.

Siegert, M. J., Le Brocq, A., and Payne, A. J.: Hydrological connections between Antarctic subglacial lakes, the flow of water beneath the East Antarctic Ice Sheet and implications for sedimentary processes, Glacial Sedimentary Processes and Products, 39, 3–10, 2009.

Smith, B. E., Fricker, H. A., Joughin, I. R., and Tulaczyk, S.: An inventory of active subglacial lakes in Antarctica detected by ICESat (2003–2008), Journal of Glaciology, 55, 573–595, doi:10.3189/002214309789470879, 2009.

Spring, U. and Hutter, K.: Conduit flow of a fluid through its solid phase and its application to intraglacial channel flow, International Journal of Engineering Science, 20, 327–363, doi:10.1016/0020-7225(82)90029-5, 1982.

Steinhage, D., Bellot, F.-F., Gudlaugsson, E., Helm, V., and Humbert, A.: Basal roughness of the ice sheet in Dronning Maud Land, Antarctica, Journal of Glaciology, in prep.

Studinger, M., Bell, R. E., Karner, G. D., Tikku, A. A., Holt, J. W., Morse, D. L., Richter, T. G., Kempf, S. D., Peters, M. E., Blankenship, D. D., et al.: Ice cover, landscape setting, and geological framework of Lake Vostok, East Antarctica, Earth and Planetary Science Letters, 205, 195–210, doi:10.1016/S0012-821X(02)01041-5, 2003.

Studinger, M., Bell, R. E., and Tikku, A. A.: Estimating the depth and shape of subglacial Lake Vostok's water cavity from aerogravity data, Geophysical Research Letters, 31, L12 401, doi:10.1029/2004GL019801, 2004.

Sundal, A. V., Shepherd, A., Nienow, P., Hanna, E., Palmer, S., and Huybrechts, P.: Melt-induced speed-up of Greenland ice sheet offset by efficient subglacial drainage, Nature, 469, 521–524, doi:10.1038/nature09740, 2011.

Tabacco, I. E., Cianfarra, P., Forieri, A., Salvini, F., and Zirizotti, A.: Physiography and tectonic setting of the subglacial lake district between Vostok and Belgica subglacial highlands (Antarctica), Geophysical Journal International, 165, 1029–1040, doi:10.1111/j.1365-246X.2006.02954.x, 2006.

Tarboton, D.: A new method for the determination of flow directions and upslope areas in grid digital elevation models., Water Resources Research, 33 (2), 309–319, doi:10.1029/96WR03137, 1997.

Thoma, M., Grosfeld, K., and Mayer, C.: Modelling accreted ice in subglacial Lake Vostok, Antarctica, Geophysical Research Letters, 35, doi:10.1029/2008GL033607, 2008.

Thoma, M., Grosfeld, K., Filina, I., and Mayer, C.: Modelling flow and accreted ice in subglacial Lake Concordia, Antarctica, Earth and Planetary Science Letters, 286, 278–284, doi:10.1016/j.epsl.2009.06.037, 2009.

Thoma, M., Grosfeld, K., Mayer, C., and Pattyn, F.: Interaction between ice sheet dynamics and subglacial lake circulation: a coupled modelling approach, The Cryosphere, 4, 1–12, doi:10.5194/tc-4-1-2010, 2010.

Thoma, M., Grosfeld, K., Mayer, C., and Pattyn, F.: Ice-flow sensitivity to boundary processes: a coupled model study in the Vostok Subglacial Lake area, Antarctica, Annals of Glaciology, 53, 173–180, doi:10.3189/2012AoG60A009, 2012.

Thoma, M., Grosfeld, K., Barbi, D., Determann, J., Goeller, S., Mayer, C., and Pattyn, F.: RIMBAY – a multi-approximation 3D ice-dynamics model for comprehensive applications: model description and examples, Geoscientific Model Development, 7, 1–21, doi:10.5194/gmd-7-1-2014, 2014.

Twidale, C. R.: River patterns and their meaning, Earth-Science Reviews, 67, 159–218, doi:10.1016/j.earscirev.2004.03.001, 2004.

Van der Veen, C. and Whillans, I.: Force budget: I. Theory and numerical methods, Journal of Glaciology, 35, 53–60, doi:10.3189/002214389793701581, 1989.

Vaughan, D. G., Rivera, A., Woodward, J., Corr, H. F., Wendt, J., and Zamora, R.: Topographic and hydrological controls on subglacial Lake Ellsworth, West Antarctica, Geophysical Research Letters, 34, L18 501, doi:10.1029/2007GL030769, 2007.

Walder, J. S. and Fowler, A.: Channelized subglacial drainage over a deformable bed, Journal of Glaciology, 40, 3–15, 1994.

Weertman, J.: General theory of water flow at the base of a glacier or ice sheet, Reviews of Geophysics and Space Physics, 10, 287–333, doi:10.1029/RG010i001p00287, 1972.

Welch, B. C. and Jacobel, R. W.: Analysis of deep-penetrating radar surveys of West Antarctica, US-ITASE 2001, Geophysical Research Letters, 30, doi:10.1029/2003GL017210, 2003.

Wingham, D., Francis, C., Baker, S., Bouzinac, C., Brockley, D., Cullen, R., de Chateau-Thierry, P., Laxon, S., Mallow, U., Mavrocordatos, C., et al.: CryoSat: A mission to determine the fluctuations in Earth's land and marine ice fields, Advances in Space Research, 37, 841–871, doi:10.1016/j.asr.2005.07.027, 2006a.

Wingham, D. J., Siegert, M. J., Shepherd, A., and Muir, A. S.: Rapid discharge connects Antarctic subglacial lakes, Nature, 440, 1033–1036, doi:10.1038/nature04660, 2006b.

Winkelmann, R., Martin, M., Haseloff, M., Albrecht, T., Bueler, E., Khroulev, C., and Levermann, A.: The Potsdam Parallel Ice Sheet Model (PISM-PIK)–Part

1: Model description, The Cryosphere, 5, 715–726, doi:10.5194/tc-5-715-2011, 2011.

Winsborrow, M., Clark, C. D., and Stokes, C. R.: What controls the location of ice streams?, Earth-Science Reviews, 103, 45–59, doi:10.1016/j.earscirev.2010.07.003, 2010.

Woodward, J., Smith, A. M., Ross, N., Thoma, M., Corr, H., King, E. C., King, M., Grosfeld, K., Tranter, M., and Siegert, M.: Location for direct access to subglacial Lake Ellsworth: An assessment of geophysical data and modeling, Geophysical Research Letters, 37, doi:10.1029/2010GL042884, 2010.

Wright, A. and Siegert, M. J.: The identification and physiographical setting of Antarctic subglacial lakes: an update based on recent discoveries, in: Subglacial Antarctic Aquatic Environments, Geophysical Monograph Series, vol. 192, pp. 9–26, AGU, Washington D.C., doi:10.1029/2010GM000933, 2011.

Wright, A. and Siegert, M. J.: A fourth inventory of Antarctic subglacial lakes, Antarctic Science, 24, 659–664, doi:10.1017/S095410201200048X, 2012.

Wright, A., Siegert, M. J., Le Brocq, A. M., and Gore, D. B.: High sensitivity of subglacial hydrological pathways in Antarctica to small ice-sheet changes, Geophysical Research Letters, 37, L17 504, doi:10.1029/2008GL034937, 2008.

Wright, A., Young, D., Roberts, J., Schroeder, D., Bamber, J., Dowdeswell, J., Young, N., Le Brocq, A., Warner, R., Payne, A., et al.: Evidence of a hydrological connection between the ice divide and ice sheet margin in the Aurora Subglacial Basin, East Antarctica, Journal of Geophysical Research: Earth Surface (2003–2012), 117, doi:10.1029/2011JF002066, 2012.

Wynn-Williams, D. and Edwards, H.: Antarctic ecosystems as models for extraterrestrial surface habitats, Planetary and Space Science, 48, 1065–1075, doi:10.1016/S0032-0633(00)00080-5, 2000.

Zotikov, I.: The thermophysics of glaciers, Reidel, Dordrecht, 1987.

Zwally, H., Schutz, B., Abdalati, W., Abshire, J., Bentley, C., Brenner, A., Bufton, J., Dezio, J., Hancock, D., Harding, D., et al.: ICESat's laser measurements of polar ice, atmosphere, ocean, and land, Journal of Geodynamics, 34, 405–445, doi:10.1016/S0264-3707(02)00042-X, 2002.

APPENDIX

A

SUBGLACIAL LAKES IN ANTARCTICA

A.1 PREDICTED SUBGLACIAL LAKES MATCHING KNOWN LAKES

Table 5 shows a list of 206 subglacial lakes in Antarctica which were both theoretically predicted applying the modeling approach in Sec. 4.2 and observed by in situ seismic investigations, radio-echo sounding (RES) flights or ice surface elevation changes. The tally, position and name of the lakes in Tab. 5 follow the current inventory of Antarctic subglacial lakes by Wright and Siegert (2012), comprising 379 subglacial lakes in total.

Table 5: Known Antarctic subglacial lakes which were successfully predicted.

Inventory tally	Longitude	Latitude	Name
1	88.50°E	78.10°S	Sovetskaya Lake
2	104.50°E	78.15°S	Lake Vostok
3	124.80°E	76.57°S	SPRI-3
6	125.02°E	74.07°S	Concordia Lake
7	150.00°W	88.30°S	SPRI-7
8	123.94°E	72.31°S	SPRI-8
10	127.41°E	75.94°S	SPRI-10
15	119.54°E	73.45°S	SPRI-17
16	135.34°E	76.24°S	Adventure Trench Lake
19	124.95°E	75.97°S	SPRI-22
21	126.48°E	75.69°S	SPRI-24
26	140.95°E	69.71°S	SPRI-29
30	118.50°E	74.03°S	SPRI-33
31	119.37°E	74.46°S	Aurora Lake
32	126.30°E	77.12°S	SPRI-35
36	148.86°E	75.73°S	SPRI-39
39	125.18°E	76.19°S	SPRI-42/43
41	154.13°E	79.43°S	SPRI-45
42	100.40°E	77.40°S	SPRI-46
44	64.52°E	88.73°S	SPRI-48
50	92.50°E	77.10°S	SPRI-54/59

Inventory tally	Longitude	Latitude	Name
52	155.68°E	71.13°S	SPRI-56
54	93.50°E	76.80°S	SPRI-60
56	129.41°E	72.74°S	SPRI-62
58	118.11°E	76.07°S	SPRI-65
59	118.60°E	78.00°S	SPRI-66
63	161.56°W	89.97°S	South Pole Lake (SPRI-70)
70	90.57°W	78.99°S	Subglacial Lake Ellsworth
71	121.63°E	75.46°S	ITL-1
73	122.31°E	75.42°S	ITL-3
78	125.92°E	75.02°S	ITL-9
83	119.72°E	73.70°S	ITL-17
85	26.94°E	74.30°S	M-310
87	27.29°E	75.17°S	M-511
89	37.43°E	77.50°S	M-2011
91	27.03°E	75.46°S	M-2713
94	77.89°E	82.34°S	M-3010
94	77.89°E	82.34°S	M-3010
101	144.66°E	77.10°S	WLK-6
102	145.09°E	76.71°S	WLK-14
103	144.29°E	76.43°S	WLK-12
104	144.75°E	76.12°S	WLK-24
106	139.23°E	80.41°S	DCS/DCSx/X02b-X02e
107	120.08°E	81.84°S	DCS/DCSx/X01c
109	117.99°E	75.85°S	LVS-12
110	88.88°E	79.30°S	LVS-9
112	91.08°E	77.38°S	90 Degree East Lake
116	120.13°W	81.45°S	Kamb10
118	135.00°E	75.94°S	U1
119	135.77°E	76.34°S	U2
121	107.13°E	78.58°S	unnamed
132	107.80°E	78.05°S	unnamed
137	105.37°E	78.60°S	unnamed
139	103.62°E	77.88°S	unnamed

continued from previous page

Inventory tally	Longitude	Latitude	Name
146	103.36°E	77.50°S	unnamed
147	103.86°E	75.91°S	unnamed
148	105.00°E	78.58°S	unnamed
150	97.29°E	73.62°S	Komsomolskoe Subglacial lake
151	95.54°E	69.75°S	Pionerskoe Subglacial Lake
152	150.11°E	77.42°S	WLK-4
153	148.93°E	76.88°S	WLK-5
154	153.72°E	77.16°S	WLK-7
155	150.94°E	77.00°S	WLK-8
157	150.21°E	76.88°S	WLK-10
158	147.75°E	77.32°S	WLK-11
159	139.04°E	75.76°S	WLK-13
160	126.59°E	75.23°S	Horseshoe Lake (WLK-15)
163	137.35°E	76.02°S	WLK-19
166	137.33°E	76.12°S	WLK-23
168	135.75°E	75.65°S	WLK-27
170	143.81°E	76.15°S	WLK-29
171	146.04°E	76.49°S	WLK-30
174	147.24°E	77.29°S	WLK-33
175	148.30°E	76.80°S	WLK-34
176	150.14°E	76.67°S	WLK-35
177	149.68°E	76.99°S	WLK-36
178	150.47°E	76.49°S	WLK-37
179	150.61°E	77.08°S	WLK-38
180	150.92°E	76.90°S	WLK-39
181	150.93°E	77.28°S	WLK-40
184	119.23°E	75.61°S	LVS-1
186	118.71°E	75.71°S	LVS-3
187	103.32°E	77.46°S	LVS-4
189	108.16°E	78.02°S	LVS-6
191	143.83°W	89.76°S	PPT-1
192	120.39°W	88.91°S	PPT-2
193	86.10°W	89.85°S	PPT-3

continued from previous page

Inventory tally	Longitude	Latitude	Name
197	141.81°W	84.97°S	PPT-8
199	150.00°W	84.75°S	PPT-11
201	144.12°W	84.87°S	PPT-15
202	149.68°W	84.66°S	PPT-16 (Lake Mercer)
203	13.77°W	89.48°S	PPT-17
209	139.78°W	88.49°S	PPT-23
211	126.29°W	89.33°S	PPT-26
216	78.70°W	89.34°S	PPT-32
218	7.61°E	88.26°S	PPT-35
219	83.34°W	89.32°S	PPT-36
222	78.86°W	89.17°S	PPT-39
223	117.81°W	88.41°S	PPT-40
226	116.90°W	88.36°S	PPT-43
228	14.28°E	82.40°S	Recovery A
229	18.13°E	82.85°S	Recovery B
230	21.37°E	84.31°S	Recovery C
232	154.19°W	84.60°S	Mercer1
233	157.42°W	83.73°S	Whillans1 (Lake Engelhardt)
234	160.27°W	84.03°S	Whillans2a
235	158.20°W	84.34°S	Whillans2b
236	153.69°W	84.24°S	Whillans3 (Lake Whillans)
237	148.72°W	84.37°S	Whillans4 (Lake Conway)
244	120.15°E	74.07°S	ITL-23
249	125.06°E	76.07°S	ITL-28
250	61.34°W	84.14°S	Academy1
251	57.45°W	84.54°S	Academy2
254	53.70°W	84.84°S	Academy5
255	55.22°W	85.32°S	Academy6
256	53.72°W	85.56°S	Academy7
257	52.93°W	85.65°S	Academy8
259	50.99°W	85.77°S	Academy10
260	48.41°W	85.80°S	Academy11
261	45.38°W	85.71°S	Academy12

Inventory tally	Longitude	Latitude	Name
263	39.57°W	85.78°S	Academy14
266	131.50°W	80.35°S	Bindschadler1
267	130.20°W	79.94°S	Bindschadler2
269	125.57°W	80.73°S	Bindschadler4
273	149.61°E	81.80°S	ByrdS3
274	143.71°E	80.75°S	ByrdS4
275	143.38°E	80.58°S	ByrdS5
276	143.66°E	80.32°S	ByrdS6
276	143.66°E	80.32°S	ByrdS6
277	143.74°E	80.03°S	ByrdS7
278	142.41°E	80.01°S	ByrdS8
280	139.03°E	81.83°S	ByrdS10
283	142.83°E	78.93°S	ByrdS13
284	139.78°E	78.83°S	ByrdS14
285	138.96°E	78.81°S	ByrdS15
286	155.34°E	71.87°S	CookE1
287	155.79°E	72.80°S	CookE2
292	152.92°E	75.24°S	David3
293	152.25°E	75.73°S	David4
294	152.46°E	74.88°S	David5
295	145.24°E	75.39°S	David6
296	140.64°E	85.84°S	EAP1
297	135.48°E	85.68°S	EAP2
299	128.37°E	85.91°S	EAP4
300	124.42°E	85.66°S	EAP5
304	135.56°E	75.81°S	EAP9
305	73.66°W	84.52°S	Foundation1
308	74.49°W	82.13°S	InstituteE1
309	79.01°W	82.62°S	InstituteE2
312	140.40°W	81.95°S	Kamb
312	140.40°W	81.95°S	Kamb
313	131.20°W	82.01°S	Kamb1
313	131.20°W	82.01°S	Kamb1

Inventory tally	Longitude	Latitude	Name
314	129.84°W	82.19°S	Kamb2
315	128.60°W	81.94°S	Kamb3
316	127.44°W	81.97°S	Kamb4
317	127.48°W	82.27°S	Kamb5
318	124.34°W	82.06°S	Kamb6
320	123.14°W	82.38°S	Kamb8
321	121.63°W	82.32°S	Kamb9
324	68.28°E	74.00°S	Lambert1
325	157.12°E	84.77°S	Lennox-King1
326	145.36°W	79.95°S	MacAyeal1/Mac1
326	145.36°W	79.95°S	MacAyeal1/Mac1
327	144.08°W	79.83°S	MacAyeal2/Mac2
329	149.11°E	78.09°S	Mulock1
334	29.08°W	81.15°S	Recovery1
337	20.05°W	81.32°S	Recovery4
338	9.61°W	81.28°S	Recovery5
338	9.61°W	81.28°S	Recovery5
339	7.24°W	81.43°S	Recovery6
340	5.98°W	81.64°S	Recovery7
341	4.12°W	81.80°S	Recovery8
342	2.34°E	82.91°S	Recovery9
343	5.94°E	83.50°S	Recovery10
344	8.42°E	81.72°S	Recovery11
345	84.17°W	78.18°S	Rutford1
347	21.56°W	79.84°S	Slessor2
349	17.09°W	79.34°S	Slessor4
350	17.04°W	79.20°S	Slessor5
351	14.30°W	78.77°S	Slessor6
352	11.05°W	79.25°S	Slessor7
353	107.50°E	70.10°S	Totten1
354	110.51°E	70.83°S	Totten2
357	136.91°W	83.85°S	Whillans6
361	121.57°E	68.70°S	Wlikes2

continued from previous page

Inventory tally	Longitude	Latitude	Name
362	142.81°W	80.02°S	Mac3
363	139.00°W	79.74°S	Mac4
364	139.11°W	79.64°S	Mac5
365	11.65°E	82.00°S	unnamed
366	130.40°E	70.43°S	R03Wa 1
367	135.00°E	71.62°S	R04Ea 9
369	129.06°E	71.84°S	R05Ea 5
373	122.58°E	74.29°S	R08Wa 0.1
374	122.50°E	74.30°S	R08Wa 0.2
375	106.05°E	75.98°S	R13Ea 8
376	100.82°E	74.08°S	R15Ea 4
377	112.54°E	67.80°S	Site A

A.2 PREDICTED AND RADAR-IDENTIFIED SO FAR UNKNOWN SUBGLACIAL LAKES

Table 6 shows a list of 31 theoretically predicted and so far uncharted subglacial lakes in Antarctica where lake-like basal radar reflections were identified in the corresponding RES profiles. The result is based on the visual interpretation of 270 RES flight lines from flight campaigns of the Alfred Wegener Institute (AWI) between 1994 and 2013 where the flight lines cross the contours of the predicted lakes. The tally for predicted lakes in Tab. 6 follows the inventory of all 10 183 predicted lakes, whereby some predicted lake locations are crossed by more then one flight line (e.g., lake 152). The given position is corresponding to the central shot number in the specified shot number range. As an additional information, the first two digits in the flight number describe the year of the respective flight campaign.

Table 6: Predicted lake locations where lake-like basal radar reflections were identified in AWI RES profiles.

Predicted lake tally	Longitude	Latitude	Flight line	Shot numbers
152	8.11°E	73.46°S	022119	6040−6144
152	8.10°E	73.47°S	042016	11177−11334
152	8.23°E	73.53°S	042021	2830−2860
154	12.43°E	73.27°S	042010	15−223

Predicted lake tally	Longitude	Latitude	Flight line	Shot numbers
155	7.25°E	73.53°S	042021	1975 – 1993
201	10.91°E	73.81°S	082029	39230 – 39419
210	16.21°E	73.41°S	042032	7282 – 7304
220	2.90°W	74.18°S	032003	11190 – 11222
234	8.01°E	74.25°S	042016	12929 – 13284
243	10.31°E	74.09°S	082029	9939 – 10004
246	7.27°E	74.25°S	022027	14561 – 14568
284	9.98°E	74.37°S	042015	6288 – 6314
332	6.09°W	74.85°S	032021	12125 – 12364
411	6.82°W	75.16°S	982406	253 – 262
457	9.37°W	75.37°S	052012	25012 – 25273
474	6.97°W	75.58°S	052010	4758 – 4887
474	6.57°W	75.56°S	052109	2732 – 2780
474	6.61°W	75.56°S	982407	2263 – 2327
489	9.00°W	75.56°S	052012	24403 – 24622
499	5.01°W	75.70°S	052107	2743 – 2837
499	4.90°W	75.70°S	982102	5257 – 5337
662	10.45°E	76.49°S	082029	15838 – 31083
799	12.07°W	77.14°S	952306	2315 – 2814
816	13.90°W	77.11°S	952309	4858 – 4870
831	41.93°E	73.26°S	062017	19077 – 19102
958	18.89°W	77.48°S	952409	8645 – 8653
1100	15.00°W	78.32°S	952210	2839 – 3039
1138	32.21°E	76.81°S	032141	2796 – 2819
1480	34.14°E	78.11°S	032139	6073 – 6075
3999	60.29°E	88.16°S	112120	6641 – 7283
5054	93.34°E	73.13°S	082121	12119 – 12134
7379	118.12°E	76.83°S	082120	4247 – 4256
7833	121.09°E	75.93°S	082120	5792 – 5894
8001	122.14°E	75.58°S	082120	6423 – 6435
8741	130.56°E	74.56°S	082117	18930 – 18942
9704	154.80°E	73.24°S	082117	9297 – 9468

B

PUBLICATIONS

Goeller, S., Thoma, M., Grosfeld, K. and Miller, H., A balanced water layer concept for subglacial hydrology in large-scale ice sheet models, *The Cryosphere, 7*(4), 1095–1106, doi:10.5194/tc-7-1095-2013, 2013.

Thoma, M., Grosfeld, K., Barbi, D., Determann, J., Goeller, S., Mayer, C. and Pattyn, F., Rɪᴍʙᴀʏ – a multi-approximation 3D ice-dynamics model for comprehensive applications: model description and examples, *Geoscientific Model Development, 7, 1–21*, doi:10.5194/gmd-7-1-2014, 2014.

Goeller, S., Thoma, M., Grosfeld, K., Helm, V. and Miller, H. Evolution of subglacial hydrology and ice dynamics at the Siple Coast, Antarctica, *Geophysical Research Letters*, in prep.